ABSTRACT

Title of dissertation: NOISE-INFLUENCED DYNAMICS OF NONLINEAR OSCILLATORS

J. Edmon Perkins,
Doctor of Philosophy, 2015

Dissertation directed by: Professor Balakumar Balachandran
Department of Mechanical Engineering

Noise is usually considered detrimental to the performance of a system and the effects of noise are usually mitigated through design and/or control. In this dissertation, noise-influenced phenomena and qualitative changes in responses of nonlinear systems with noise are explored.

Here, the author considers a range of nonlinear dynamical systems, including an array of nonlinear, coupled oscillators, a vertically excited pendulum, the Duffing oscillator, and a Rayleigh-Duffing mixed type oscillator. These systems are studied analytically and numerically via stochastic direct numerical integration, and analytically via the Fokker-Planck equation. The array of nonlinear, coupled oscillators is also experimentally studied. The topics covered in this dissertation are as follows: i) the destruction and formation of energy localizations in an array of oscillators, ii) a technique to stabilize an inverted pendulum by using noise, iii) a noise-utilizing control scheme, iv) the effects of noise on the response of a nonlinear system that exhibits chaotic behavior, v) and the effects of phase lag on the information rate of a Duffing oscillator. The understanding gained through this dissertation efforts can be of benefit to a variety of nonlinear systems, including structural systems at the macro-scale, micro-scale, and nano-scale.

NOISE-INFLUENCED DYNAMICS OF NONLINEAR OSCILLATORS

by

J. Edmon Perkins

Dissertation submitted to the Faculty of the Graduate School of the
University of Maryland, College Park in partial fulfillment
of the requirements for the degree of
Doctor of Philosophy
2015

Advisory Committee:
Professor Balakumar Balachandran, Chair and Advisor, Mechanical Engineering
Professor Amr Baz, Department of Mechanical Engineering
Associate Professor Nikhil Chopra, Department of Mechanical Engineering
Associate Professor Miao Yu, Department of Mechanical Engineering
Professor Konstantina Trivisa, Department of Mathematics and AMSC (Dean's Representative)

Acknowledgments

The guidance and patience of my advisor, Dr. Bala Balachandran, is most appreciated. Many thanks are also given to my labmates for their thoughtful, useful, and candid advice. My thanks, as well, to my dissertation defense committee for their time and comments.

Support received for this research through NSF Grant Nos. 0826173 and 1414764, JSPS Grant No. SP14048, the Ford Foundation, and the Sloan Foundation is gratefully acknowledged.

Table of Contents

List of Tables

List of Figures

List of Abbreviations

DB	Discrete Breather
FPE	Fokker-Planck equation
ILM	Intrinsic localized mode
ODE	Ordinary differential equation
PDE	Partial differential equation
SDE	Stochastic differential equation
SNR	Signal-to-Noise Ratio

Chapter 1

INTRODUCTION

1.1 Problem of Interest

In this dissertation, the author has studied the effects of mechanical noise on several nonlinear oscillators. Unless otherwise stated, in this dissertation, "noise" refers to white Gaussian noise, which is a random process. Noise can enter into the dynamics of a system through multiple ways: thermal noise (especially, noticeable in micro-systems and nano-systems), noise in feedback controller (which can come from sensor noise or actuator noise), biological noise (e.g., neuronal interactions), and many others not to be considered here. Since noise is typically considered to be undesirable, it is either ignored or controlled in a manner in which its effect is suppressed [Poznyak and Taksar (1996)]. Since noise is a prevalent source of energy, it is not surprising that many systems are affected by it. Many physical systems have dynamics that are influenced by noise. For nonlinear systems, this energy can have counter-intuitive effects. The well-known stochastic resonance is one such example of this.

Since so many systems have been shown to exhibit stochastic resonance (literally thousands of papers have been written about stochastic resonance), other types of noise-influenced phenomena are also possible. Although, there has been much less work done in studying the effects of noise, if it is not a form of stochastic resonance.

One of the primary goals of this research is to explore what kinds of phenomena may be produced in nonlinear oscillators when they are subjected to noise. This is a difficult problem because nonlinear oscillators have very rich dynamics, even without the presence of noise. Hysteresis, high-frequency stabilization, energy localizations,

and chaos may occur in nonlinear oscillators.

The author has studied several nonlinear systems, including the nonlinear pendulum, the Rayleigh-Duffing mixed type oscillator, the Duffing oscillator, as well as an array of Duffing oscillators. Direct numerical simulations of these stochastic systems are performed, by using the Euler-Maruyama or the Euler-Heun method. The Fokker-Planck equation is also analyzed to study the system dynamics. An experimental arrangement of the array of Duffing oscillators is also studied.

The problems of interest for this work are instances where noise can have a beneficial effect on a nonlinear system, similar to, but broader than that associated with the phenomenon of stochastic resonance. The motivation is to develop systems that are not only robust to noise, but can also actually use noise that is already present in the systems' environment. By using noise (energy) that is already prevalent in the environment, one can understand how to exploit this energy to achieve a better system performance.

1.2 Prior Work

In each chapter of this dissertation, literature pertaining to the particular systems considered in that chapter are discussed. To put this dissertation in a broader context, stochastic resonance and related observations are discussed in this section.

Stochastic resonance, in its classical form, needs three ingredients to occur: 1) a bistable potential, 2) a noise source, and 3) a weak, periodic signal [Gammaitoni, Hänggi, Jung, and Marchesoni (1998)]. Although this phenomenon was first formulated to explain the occurrence of ice ages [Benzi, Sutera, and Vulpiani (1981); Benzi, Parisi, Sutera, and Vulpiani (1982)], it has been shown to be a nearly ubiquitous. In its first description, the bistable potential was the earth's state ("ice age" or "non-ice age"). If one considers the state of being in an ice age and the

state of being in a non-ice age as two equilibrium positions of the climate system, then, the stability of the climate ("ice age" versus "non-ice age") is explained by the fact that when the earth is in an ice age, it reflects more sunlight, keeping the earth cooler. Conversely, when the earth is not in an ice age, it absorbs more sunlight, keeping the earth warmer. The noise source in this example was random fluctuations in weather patterns. The weak signal was the variation of solar energy influx, caused by the orbital eccentricity of the earth. This signal has a period of 10^5 years (which is also the average length of the periodicity of ice ages), and it is quite weak, amounting to only a 0.1% change in solar energy influx [Gammaitoni, Hänggi, Jung, and Marchesoni (1998)]. In essence, the very weak signal is "boosted" by random fluctuations in weather patterns, to cause a shift between an ice age state and a non-ice age state.

Since the initial formulation of stochastic resonance, many physical and biological systems have been shown to be either strongly influenced by noise or "tuned" to noise. During the subsequent thirty years, the phenomenon of stochastic resonance has been studied in many different fields. It has been shown to be an important phenomenon in climatic systems [Benzi *et al.* (1981, 1982)], biological systems [Hänggi (2002); Levin and Miller (1996); Douglass, Wilkens, Pantazelou, and Moss (1993); Dussutour, Beekman, Nicolis, and Meyer (2009)], physical systems [McNamara, Wiesenfeld, and Roy (1988); Pérez-Madrid and Rubi (1995)], mechanical systems [Almog, Zaitsev, Shtempluck, and Buks (2007)], and chemical systems [Guderian, Dechert, Zeyer, and Schneider (1996); Leonard and Reichl (1994)]. For nanomechanical oscillators, experimental validation to show that thermal energy can cause a stochastic resonance effect has been carried out [Badzey and Mohanty (2005)]. Several literature reviews have been written on this phenomenon [Gammaitoni *et al.* (1998); Wiesenfeld and Moss (1995)].

The classical form of stochastic resonance is explained in the context of a system

with a bistable potential, for instance, the Duffing equation with negative linear stiffness and positive cubic stiffness. However, the definition for stochastic resonance can also be expanded to encompass more exotic varieties of this phenomenon, for example, phenomenon exhibited by monostable oscillators such as in the cases of neuron firing [Levin and Miller (1996); Douglass, Wilkens, Pantazelou, and Moss (1993); Collins, Chow, Capela, and Imhoff (1996)]. The neuron model considered is a model with a monostable potential and a threshold; if the threshold is reached, the neuron will fire before entering a relaxation period.

The prevalence of stochastic resonance in biological systems seems to indicate that evolution prefers the utilization of noise, which seems reasonable given that it is a free source of energy. Although many researchers have studied a wide variety of systems, a few will be discussed briefly here. Some of the first work in biological stochastic resonance was on the cricket sensory system [Levin and Miller (1996)]. Since this work, more complex biological systems have been studied as well. Randomly vibrating insoles have been shown to ameliorate impaired balance control [Priplata, Niemi, Harry, Lipsitz, and Collins (2003)]. Hairs in the cochlea have also been shown to have enhanced sensitivity, with the addition of noise [Morse, Allingham, and Stocks (2003); Jaramillo and Wiesenfeld (1998)]. However, arguably the most profound versions of biological stochastic resonance are several studies on the blood pressure regulatory system and vision [Hidaka *et al.* (2000)]. Researchers believe that a weak periodic signal introduced to a venous blood pressure receptor is optimized by adding noise to the arterial blood pressure receptor. With this formulation, these researchers believe that the stochastic resonance effect is happening in the brain stem. Similarly, by stimulating one eye with a subthreshold periodic optical signal and the other eye with noise, researchers observed that stochastic resonance also happens in the visual processing area of the human brain [Mori and Kai (2002)].

Since these biological sensory systems may be modeled as nonlinear oscillators

(or coupled oscillator arrays), it is very important to discover what types of other phenomena are possible under the effects of noise. At the very least, new sensory technology is feasible.

Another type of stochastic resonance has also been exhibited by the foraging of ants [Dussutour, Beekman, Nicolis, and Meyer (2009)]. In this situation, ants will walk randomly. However, an ant will produce a pheromone trail, after finding a good food source, as it walks back to the nest. This weak signal, which dissipates over time, can be "boosted" if more ants take the same trail. This foraging technique has even been implemented as an optimization scheme, called Ant Colony Optimization [Dorigo and Blum (2005)]. This ability to "tune" the signal-to-noise ratio of the system is a distributed process, as there is no higher intelligence guiding the ants.

From the examples given, it is clear that noise enhanced performance (e.g., stochastic resonance) is a prevalent phenomenon in the physical world. Noise is a free source of energy, which biological systems harness to boost weak signals, synchronize brain patterns, and even forage for food. For mechanical systems, it is necessary to know what other types of noise-influenced dynamics are also possible.

1.3 Objectives

The principal objective of this work is to understand how noise influences the dynamics of several nonlinear systems, and to use this understanding to suggest designs of systems that utilize noise in an advantageous way. To better understand the effects of noise in combination with nonlinearity, it is intended to understand if noise can be used to move a system from one solution state to another, with the solution state not necessarily being an equilibrium position (as is the case with stochastic resonance).

To reach the objective, several nonlinear systems are studied, in order to find possible phenomenological effects of noise on nonlinear oscillators. These phenomena

include the following:

i) Instabilities caused by addition of noise;

ii) Effects of noise on energy localizations (e.g., intrinsic localized modes);

iii) Bifurcation of dynamic response into aperiodic motion, caused by addition of noise;

iv) Noise-induced energy attenuation.

In addition, a novel noise-utilizing control scheme, as well as the effects of phase lag on the information rate, are also studied. While the focus of the current work is directed towards macro-scale experiments, extensions to micro-scale devices (such as a microelectromechanical system (MEMS) array of oscillators or a MEMS sensor) is conceivable.

1.4 Outline

The rest of this dissertation is organized in the following manner. In Chapter 2, the inverted pendulum and Rayleigh-Duffing mixed type oscillator will be discussed [Perkins and Balachandran (2012, 2013)]. For the pendulum system, white Gaussian noise can cause a instability to occur. Similarly for the Rayleigh-Duffing system, white Gaussian noise can cause a transition to an aperiodic state to occur. A novel, noise-utilizing control scheme is also discussed, using the pendulum system as an example. In Chapter 3, the effects of phase lag on the information rate of a bistable Duffing oscillator undergoing stochastic resonance are described [Perkins and Balachandran (2015)]. In Chapter 4, preliminary results for energy localization in an array is discussed [Perkins and Balachandran (2012)]. In Chapter 5, noise-induced energy attenuation in a coupled oscillator array subjected to an impulse is examined [Perkins, Chabalko, and Balachandran (2013)]. In Chapter 6, the effects of noise and cubic coupling on intrinsic localized modes is explored [Balachandran, Perkins, and Fitzgerald (2014)]. In Chapter 7, experimental results showing the effect of noise on

the ILM hysteresis curve is presented, as well as simulation results [Perkins, Kimura, Hikihara, and Balachandran (2015)]. In Chapter 8, concluding remarks and future work are presented. Appendices containing derivations and programs used for this study are included.

Chapter 2

NOISE-INDUCED QUALITATIVE CHANGES AND NOISE-UTILIZING CONTROL SCHEME

In this chapter, the vertically excited pendulum is used as an example to illustrate the beneficial effects of noise. The upright equilibrium position of this system can be stabilized passively with a high-frequency excitation by utilizing the system nonlinearities and a bifurcation. After introducing white Gaussian noise into the pendulum pivot motion, the stability of the system prior to this bifurcation is analyzed. It is shown that white Gaussian noise has the potential to stabilize the unstable equilibrium point. Considering the bi-stable pendulum, a control scheme is introduced which utilizes only noise to switch between the two stable equilibrium points. This system is studied on the basis of an Itō scheme and direct numerical simulations are carried out by using the Euler-Maruyama method, and also with a semi-analytical formulation based on the Fokker-Planck equation. The results of the work can provide a basis to develop noise-utilizing controllers.

Additionally, the Rayleigh-Duffing system will be used to illustrate how the addition of noise to a deterministic input can push the system from a periodic attractor in the case without noise to a "broken-egg attractor" in the case with noise. This sytem was chosen in honor of Dr. Y. Ueda, whose pioneering work on the "broken egg attractor", helped establish a better understanding of chaos. These representative examples serve to illustrate a range of possible noise-influenced responses near bifurcation points. This work could allow the use of noise to be used as an energy-efficient control strategy.

The rest of this chapter is organized as follows. In the next section, a brief literature review of the pertinent systems is given. In Section 2.2, the equations gov-

Table 2.1: Nomenclature describing the quantities governing the pendulum.

θ	Pendulum angular displacement from upright position
ϕ_1	Pendulum position in state space
ϕ_2	Pendulum velocity in state space
g	Acceleration due to gravity
a	Forcing amplitude of pendulum system, $\frac{\tilde{a}}{l}$
Ω	Forcing frequency
l	Length of pendulum arm or rod
μ	Coefficient of viscous damping
ω^2	$\frac{g/l}{\Omega^2}$
$\dot{W}(t)$	White Gaussian noise (derivative of Wiener process)
σ	Noise amplitude
F	Forcing amplitude of Rayleigh-Duffing system
ν, γ	Rayleigh-Duffing mixed type equation parameters

erning the simple pendulum are derived. Euler-Maruyama simulations are presented in the following section. The Fokker-Planck equation and method of moments are shown in the subsequent section. By using the Euler-Maruyama method and the moment evolution equations, the behavior of this nonlinear system is explored and compared to that observed in the absence of noise. In Section 3, a noise-utilizing control scheme is then described and implemented. In Section 4, the Rayleigh-Duffing mixed type oscillator is presented and the response of this oscillator is examined. By using the Euler-Maruyama method and the aforementioned histograms of the Poincaré sections, the behaviour of this nonlinear system is explored and compared to that observed in the absence of noise. Concluding remarks are collected together in the final section.

2.1 Introduction and Background

Under only the influence of gravity, the upright position of the pendulum is an unstable equilibrium point. Control of the inverted pendulum is a classical problem in control theory. By using full-state feedback (angular displacement and angular velocity), lateral motions of the pivot can be used to control this system [Ogata (2001)]. Another method to stabilize the upright position of the pendulum is

achieved by driving the system harmonically in the vertical direction [Stephenson (1908)]. This second method is fundamentally different from the classical one, since it is based on an open-loop control scheme in which one exploits nonlinearities to stabilize the upright position. This method of control of the inverted pendulum is a specific problem in the field of vibration control [Meerkov (1977); Thomsen (2002); Yabuno, Miura, and Aoshima (2004)]. A treatment of the different responses of the parametrically excited pendulum is given in reference [Xu, Wiercigroch, and Cartmell (2005)], and the different responses include regular oscillations, rotations, and chaos.

For the inverted pendulum stabilized by a high-frequency excitation, in reference [Zhi-Long, Xiao-Ling, and Zi-Qi (2008)], it is shown that noise increases the largest Lyapunov exponent of the system, destabilizing the upward position. In another study [Wihstutz (1999)], perturbation methods are discussed for determining the Lyapunov exponents of linear systems. For the linearized pendulum equation, degenerate real noise is shown to stabilize the system [Wihstutz (2003)]. However, white noise alone cannot stabilize the upright position [Kao and Wihstutz (2000)]. For a pendulum in chaotic motion, noise addition can turn the motion into a regular motion, which terminates at the stable downward position [Lepik and Hein (2005)].

Here, the deterministic system with sinusoidal forcing is first presented, and then a white Gaussian noise component is included in the input. The pendulum system is integrated via an Itō scheme, and this allows for a numerical study by using the Euler-Maruyama method [Higham (2001)]. By using this method, one obtains an approximate solution of the system. This method is an extension of the Euler method for ordinary differential equations, which has been adapted to perform integrations of stochastic differential equations (SDEs). In addition, a Method of Moments analysis is also used to study the averaged dynamics of the system. Through this analysis, an approximation is obtained for the solution of the Fokker-Planck equation (a partial

differential equation) for the system, which governs the evolution of the probability density function of the states of the pendulum [Gardiner (1985)]. The moment evolution equations (an infinite set of ordinary differential equations) are derived from the Fokker-Planck equation [Socha (2007)] and truncated. As a part of the development, Taylor expansions of the harmonic terms are performed. A numerical solution of this truncated, finite set of ordinary differential equations provides an averaged (approximate) solution to the variables in state space.

The second system studied here is a Rayleigh-Duffing mixed type oscillator, which is a system studied by Dr. Y. Ueda in the 1960s. This system was shown to have a chaotic attractor in the form of a broken egg [Abraham and Ueda (2001)]. Since this system has had an important influence on developing an understanding of chaos, as a tribute to Dr Y. Ueda, this system was chosen to explore the effects of noise on the response of this oscillator.

In the case of the Rayleigh-Duffing mixed type oscillator, to visualize the influence of noise on the response, the Poincaré sections of this system are presented in the form of a two-dimensional histogram. By using this means of visualization, the stochastic dynamics of the system is believed to be portrayed in a meaningful way. This approach might serve as a useful tool in exploring the response of other

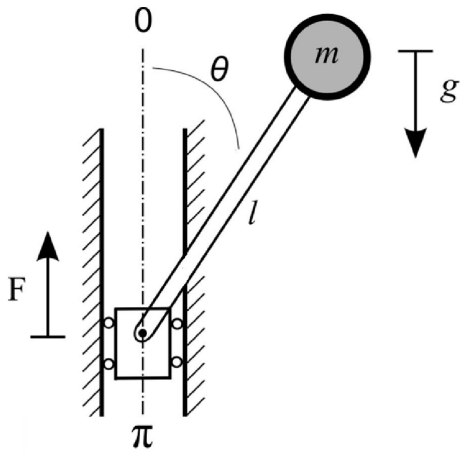

Figure 2.1: Planar pendulum subjected to vertical excitation. The symbols in this figure are listed in Table 2.1.

systems with noise component inclusions.

2.2 Pendulum Stabilization

2.2.1 System Equations

Under the influence of gravity, the equation of motion for a vertically and harmonically forced simple pendulum with a massless rod of length l and pendulum mass m takes the form:

$$\frac{d^2\theta}{dt^2} - \frac{g}{l}\sin\theta - \frac{\tilde{a}\Omega^2}{l}\sin\theta\cos\Omega t = 0 \tag{2.1}$$

After nondimensionalizing equation (2.1) and including a viscous damping term, the following is obtained

$$\ddot{\theta} + \mu\dot{\theta} - \omega^2\sin\theta - a\sin\theta\cos t = 0 \tag{2.2}$$

The nondimensionalized equation of motion with harmonic and stochastic forcing is given by

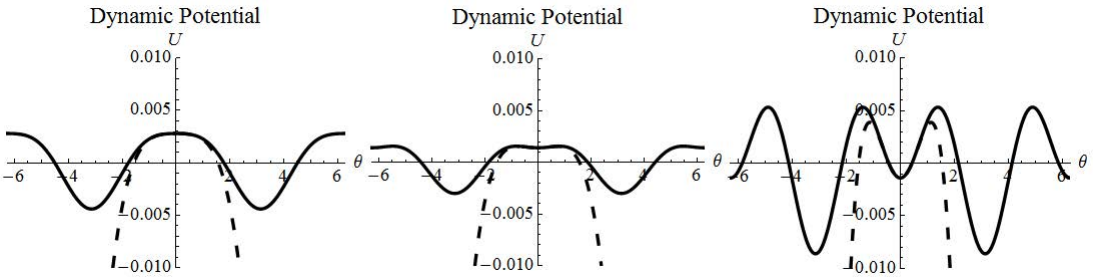

Figure 2.2: Dynamic potential approximation for the pendulum determined by using the method of multiple scales, as presented in Appendix A. A solid line is used to depict the multiple scales approximation and a dashed curve is used to depict a further approximation obtained with 3^{rd} order Taylor expansions of the harmonic terms. a) $a = 0.08, \omega = 0.06$, b) $a = 0.08, \omega = 0.047$, and c) $a = 0.2, \omega = 0.06$

$$\ddot{\theta} + \mu\dot{\theta} - \omega^2 \sin\theta - a \sin\theta[\cos t + \sigma\dot{W}(t)] = 0 \tag{2.3}$$

It is remarked that the noise excitation is multiplicative, due to the vertical nature of the excitation. By using the method of multiple scales [Nayfeh and Balachandran (1995)], for a system subjected to low-amplitude, high-frequency forcing, the dynamic potential function of the forced pendulum system can be approximated as

$$U(\theta) = \omega^2 \cos\theta - \frac{a^2}{8}\cos 2\theta \tag{2.4}$$

where the details on the construction of this function are provided in Appendix A. This function will be used to determine the stability of the deterministic pendulum, in the presence of the high-frequency forcing. Several graphs of this dynamic potential are presented in Figure 2.2. In subsequent sections, this function will be used to determine parameter values for which the top position is either stable or unstable.

2.2.2 Numerical Results

This pendulum is subjected to a deterministic forcing $a\cos t$ and a stochastic input $a\sigma\dot{W}(t)$, which is multiplicative with respect to the sine of the angular displacement. The term, $\dot{W}(t)$, denotes white noise, which is defined as the derivative of Brownian motion. Since Brownian motion (or in the physics literature, the Wiener process) has independent increments, its derivative does not exist with probability one [Chorin and Hald (2009)]. Thus, $\dot{W}(t)$ is a "mnemonic" derivative. To write the equations with more formality, the stochastic differential equations is converted into Langevin form. For facilitating the analysis, the equation of motion is first cast into a state-space form. In the subsequent notation, ϕ_1 and ϕ_2, respectively, correspond to the pendulum position and velocity in state space:

$$\begin{cases} \dot{\phi}_1 = \phi_2 \\ \dot{\phi}_2 = -\mu\phi_2 + \omega^2 \sin\phi_1 + a\sin\phi_1 \cos t + a\sigma \sin\phi_1 \dot{W}(t) \end{cases} \tag{2.5}$$

Next, the system of Langevin equations from this system of stochastic differential equations is written as

$$\begin{cases} d\phi_1 = \phi_2 dt \\ d\phi_2 = [-\mu\phi_2 + \omega^2 \sin\phi_1 + a\sin\phi_1 \cos t]dt + a\sigma \sin\phi_1 dW \end{cases} \tag{2.6}$$

Notice that in this differential form, one no longer has the derivative of Brownian motion (which does not exist) but a differential white noise which does exist. This system is integrated as an Itō integral. It should be noted that since there is parametric excitation, the Itō and Stratonovich integrations of this equation are not the same in general. Integrating equation (2.5) as a Stratonovich integral, the system is written as

$$\begin{cases} d\phi_1 = \phi_2 dt \\ d\phi_2 = [-\mu\phi_2 + \omega^2 \sin\phi_1 + a\sin\phi_1 \cos t]dt + a\sigma \sin\phi_1 \circ dW \end{cases} \tag{2.7}$$

where $\circ$ denotes integration in the Stratonovich sense. The Euler-Maruyama method can be used to obtain numerical solutions for equation (2.6), while the Euler-Heun method can be used to obtain numerical solutions for equation (2.7).

In each of the graphs shown in Figures 2.3 and 2.4, the simulations were initiated with a small initial displacement. As can be seen in Figures 2.3(a) and 2.4(a), for the considered parameter values, the upright position of the pendulum is not stable, as mentioned in the previous subsection. However, by adding a low amplitude noise, the pendulum is caused to stay in the upright position as seen in Figures 2.3(b) and 2.4(b). If one is operating just below the bifurcation point (i.e., if the amplitude level of the sinusoidal forcing is too low to stabilize the upright position), noise can help stabilize this pendulum system in the upright position, for at least finite time intervals.

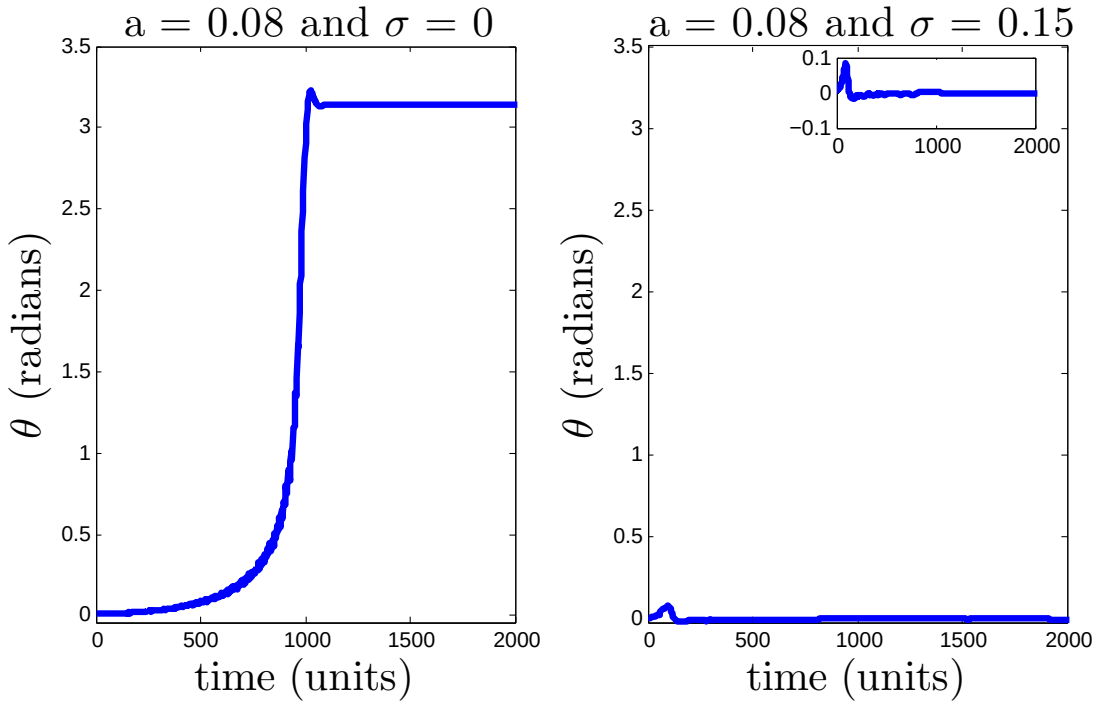

Figure 2.3: Euler-Maruyama results for $\omega = 0.06$, $\mu = 0.1$, and $a = 0.08$. a) With no noise, the pendulum falls from the upright position ($\theta = 0$ radians) to the bottom position ($\theta = \pi$ radians). b) With a low level of noise, the pendulum remains in the upright position for the finite duration considered. These results are to be compared with those presented later in Figure 2.6.

As shown in Figure 2.5, with a deterministic forcing, the upright position can be stabilized. By considering only noise of amplitude $\sigma = 2.0$ in the forcing, the pendulum still settles to the downward position. However, if the upright position is stabilized with a driving amplitude of $a = 0.2$, noise of the same amplitude as previously used can cause the pendulum to enter periods of complete rotations. In other words, if only the downward position is stable, white noise alone cannot stabilize the upright position (which is also noted in the study of [Kao and Wihstutz (2000)]); however, if a sinusoidal forcing stabilizes the upright position, the noise causes motions between the two stable equilibrium points (periods of rotations). This could be useful for energy harvesting applications, as the noise can cause large movements in the bi-stable system.

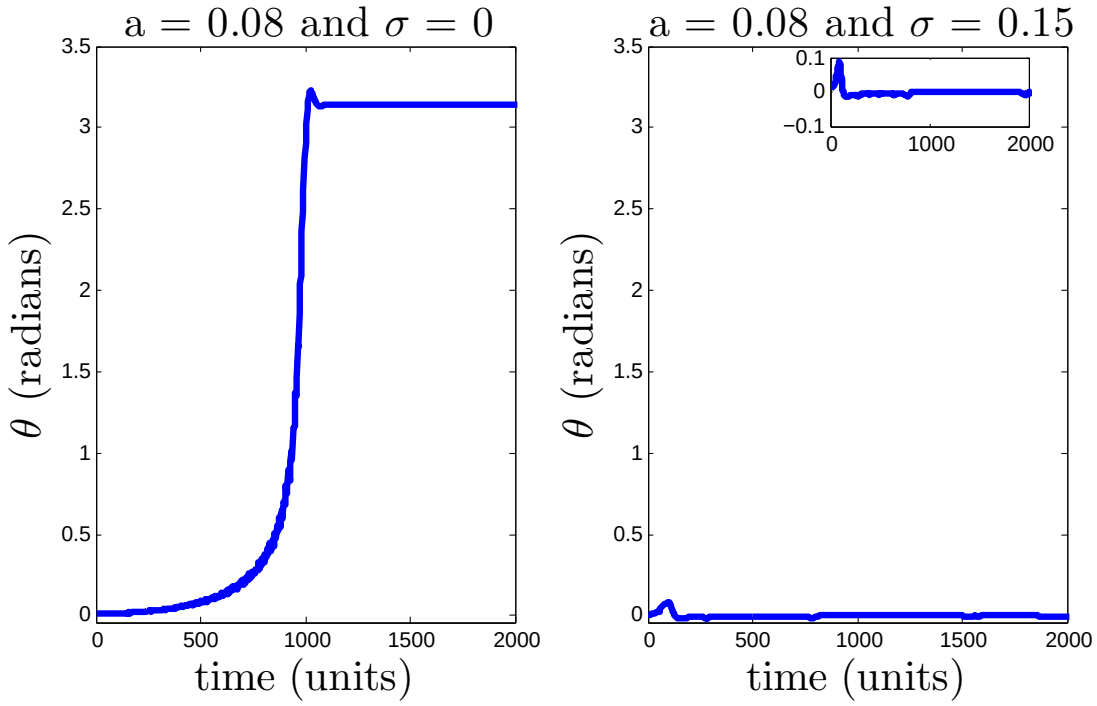

Figure 2.4: Euler-Heun results for $\omega = 0.06$, $\mu = 0.1$, and $a = 0.08$. a) With no noise, the pendulum falls from the upright position ($\theta = 0$ radians) to the bottom position ($\theta = \pi$ radians). b) With a low level noise, the pendulum remains in the upright position for the finite duration considered. Notice that in this case, the simulation results are qualitatively similar to those found in Figure 2.3.

2.2.3 Fokker-Planck Equation and Method of Moments Analysis

In the preceding subsection, the use of white noise to stabilize the unstable upright position of the pendulum was demonstrated. In this subsection, the aim is to obtain an approximate solution on the basis of a formalism based on the Fokker-Planck equation [Gardiner (1985)]. The solution of this partial differential equation is the time evolution of the probability density function, which is a function of the variables in state space and of time. The Fokker-Planck equation can be written as

$$\partial_t p = -\Sigma_j \partial_j [A_j(\mathbf{x}, t)p] + \tfrac{1}{2}\Sigma_{j,k}\partial_j\partial_k [B(\mathbf{x}, t)B^T(\mathbf{x}, t)]_{j,k}p \tag{2.8}$$

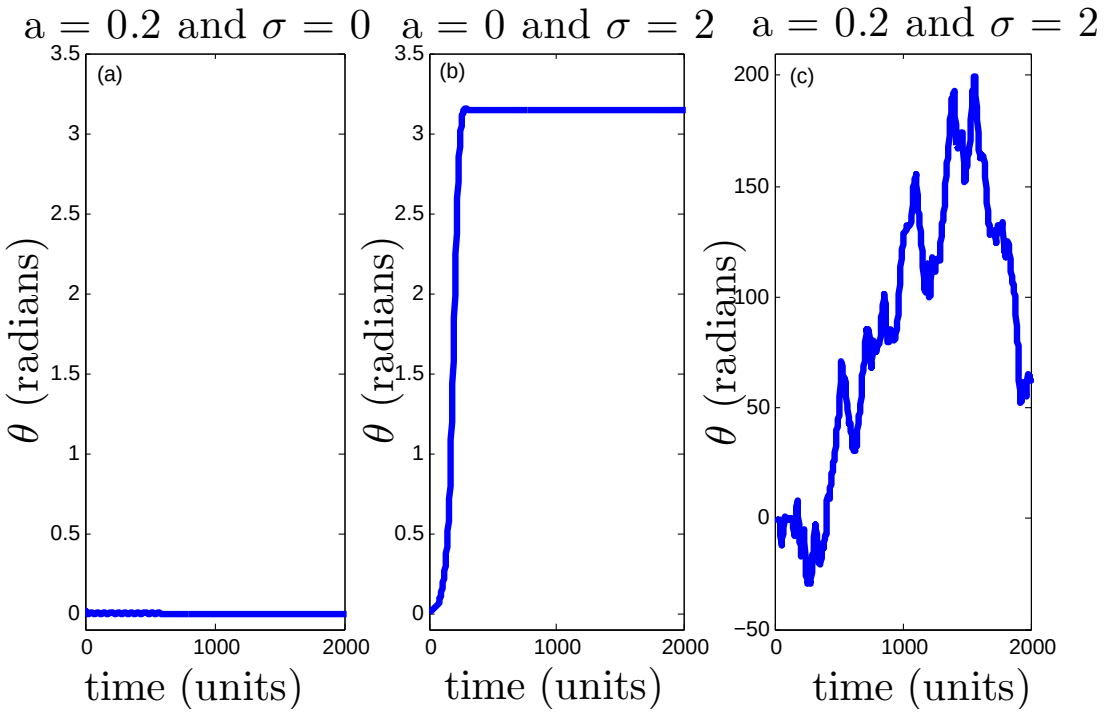

Figure 2.5: Results with and without deterministic components in the input. a) With only deterministic forcing, the upright position is stable, and the pendulum approaches the top position. b) With only noise, in this case with $\sigma = 2.0$, the upright position is unstable, and the pendulum approaches the bottom position. c) With a forcing amplitude that stabilizes the upright position and the same noise level, the pendulum is sent into periods of full rotations.

where, $\mathbf{x}$ is the vector of variables in state space, $p = p(\mathbf{x}, t)$ is the probability density function, $A_j(\mathbf{x}, t)$ is the vector containing the deterministic parts of equation (2.6), and $B(\mathbf{x}, t)$ is the vector containing the stochastic parts of equation (2.6). The Fokker-Planck equation for the pendulum can then be straightforwardly constructed as

$$\partial_t p = -\partial_{\phi_1}(\phi_2 p) - \partial_{\phi_2}([-\mu\phi_2 + \omega^2 \sin\phi_1 + a \sin\phi_1 \cos t]p) + \frac{1}{2}\partial^2_{\phi_2}(a^2\sigma^2 \sin^2\phi_1 p) \tag{2.9}$$

To find an approximate solution for equation (2.8), the Method of Moments is employed [Socha (2007)]. To briefly explain this method, first consider the general moment equation:

$$< g >= \int \int gpdx_1dx_2 \tag{2.10}$$

Then, obtaining the moment as it evolves through time, it is found that

$$\frac{d < g >}{dt} = \int \int g\frac{dp}{dt}dx_1dx_2 \tag{2.11}$$

Now, replacing g with the r^{th} moment of position and the s^{th} moment of velocity of the pendulum, the result is

$$\frac{d < \phi_1^r\phi_2^s >}{dt} = \int \int \phi_1^r\phi_2^s\frac{dp}{dt}d\phi_1d\phi_2 \tag{2.12}$$

After substitution and rearrangement, the moment evolution equation for the pendulum is obtained:

$$\begin{aligned} \tfrac{d}{dt} < \phi_1^r\phi_2^s >= r < \phi_1^{r-1}\phi_2^{s+1} > -\mu s < \phi_1^r\phi_2^s > \\ +(\omega^2 s + as\cos t) < \phi_1^r \sin\phi_1\phi_2^{s-1} > \\ +\tfrac{a^2\sigma^2}{2}s(s-1) < \phi_1^r \sin^2\phi_1\phi_2^{s-2} > \end{aligned} \tag{2.13}$$

On substitution of different values of r and s, this moment evolution equation gives an infinite set of ODEs. For instance, the ODE corresponding to the time derivative of the second moment of velocity (i.e., $r = 0, s = 2$) is expressed in terms of the fourth moment of position because of the $\sin^2\phi_1$ term. The following two approximations are made, in order to solve this infinite set of ODEs: i) a 3^{rd} degree Taylor expansion is used to approximate $\sin\phi_1$ about the upright equilibrium point (an expansion about $\phi_1 = 0$ radians) to obtain approximate solutions about this point, and ii) moments of order 3 and higher are neglected via the cumulant neglect method [Socha (2007)]. It should be noted that the states are not considered to be independent (i.e., $< \phi_1^r\phi_2^s > \neq < \phi_1^r >< \phi_2^s >$). These approximations yield a set of 5 ODEs, from the Fokker-Planck PDE. The numerical results obtained with this reduced-order system are presented in Figure 2.6.

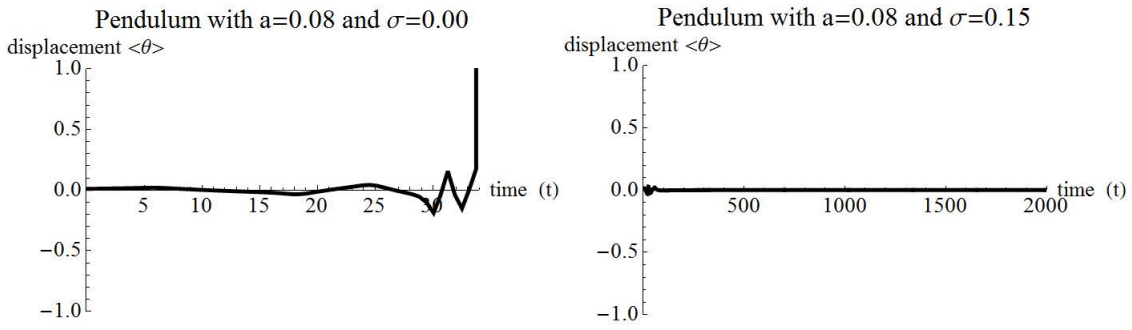

Figure 2.6: The average displacement obtained from the moment evolution equation is presented here. a) Without noise, the pendulum moves away from the unstable equilibrium point. b) With noise, the average displacement of the pendulum stays near the previously unstable equilibrium point. These cases may be compared with those in Figures 2.3 and 2.4.

In Figure 2.6(a), the average displacement of the pendulum is shown to move from the unstable equilibrium position, $\theta = 0$ radians, when there is no noise. It is noted that since the Taylor expansion is to 3^{rd} degree about the point $\phi_1 = 0$ radians, the solution is only valid in the range of $-1.0rad < \theta < 1.0rad$. Since this is a truncated model, the instability happens in a shorter amount of time, as compared to the Euler-Maruyama simulation in Figure 2.3(a). In Figure 2.6(b), the solution is stabilized (for at least a finite time) about the unstable equilibrium position, similar to that discussed in the previous section and shown in Figure 2.3(b).

2.3 Noise-utilizing Controller

Here, a novel controller for the bi-stable pendulum is presented, which could be extended with ease to other multi-stable systems. The controller is defined with the following logic: if the system is in an undesirable well, the noise amplitude is positive; and if the system is in the desired well, the noise amplitude is set to zero. To steer the system response to the upward position, the controller C_{up} is implemented; and to steer the system response to the bottom position, the controller C_{down} is implemented. The control scheme is written symbolically for the pendulum

as follows, where $\wedge$ is the "AND" operator and $\vee$ is the "OR" operator:

$$C_{up} = \begin{cases} \sigma > 0, \quad if\ [\frac{\phi_2^2}{2} + \omega^2 \cos\phi_1 - \frac{a^2}{8}\cos 2\phi_1 < U(\phi_1^*)] \\ \qquad\qquad \wedge[(mod(|\phi_1|, 2\pi) < \phi_1^*) \\ \qquad\qquad \vee(mod(|\phi_1|, 2\pi) > (2\pi - \phi_1^*))] \\ \sigma = 0, \qquad\qquad otherwise \end{cases} \tag{2.14}$$

$$C_{down} = \begin{cases} \sigma > 0, \quad if\ [\frac{\phi_2^2}{2} + \omega^2 \cos\phi_1 - \frac{a^2}{8}\cos 2\phi_1 < U(\phi_1^*)] \\ \qquad\qquad \wedge[(mod(|\phi_1|, 2\pi) > \phi_1^*) \\ \qquad\qquad \wedge(mod(|\phi_1|, 2\pi) < (2\pi - \phi_1^*))] \\ \sigma = 0, \qquad\qquad otherwise \end{cases} \tag{2.15}$$

Here, ϕ_1^* is the value of ϕ_1 such that $0 < \phi_1^* < \pi$ and $U(\phi_1^*) = Max(U)$. For the pendulum system, with parameters such that the upright and downward positions are both stable (say, $a = 0.08, \omega = 0.047, \mu = 0.01$), this controller can be used to move the system from one well to the other. For the case presented in Figure 2.7, $\phi_1^* = 0.808871$ and $U(\phi_1^*) = 0.0015$, as seen from Figure 2.2(b). For the case presented in Figure 2.8, $\phi_1^* = 1.38981$ and $U(\phi_1^*) = 0.0053$, as seen from Figure 2.2(c). This control scheme utilizes noise to move the system to a desired stable equilibrium position, while ensuring that the system does not have enough energy to leave the desired position's dynamic potential well. The simulation results shown in Figures 2.7 and 2.8 were obtained by using the Euler-Maruyama method, as described in the second section, together with the described controller.

2.4 Qualitative Changes in Aperiodic Behavior of Rayleigh-Duffing System

In the previous section, the effects of noise on the response of a vertically-excited pendulum were discussed. Here, in honor of Dr. Y. Ueda, the effects of noise on the Rayleigh-Duffing oscillator are explored. This oscillator is described by

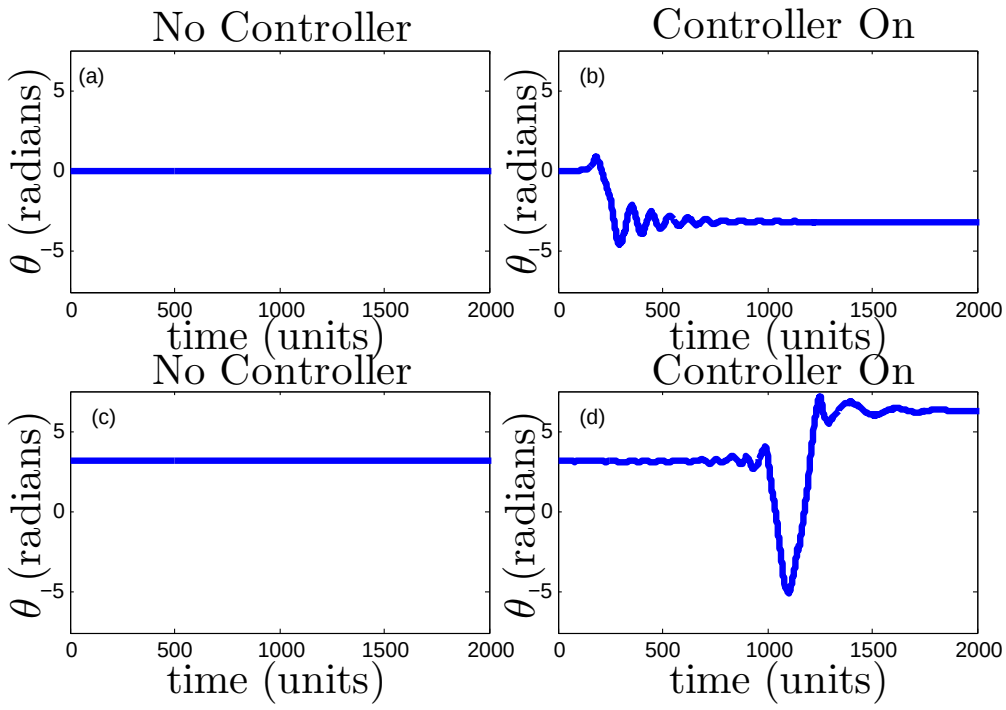

Figure 2.7: For $a = 0.08$ and $\omega = 0.047$, whose dynamic potential is shown in Figure 2.2(b). a) The system is stable about the upright position. b) With the controller, the pendulum is pushed to the bottom position. c) The system is stable about the bottom position. d) With the controller, the pendulum is pushed to the upright position (mod 2π).

$$\frac{d^2x}{dt^2} - \nu(1 - \gamma(\frac{dx}{dt})^2)\frac{dx}{dt} + x^3 = Fsin(\Omega t) + \sigma\dot{W}(t) \tag{2.16}$$

As before, the system has a superposition of deterministic and stochastic forcing ($Fsin(\Omega t)$ and $\sigma\dot{W}(t)$, respectively). For the parameter values $\nu = 0.2$, $\gamma = 4.0$, $F = 0.3$, and $\Omega = 1.1$, the deterministic counterpart of this system (i.e., the system without noise) exhibits the broken-egg chaotic attractor [Higham (2001)]. As discussed in Section 2.2, this equation can be written in Langevin form, and using this form, an Euler-Maruyama simulation can be implemented. By keeping the other parameters at the aforementioned values, but reducing the forcing constant to $F = 0.166$, it is found that the motion of the oscillator is periodic.

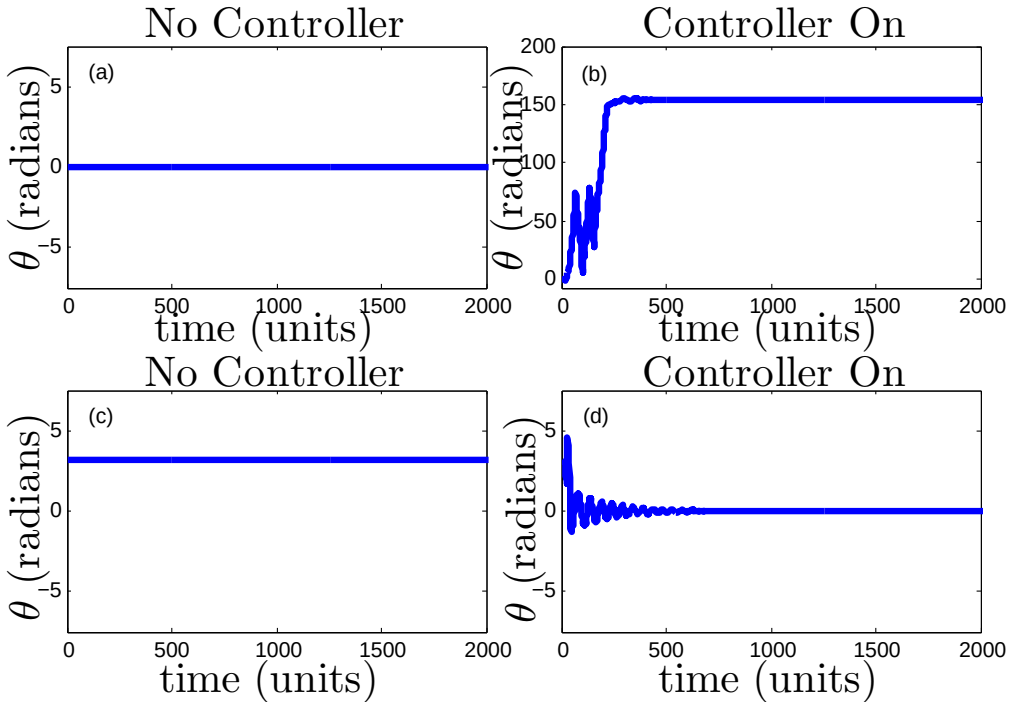

Figure 2.8: For $a = 0.2, \omega = 0.06$, whose dynamic potential is shown in Figure 2.2(c). a) The system is stable about the upright position. b) With the controller, the pendulum is pushed to the bottom position. c) The system is stable about the bottom position. d) With the controller, the pendulum is pushed to the upright position (mod 2π).

It is noted that in Figure 2.9, a two-dimensional histogram is taken of the Poincaré sections of the Euler-Maruyama simulation. The clock frequency used to construct the Poincaré section is taken to be the forcing frequency. In the histograms presented, the color coding shows how many points from the Poincaré sections lie within each small box of the state space in a given amount of time, where x refers to position and v refers to velocity. On top of this histogram, the broken-egg attractor with the parameter values given above is graphed also for direct comparison. As noise is added to the Rayleigh-Duffing mixed type oscillator, the oscillator progresses from periodic motion to something that appears to be "quasiperiodic" or "chaotic," in an average sense. This method of visualization might be useful for other systems that have stochastic components. Since there are many attracting sets between

the parameter values $F = 0.166$ and $F = 0.3$, the response of the oscillator is best thought of in an average sense: the noise pushes the response between many different attracting sets, which are close to each other. In an average sense, in going from Figure 2.9(b) to Figure 2.9(c), the noise pushes the system response to what also looks like a broken-egg form; the noise breaks the egg shape form observed in Figure 2.9(b). It is recalled that in the absence of noise, the response is periodic as noted in Figure 2.9(a). For relatively large levels of noise, the state of the system begins to fill a portion of the state space, centered about the origin.

2.4.1 Lyapunov Exponent

Although the graphs from Figure 2.9 seem to imply that noise might push the system into a chaotic regime, a calculation of the largest Lyapunov exponent elucidates this more clearly. A calculation method for the largest Lyapunov exponent which is robust to noise was used to approximate this metric from the data presented in Figure 2.9 [Rosenstein *et al.* (1993)]. Calculations carried out with this method yield $\lambda_1 \approx 0$ for the case of no noise, which is consistent with the fact that the system exhibits a stable limit cycle. For the case of $\sigma = 0.05$, this calculation gave that $\lambda_1 \approx 0.38 > 0$. Thus, it seems reasonable that noise does push this system into a region of chaotic behavior.

2.5 Concluding Remarks

In this chapter, several aspects of the influence of noise on the dynamics of a planar pendulum subjected to a vertical forcing is explored. Through numerical simulations, it has been shown that a low level of noise can help stabilize the upright position, when the forcing amplitude is close to the critical value at the bifurcation point of the deterministic system. Also, it is shown that noise can be used to

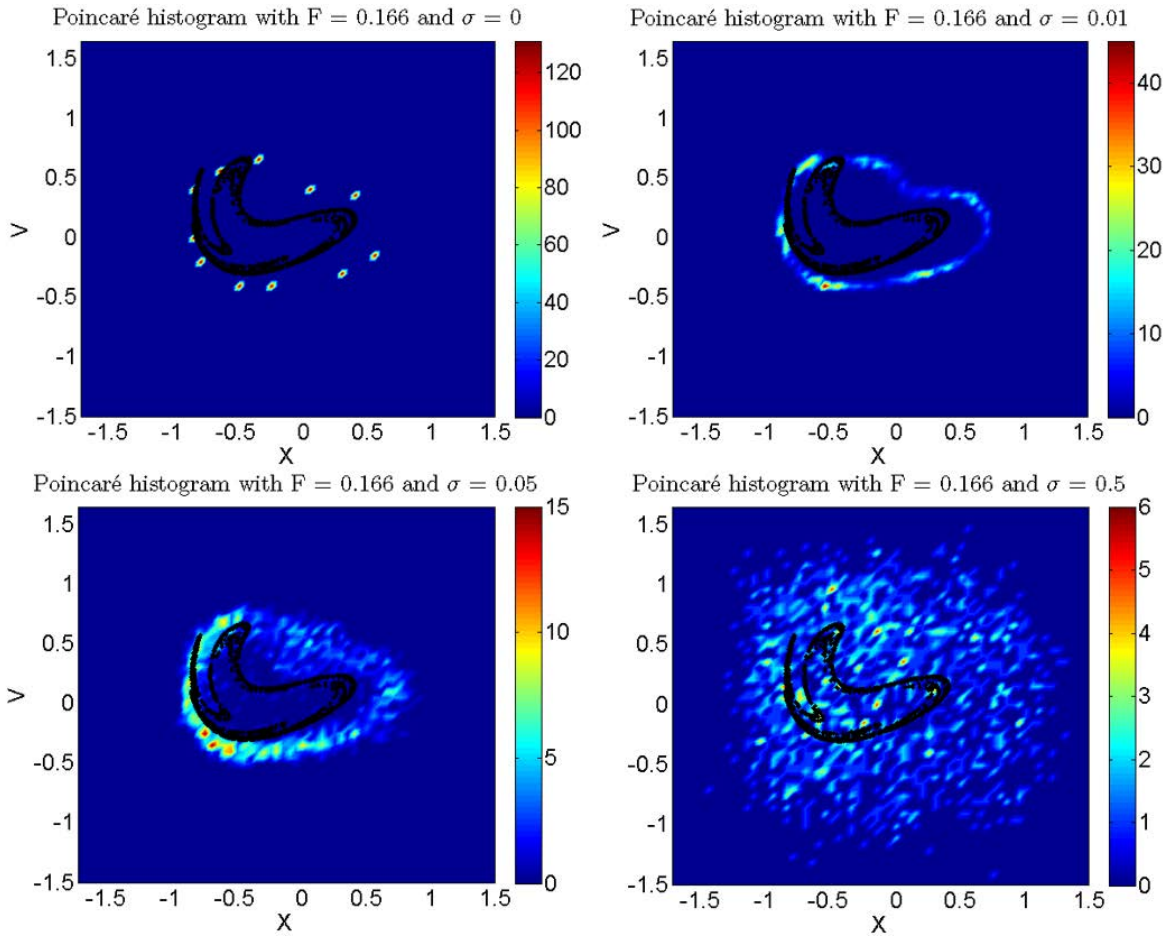

Figure 2.9: Illustration of the broken-egg attractor along with the different responses on the Poincaré section constructed by using the forcing frequency as the clock frequency: a) With no noise, the motion of the oscillator is periodic, as illustrated by the discrete set of points. b) With a low level of noise, a curve in the state space is traced. c) With the noise level at $\sigma = 0.05$, the Poincaré sections are, on average, on an egg-like shape which encircles the broken-egg attractor. d) With higher levels of noise, the oscillator's response fills a large, sparsely populated area.

push the pendulum system into periods of rotation. The author believes that this aspect of noise could be utilized to harvest energy from this system by storing the rotational energy. After deriving the Fokker-Planck equation and the moment evolution equation, the author numerically found an approximate solution to the moment evolution equation. Through this analysis, it has been shown that the average displacement of the pendulum can be stabilized (at least over a finite time interval) about the unstable upright position. This has been done by using white

noise before the onset of the bifurcation associated with the upright position in the deterministic case.

Through studies of the Rayleigh-Duffing mixed type oscillator, it has been shown that the addition of noise can promote an early appearance of dynamic response in an average sense, which previously did not exist in the corresponding noise-free case. Poincaré sections were constructed for the numerically obtained responses from the Euler-Maruyama simulation. A two-dimensional histogram was used to visualize this data and compare it to the broken-egg chaotic attractor that is known to occur in this system. It is noted that the noise inclusion caused the system response to progress from a periodic motion to a motion that appears to be "quasiperiodic" or "chaotic". The histograms can be taken to show the average dynamics of the system. For the deterministic case, the histogram is simply the same as that obtained with the usual constructions of Poincaré sections. As noise is added, the system dynamics moves between different attracting sets (there appear to be many attracting sets between $F = 0.166$ and $F = 0.3$). Eventually, the noise overpowers the attracting sets, and the system response fills a portion of the state space. These results suggest that an optimal level of noise may exist, which can be used to control/confine the system response to different attracting sets.

The author believes that the noise-utilizing controller can be used for many other systems with two or more equilibrium solutions. Since the influence of noise is quite prevalent at the micro-scale, this controller might be implemented through a converse method: if the system is in an undesirable position, one should not filter the noise; if the system is in a desirable position, one can filter the noise from the system. In many situations, noise is considered to be undesirable. As shown in this study, there are several ways through which noise can influence the dynamics of the pendulum in an advantageous manner. By understanding the noise-influenced dynamics of the pendulum, parameters could be designed to utilize these stochastic

components.

Chapter 3

EFFECTS OF PHASE LAG ON THE INFORMATION RATE OF A BISTABLE DUFFING OSCILLATOR

To utilize noise for systems, which are transmitting or receiving information, the information rate is a necessary metric to consider. The phase lag, which is the difference between the sender (applied forcing) and receiver (the oscillator) phases, has a significant effect on the information rate. However, this phase lag is a nonlinear function of the noise level. Here, the effects of phase lag on the information rate for a Duffing oscillator are examined and comparative discussions are made with phase lag from linear response theory. The phase lag is shown to be an important variable in calculating the information rate.

The rest of this chapter is organized as follows. In the next section, a brief literature review of pertinent information theory is discussed. In Section 3.2, the equations governing the nondimensionalized bistable Duffing oscillator are discussed. Euler-Maruyama simulations are presented in the following section, as well as the approach used to convert the continuous system response into a binary signal. The Fokker-Planck equation and cumulant neglect method are presented in the subsequent section. By using the Euler-Maruyama method and the moment evolution equations, the information rate is used to assess the influence of noise on the system response. By considering the phase lag as a parameter in calculating the information rate, a relationship amongst the phase lag, noise amplitude, and information rate is shown. Concluding remarks are collected together in the final section.

Table 3.1: Nomenclature describing the quantities governing the bistable Duffing oscillator.

x	Oscillator displacement
x_1	Oscillator position in state space
x_2	Oscillator velocity in state space
c	Viscous damping
ζ	Damping ratio
k_1	Linear stiffness
k_3	Nonlinear stiffness
$\hat{K}$	Nondimensionalized stiffness
Ω	Forcing frequency
$\hat{\Omega}$	Nondimensionalized forcing frequency
ω_n	Natural frequency
$\dot{W}(t)$	White Gaussian noise (derivative of Wiener process)
$\hat{\sigma}$	Nondimensionalized noise amplitude

3.1 Introduction and Background

Stochastic resonance has been classically identified as a peak in the signal-to-noise ratio [Gammaitoni *et al.* (1998)], when a response measure is plotted against the amplitude of noise. This phenomenon, which has been used to describe the effects of noise on the recurrence of ice ages [Benzi *et al.* (1981)], was first studied in the context of a bistable Duffing oscillator [Gammaitoni *et al.* (1998)] and also shown to have an important effect on the response of a monostable Duffing oscillator [Stocks, Stein, and McClintock (1993)]. Recently, stochastic resonance has been studied in a macroscale, distributed parameter system, a post-buckled beam [Wiebe and Spottswood (2014)]. The integrate-and-fire model for neurons exhibit the behavior shown by a monostable Duffing oscillator [Wiesenfeld and Moss (1995)].

Since Shannon's seminal information theory work [Shannon and Weaver (1948)], information theoretic techniques have been applied to many different systems. A binary channel has been studied by using information capacity [Chapeau-Blondeau (1997)]. In experimental work, mutual information has been used to show broadband stochastic resonance in a neuron [Levin and Miller (1996)]. The channel capacity has also been used to detect the occurrence of stochastic resonance in a neuron

model [Kish, Harmer, and Abbott (2001)], where it was noted that the location of the channel capacity maximum occurs at a higher noise amplitude than does the maximum of the signal-to-noise ratio (SNR). In the present chapter, a similar result is obtained. Furthermore, for different phase lags, the peak is found to occur at different noise amplitudes. For a neuron model, aperiodic stochastic resonance has been measured by using mutual information [Bulsara and Zador (1996)]. Also,this measure was used to study a neuron undergoing adaptive stochastic resonance [Mitaim and Kosko (2004)]. Simulations have also been carried out with a bistable dynamic system by using an Euler discretization scheme, revealing a single peak in the channel capacity [Godivier and Chapeau-Blondeau (1998)]. After converting input and output signals to binary sequences, experimental data from a Schmitt trigger have been shown to exhibit extrema when studied with Conditional and Kullback entropies [Neiman, Shulgin, Anishchenko, Ebeling, Schimansky-Geier, and Freund (1996)]. For weak forcing and noise variance, the behavior of the normal form equation was examined by using mutual information [Nicolis and Nicolis (2000)]. The Fisher information measure has also been used to study responses of a parallel array of sensors [Chapeau-Blondeau *et al.* (2006)]. Entropy measures for several dynamical systems, including a linear oscillator, are discussed in reference [Sobczyk (2001)].

3.2 System Equations

The equation of motion governing a bistable Duffing oscillator with mass m, viscous damping c, linear stiffness k_1, nonlinear stiffness k_3, forcing amplitude F, and forcing frequency Ω can be written as

$$m\ddot{x} + c\dot{x} - k_1 x + k_3 x^3 = F\sin(\Omega t) \tag{3.1}$$

where all of the parameters assume positive values and an overdot indicates differentiation with respect to time t. After dividing equation (3.1) by m and introducing a nondimensional time $\tau = \omega_n t$, the resulting equation takes the form

$$\omega_n^2 \frac{d^2x}{d\tau^2} + 2\zeta\omega_n^2 \frac{dx}{d\tau} - \omega_n^2 x + \frac{k_3}{m}x^3 = \frac{F}{m}\sin(\frac{\Omega}{\omega_n}\tau) \tag{3.2}$$

Dividing through by ω_n^2 and introducing primes to indicate differentiation with respect to the nondimensional time τ, the result is

$$x'' + 2\zeta x' - x + \frac{k_3}{k_1}x^3 = \frac{F}{k_1} sin(\frac{\Omega}{\omega_n}\tau) \tag{3.3}$$

Finally, after substituting the nondimensional parameters $\hat{K} = \frac{k_3}{k_1}$, $\hat{F} = \frac{F}{k_1}$, and $\hat{\Omega} = \frac{\Omega}{\omega_n}$, the equation becomes

$$x'' + 2\zeta x' - x + \hat{K}x^3 = \hat{F} sin(\hat{\Omega}\tau) \tag{3.4}$$

After including nondimensional noise, the stochastic differential equation (SDE) for the nondimensionalized bistable Duffing equation is modified to

$$x'' + 2\zeta x' - x + \hat{K}x^3 = \hat{F} sin(\hat{\Omega}\tau) + \hat{\sigma}\dot{W}(\tau) \tag{3.5}$$

3.3 Numerical Results

In equation (3.5), the oscillator is subjected to a deterministic forcing $\hat{F}\sin(t)$ and a stochastic input $\hat{\sigma}\dot{W}(\tau)$. Writing in state-space form, one obtains

$$\begin{cases} \frac{dx_1}{d\tau} = x_2 \\ \frac{dx_2}{d\tau} = -2\zeta x_2 + x_1 - \hat{K}x_1^3 + \hat{F} sin(\hat{\Omega}\tau) + \hat{\sigma}\dot{W}(\tau), \end{cases} \tag{3.6}$$

where x_1 and x_2 correspond to the position and velocity, respectively. The white noise term, $\dot{W}(t)$, is defined as the derivative of Brownian motion. Since Brownian motion

(or in the physics literature, the Wiener process) has independent increments, as also mentioned in the previous chapter, its derivative does not exist with probability one [Chorin and Hald (2009)]. For this reason, $\dot{W}(t)$ is a "mnemonic" derivative. Hence, writing equation (3.6) in differential form, one has

$$\begin{cases} dx_1 = x_2 d\tau \\ dx_2 = [-2\zeta x_2 + x_1 - \hat{K}x_1^3 + \hat{F}sin(\hat{\Omega}\tau)]d\tau + \hat{\sigma}dW \end{cases} \tag{3.7}$$

In this form, one no longer has the derivative of Brownian motion but a differential white noise which does exist. This system is integrated as an Itō integral, and the Euler-Maruyama method can be used to obtain numerical solutions for equation (3.7) [Higham (2001)]. These simulations were performed on a desktop computer, with a 4.00 GHz processor, by using MATLAB. Although this code was not optimized for speed, it took approximately 7.6 hours of wall time to run the 200 Euler-Maruyama simulations for each of the 100 noise amplitudes considered and to do the subsequent averaging. A sample code for the Euler-Maruyama simulation and the cumulant neglect method is given in Appendix B.

The information rate R is defined as

$$R = H(x) - H_y(x), \tag{3.8}$$

where the Shannon entropy is $H(x) = -\Sigma_i p_i log_2 p_i$ and the conditional entropy is $H_y(x) = -\Sigma_{i,j} p(i,j) log_2 p_i(j)$, where $p_i(j) = \frac{p(i,j)}{\Sigma_j p(i,j)}$. Since the Duffing oscillator response is a continuous time response, one needs to convert the oscillator's position response into a binary output, before the associated information rate can be computed. A natural choice is to represent displacements below zero with"0" and displacements above zero with "1". With this choice, the positive piece of an input sine wave from 0 to π would be considered as one instance of "1". Thus, averaging over this range is sufficient to convert the continuous signal into a binary signal. However, given the

inherent delay in an input-output relationship, care must be exercised in choosing a phase lag for the continuous output signal, before converting it into a binary one. In this chapter, phase lag constants for different noise amplitudes are considered and their effects are examined. An example of this process for the no noise and no phase lag case is presented in Figure 3.1. In the first part of this figure, the forcing input, in black color, and the output response, in grey color, are both plotted. In the middle part of this figure, the binary conversion scheme is implemented as previously discussed. In the bottom part of this figure, the binary displacements have been averaged over sections of one half period of the forcing frequency. After this was done, if the averaged binary displacement over that length of time was above "0", it was converted to a bit value of "1". If the averaged binary displacement over that length of time was below "0", it was converted to a bit value of "0". By shifting the half period sections to be averaged (i.e., by changing the phase lag), different averages and subsequent bit values can be obtained and studied.

In Figures 3.2 and 3.3, the computed mean information rate for 200 simulations is shown, over a noise level range. The effects of different phase lag values can be seen in both figures. In Figure 3.4, the maximal information rate is plotted against the noise amplitude, along with the phase lag amount that maximizes the information rate. Interestingly, the phase lag graph is not monotonic. When a case with no phase lag is considered, a double peak can be observed in the information rate, as shown in Figure 3.5. The position of the peak in Figure 3.4 may be compared with the that shown in Figure 3.10; this will be discussed later.

3.4 Fokker-Planck Equation and Method of Moments Analysis

In the preceding subsection, the influence of white noise was measured by using Shannon's information rate. In this section, an approximate solution is obtained on the basis of a Fokker-Planck formalism. The solution of this partial differential

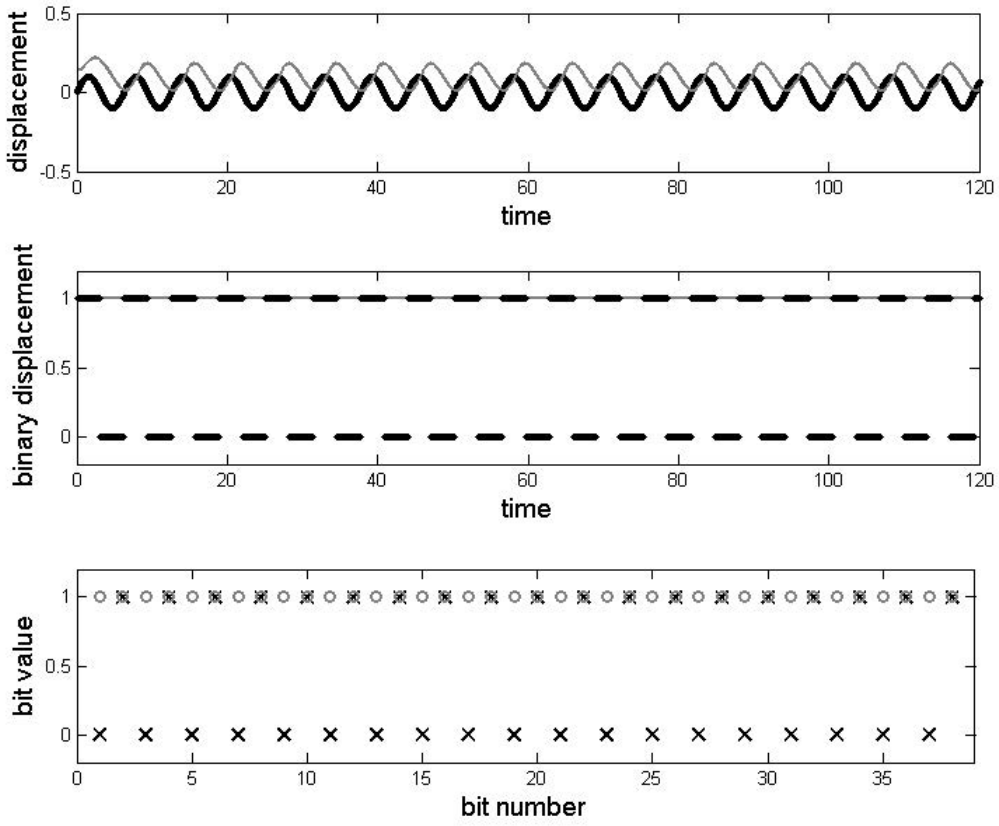

Figure 3.1: Euler-Maruyama simulation of bistable Duffing oscillator, with no noise. Black color (with black Xs in the bottom graph) is used for the input signal, and grey color (with grey circles in the bottom graph) is used for the oscillator response signal. The middle graph shows the result of converting the positions to zeros or ones, as described in the text. The bottom graph has been averaged and converted to discrete bits. There is no phase lag in this case.

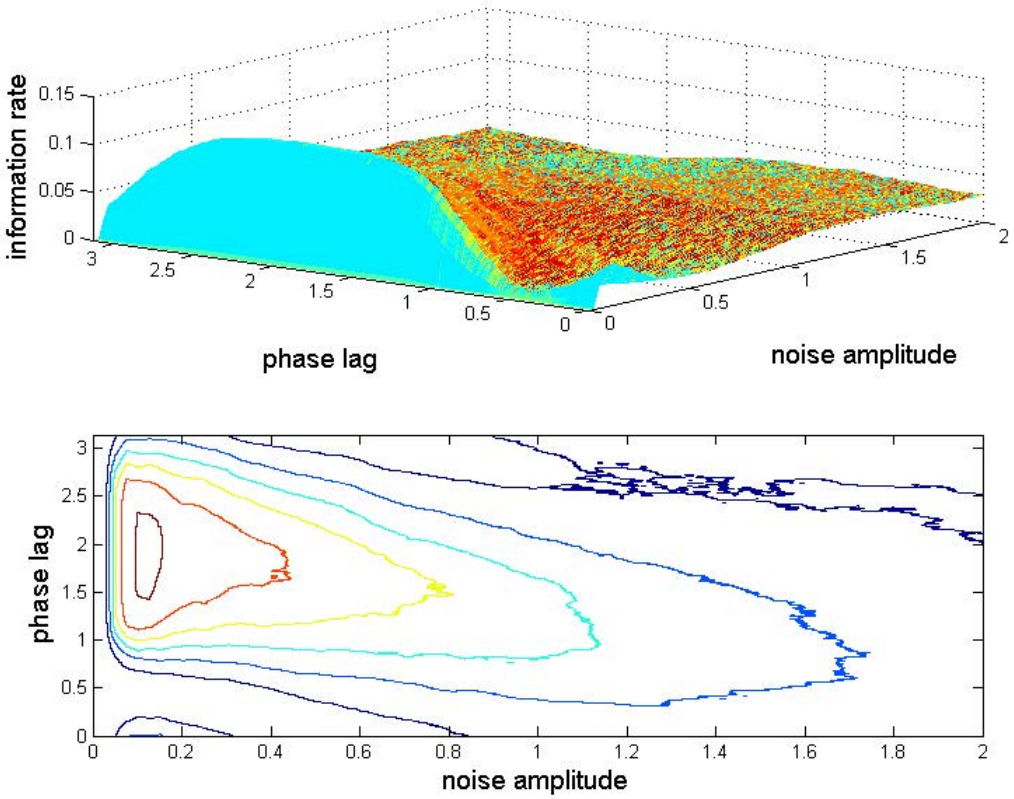

Figure 3.2: The mean information rate has been computed for 200 simulations, for a range of noise levels. Different phase lags give drastically different values for the information rate. This same information is presented as a contour plot, in order to show that the backbone of the peak falls along the phase lag axis, as the noise amplitude is increased. The parameters used for these simulations are as follows: $\zeta = 2, \hat{K} = 50, \hat{F} = 0.35$, and $\hat{\Omega} = 1$.

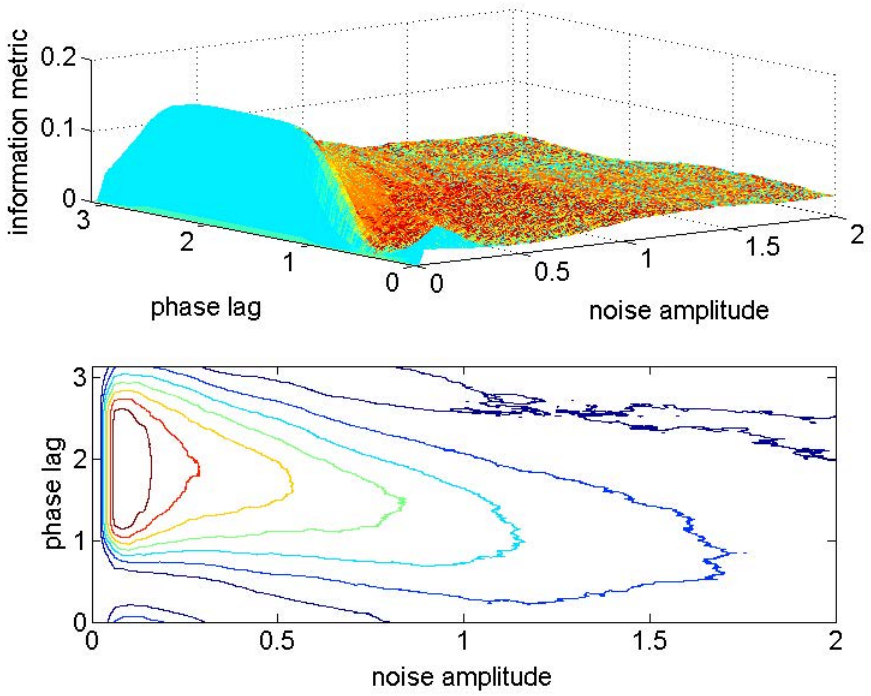

Figure 3.3: The parameters used for these simulations are as follows: $\zeta = 2, \hat{K} = 55, \hat{F} = 0.35$, and $\hat{\Omega} = 1$. The results presented in this figure, which have been obtained for a higher nonlinear stiffness value, can be compared with those shown in Figure 3.2.

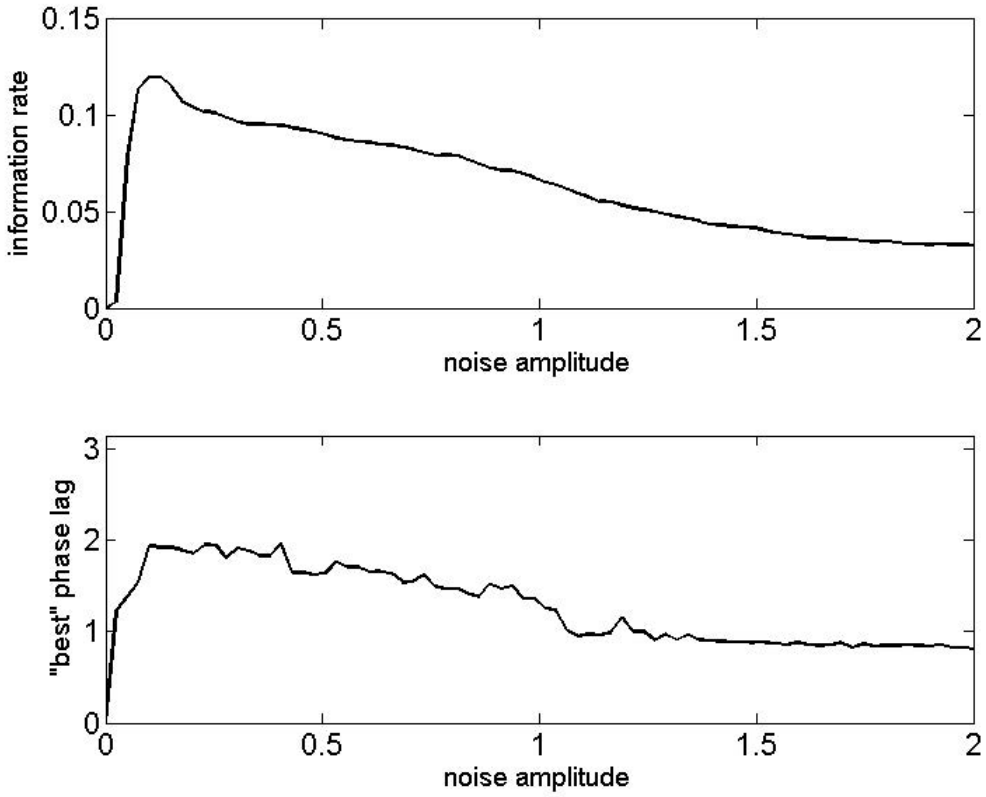

Figure 3.4: Plot of information rate versus noise amplitude. By carrying out a direct search for the largest information rate (R) values, the "best" amount of phase lag was found for each noise amplitude.

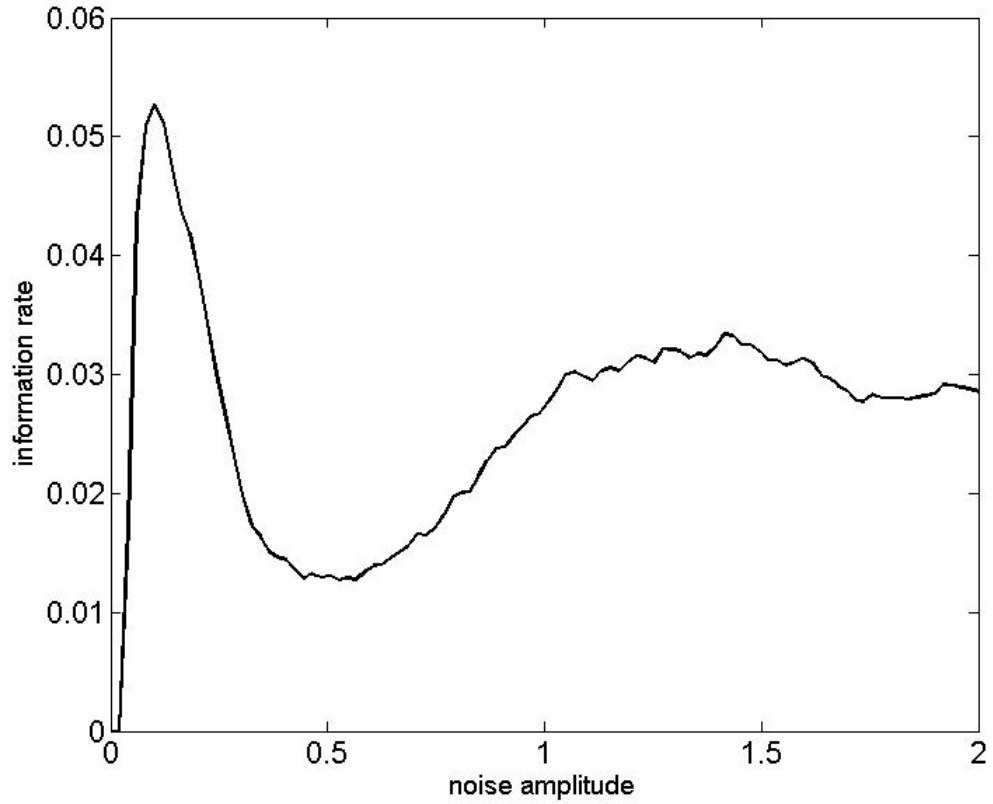

Figure 3.5: Plot of information rate versus noise amplitude for zero phase lag. Two peaks can be seen in this information rate plot. In Figures 3.2 and 3.3, a double peak feature can be observed when the phase lag is zero.

equation is the time evolution of the probability density function, which is a function of the variables in state space and time. The Fokker-Planck equation can be written as

$$\partial_t p = -\Sigma_j \partial_j [A_j(\mathbf{x}, t)p] + \tfrac{1}{2}\Sigma_{j,k}\partial_j\partial_k [B(\mathbf{x}, t)B^T(\mathbf{x}, t)]_{j,k}p \tag{3.9}$$

where $\mathbf{x}$ is the vector of variables in state space, the subscripts used with the partial signs indicate the corresponding partial derivatives, $p = p(\mathbf{x}, t)$ is the probability density function (PDF), $A_j(\mathbf{x}, t)$ is the vector containing the deterministic parts of equation (3.7), and $B(\mathbf{x}, t)$ is the vector containing the stochastic parts of equation (3.7) [Gardiner (1985)]. The Fokker-Planck equation for the bistable Duffing oscillator can then be constructed as

$$\begin{aligned}\partial_t p = -\partial_{x_1}(x_2 p) + \partial_{x_2}([2\zeta x_2 - x_1 + \hat{K}x_1^3 - \hat{F}sin(\hat{\Omega}\tau)]p) \\ + \tfrac{\hat{\sigma}^2}{2}\partial_{x_2}^2 p\end{aligned} \tag{3.10}$$

To find an approximate solution for equation (3.10), the cumulant neglect method is employed [Socha (2007)]. As also discussed in Chapter 2, the general moment equation is first written as

$$< g >= \int\int g p dx_1 dx_2 \tag{3.11}$$

Then, obtaining the moment as it evolves through time, it is found that

$$\frac{d < g >}{dt} = \int\int g\frac{dp}{dt}dx_1 dx_2 \tag{3.12}$$

Next, replacing g with the r^{th} moment of position and the s^{th} moment of velocity of the Duffing oscillator, the result is

$$\frac{d < x_1^r x_2^s >}{dt} = \int\int x_1^r x_2^s \frac{dp}{dt}dx_1 dx_2 \tag{3.13}$$

After substitution and rearrangement, the moment evolution equation for the nondimensionalized Duffing oscillator is obtained:

$$\begin{aligned}\frac{d}{dt} < x_1^r x_2^s > = r < x_1^{r-1} x_2^{s+1} > -2\zeta s < x_1^r x_2^s > \\ +s < x_1^{r+1} x_2^{s-1} > -\hat{K} s < x_1^{r+3} x_2^{s-1} > \\ +\hat{F} sin(\hat{\Omega}\tau) s < x_1^r x_2^{s-1} > \\ +\frac{\hat{\sigma}^2}{2} s(s-1) < x_1^r x_2^{s-2} >\end{aligned} \tag{3.14}$$

On substitution of different values of r and s, this moment evolution equation leads to an infinite set of ordinary differential equations (ODEs). For instance, the ODE corresponding to the time derivative of the second moment of velocity (i.e., $r = 0, s = 2$) is expressed in terms of the third moment of position. In order to truncate this infinite set of ODEs, the following approximation is made: cumulants of order 3 and higher are set equal to zero [Socha (2007)]. It should be noted that the states are not considered to be independent (i.e., $< x_1^r x_2^s > \neq < x_1^r >< x_2^s >$). From the Fokker-Planck PDE, these approximations yield the following set of five ODEs:

$$\begin{cases} \dot{\mu}_1 = \mu_2 \\ \dot{\mu}_2 = \hat{F} sin(\Omega\tau) - 2\zeta\mu_2 + \mu_1 - \hat{K}(3\mu_1\mu_3 - 2\mu_1^3) \\ \dot{\mu}_3 = 2\mu_4 \\ \dot{\mu}_4 = \mu_5 + \hat{F} sin(\Omega\tau)\mu_1 - 2\zeta\mu_4 + \mu_3 - \hat{K}(3\mu_3^2 - 2\mu_1^4) \\ \dot{\mu}_5 = \hat{\sigma}^2 + 2\hat{F} sin(\Omega\tau)\mu_2 - 4\zeta\mu_5 + 2\mu_4 - \\ \qquad 2\hat{K}(3\mu_3\mu_4 - 2\mu_1^3\mu_2) \end{cases} \tag{3.15}$$

The numerical results obtained with this reduced-order system are presented in Figure 3.6. The initial conditions used to create Figures 3.6, 3.7, 3.8,and 3.9 are $\mu_1 = \sqrt{1/\hat{K}}, \mu_2 = 0, \mu_3 = \sqrt{dt}, \mu_4 = 0$, and $\mu_5 = 0$, where dt is the step size of the Euler-Maruyama simulations. For the numerical results presented in the third section, 200 simulations were used to calculate the conditional entropy. Since the solution of the system of equations (3.15) is a time-varying probability distribution function, the probability of receiving a "1" is the area under the curve above zero,

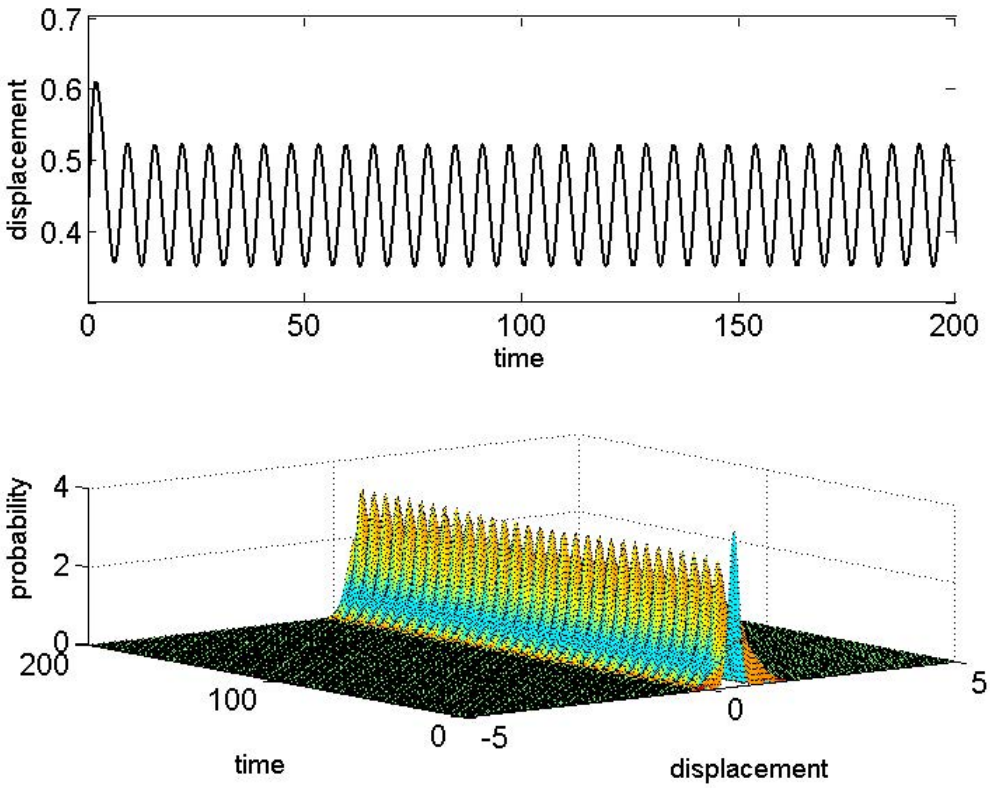

Figure 3.6: After solving the system of five ODEs obtained from the cumulant neglect method, the first five moments are used to plot the PDF of the displacement for the Duffing oscillator. The mean of the PDF plotted in the bottom plot is shown in the upper plot, as a reference.

while the probability of receiving a "0" is the area under the curve below zero. This is analogous to the procedure used for the direct numerical simulations in the previous section.

Figure 3.7 has been created by plotting the information rate against the noise amplitude and different phase lag constants. This graph, the Fokker-Planck counterpart of Figure 3.2, shows that after a certain point, the information metric quickly increases, in a range centered about approximately $\frac{\pi}{2}$ radians. After this initial sharp peak, the information metric decreases gradually. It is noted that the portion of this graph pertaining to the no phase lag case shows a double peak, similar to that seen in Figure 3.5. However, the maximum information as a function of the

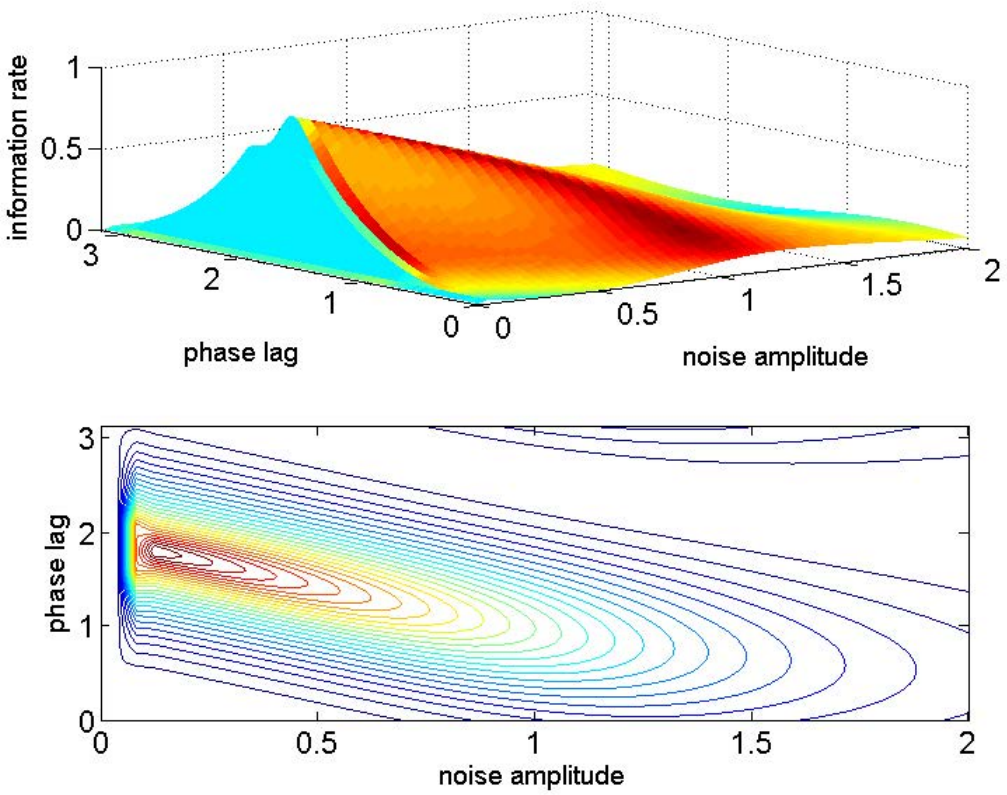

Figure 3.7: Plot of the information metric versus the noise amplitude and phase lag. The truncation of the moment evolution equations at order 3 (thus, enforcing a Gaussian aspect to the system) changes the shape of the graph. However, many qualitative similarities remain. This same information is presented as a contour plot, in order to show that the backbone of the peak decreases along the phase lag axis, as the noise amplitude is increased. The parameters used for these simulations are the same as those used for the Euler-Maruyama simulations related to Figure 3.2: $\zeta = 2, \hat{K} = 50, \hat{F} = 0.35$, and $\hat{\Omega} = 1$.

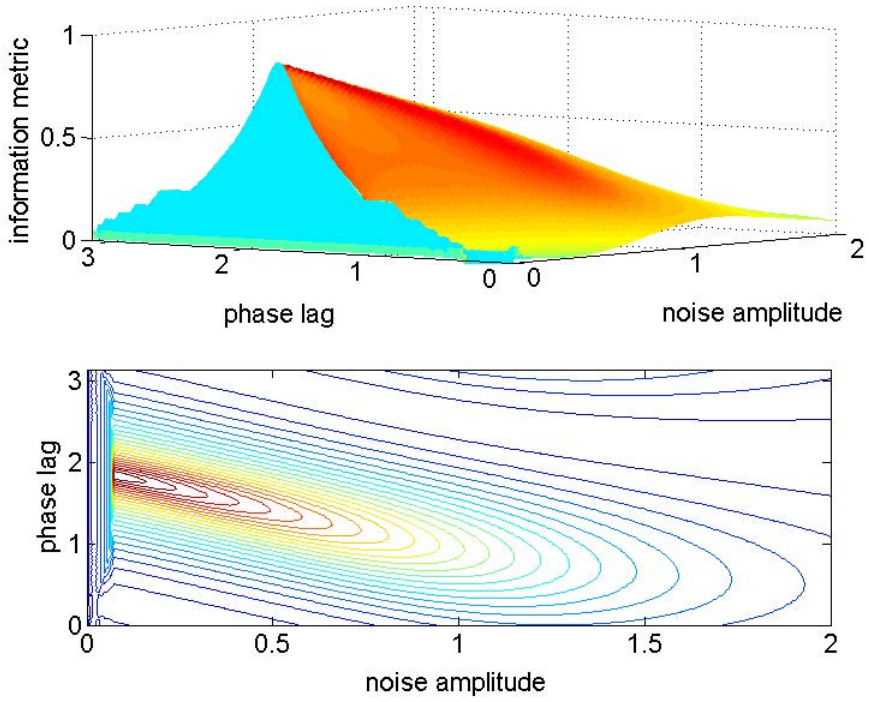

Figure 3.8: Plot of the information metric versus the noise amplitude and phase lag. The parameters used for these simulations are as follows: $\zeta = 2, \hat{K} = 55, \hat{F} = 0.35$, and $\hat{\Omega} = 1$. This graph obtained for a higher nonlinear stiffness value can be compared with Figure 3.7.

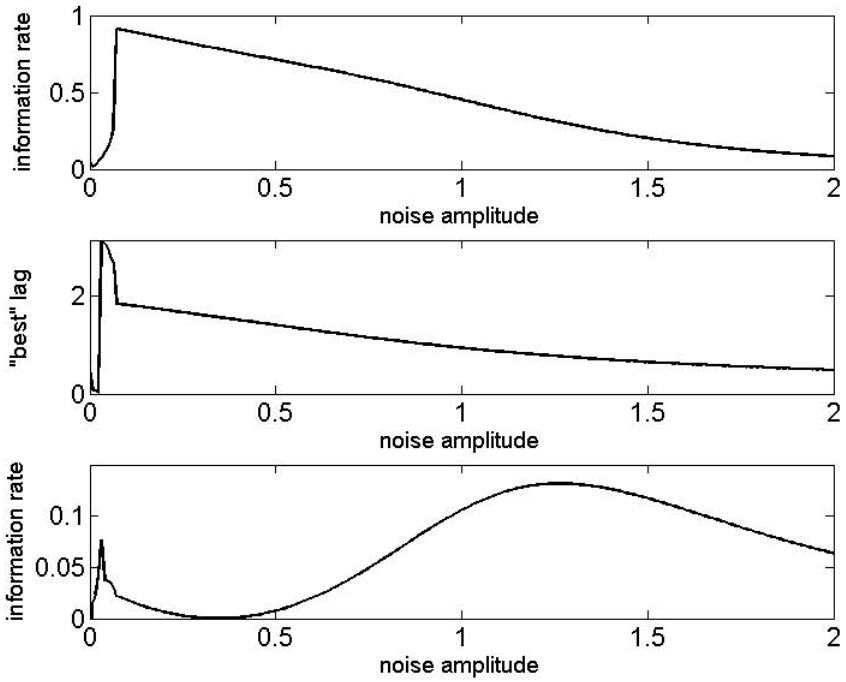

Figure 3.9: Plots to illustrate how the maximum information rate at each noise amplitude is dependent on the amount of phase lag. The bottom graph is the case of zero phase lag, which can be compared to Figure 3.5. Although the shape is different, the same qualitative double peak is observed.

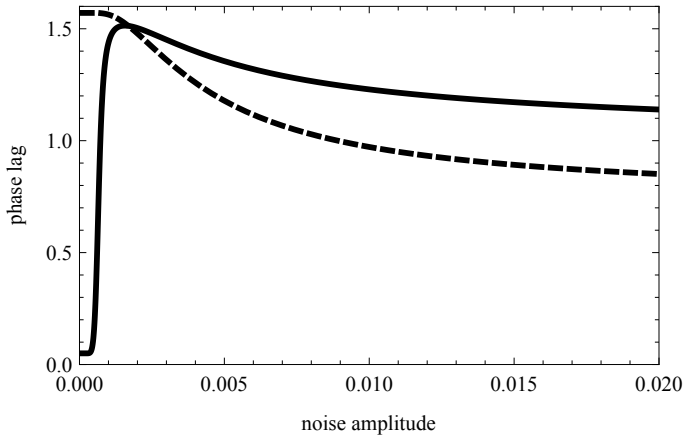

Figure 3.10: Phase lag estimated from the Kramer's rate, as obtained from equation (3.16), which is depicted by dashed lines; and from equation (3.17), which is depicted by solid lines. The parameters used are as follows: $\zeta = 2, \hat{K} = 50, \hat{F} = 0.35$, and $\hat{\Omega} = 1$.

noise level is not monotonic. The maximum information metric versus the noise amplitude is shown in Figure 3.9.

For reference, the phase lag for the SNR peak from linear response theory of a two-state system is given as

$$\bar{\phi} = arctan(\frac{\Omega}{2r_k}), \tag{3.16}$$

where the Kramer's rate $r_k = \frac{\omega_0 \omega_b}{2\pi c} e^{-\Delta V/\sigma}$, with $\omega_0^2 = V''(x_m)/m$ and $\omega_b^2 = |V''(x_b)/m|$ (V being the potential function, x_m being the minimum of the potential, and x_b being the position of the barrier) [Gammaitoni *et al.* (1998)]. For the nondimensionalized system given by equation (3.5), equation (3.16) can be used to generate the graph depicted as a dashed curve in Figure 3.10. This approach gives a monotonic phase lag for the SNR, while the phase lag results obtained from both the direct numerical simulations and Fokker-Planck formalism are not monotonic.

With further analysis of the linear response theory and taking into account intra-well motions, the phase lag can be written as

$$\bar{\phi} = arctan\Big(\frac{\frac{\Omega}{\Omega_r}(\Omega_r^2 r_k + \Omega^2 \sigma)}{\Omega_r r_k^2 + \Omega^2 \sigma}\Big), \tag{3.17}$$

where Ω_r is the relaxation rate of the system [Dykman, Mannella, McClintock, and Stocks (1992)]. This formulation for the phase lag associated with stochastic resonance does produce a peak when the phase lag is plotted against the noise amplitude, as shown by the curve plotted with solid line in Figure 3.10. Revisiting the dependence of phase lag on noise amplitude, but now plotting phase lag against noise amplitude and information rate, a more complicated relationship is noted.

3.5 Concluding Remarks

In this chapter, the focus is on how phase lag affects the use of the information rate as a metric for stochastic resonance. Through numerical simulations via the

Euler-Maruyama method and a formalism based on the Fokker-Planck equation, it has been shown that different noise amplitudes require different phase lag amounts to attain the maximal information rate at each noise amplitude. For maximizing the mutual information, it is seen that the relationship between noise amplitude and phase lag is not monotonic. Interestingly, for a phase lag of zero, a double-peak is seen in the information rate. Hence, if one is not considering phase lag, tuning the noise amplitude in order to maximize the information rate could allow for more flexibility.

The prediction from linear response theory by using the Kramer's Rate is either monotonic (equation (3.16)) or single peaked (equation (3.17)) in the plot of phase lag versus noise amplitude. When considering the system from an information theoretic approach, the peak location for the noise amplitude appears to be shifted more to the right. When studying the bistable Duffing oscillator as an information encoding medium, it is found that the phase lag is both important, and the peak is different than that predicted by linear response theory from SNR considerations.

By understanding the relationship that both the phase lag and noise amplitude have with the information rate, better tuning techniques can be developed to maximize the amount of information sent through a noisy channel. If the delaying effects of sending the signal through a noisy channel are known *a priori*, this could be used to glean more information.

Chapter 4

NOISE-INFLUENCED TRANSIENT ENERGY LOCALIZATION IN AN OSCILLATOR ARRAY

The effects of noise on transient energy localization in a coupled array of nonlinear oscillators are examined. Results obtained through simulations of deterministic systems are compared to those obtained through Euler-Maruyama scheme based simulations of the corresponding stochastic systems. To complement the numerical studies as in previous chapters, a Fokker-Planck formalism is also used to analyze the response of the system in the presence of noise. Transient localization phenomena are explored by using time-domain and time-frequency analysis, and the insights gained are discussed. The intent of this study is to further the understanding of related behavior and use it for the benefit of a nonlinear system.

Through the current study, it is shown that noise suppresses a traveling wave by transferring energy to low-frequency components. In the next section, a brief literature review is given which discusses some aspects of energy localizations. In Section 4.2, the nonlinear oscillator array is described. Euler-Maruyama simulations and wavelet analysis are shown in Section 4.3. In Section 4.4, the Fokker-Planck equation is simulated in order to study the system. In the discussion section, concluding remarks, as well as observations pertinent to a system of coupled bistable Duffing oscillators, are made. This system is seen to exhibit noise-induced transitions, which the author plans to further study in the future.

4.1 Introduction and Background

Energy localizations, which can result as a consequence of intrinsic localized modes in micro-resonator arrays [Dick *et al.* (2008)], can lead to damage due to undesirable response levels. On the other hand, these localizations can also be beneficial, with applications in energy harvesting, sensing, and other applications (e.g., [Dick, Balachandran, Yabuno, Numatsu, Hayashi, Kuroda, and Ashida (2009b); Chakraborty and Balachandran (2011)]). In the study [Benzi *et al.* (1981)], Benzi described the mechanism through which a combination of stochastic effects and deterministic forcing may enhance the system response at a particular frequency. The enhanced performance was shown to be absent when either the stochastic input or the deterministic forcing is separately applied. In the author's recent studies [Perkins and Balachandran (2012)], an energy localization was provoked by the addition of noise to an array of nonlinear oscillators under specific conditions. Though the effects of noise have been examined for nonlinear oscillator arrays subjected to harmonic inputs [Lindner, Bennett, and Wiesenfeld (2006); Jung, Behn, Pantazelou, and Moss (1992); Ramakrishnan and Balachandran (2010)], effects of noise on transient energy localizations could be of importance as well.

In this chapter, the author primarily studies the system of nonlinearly coupled monostable oscillators illustrated in Figure 4.1. This system is excited from one end with a sinc pulse, which is depicted in Figure 4.2. The sinc pulse is defined as

$$sinc(t) = \begin{cases} \frac{sin(2\pi f_1(t-t_0))}{2\pi f_1(t-t_0)}, & t \neq t_0 \\ 1, & t = t_0 \end{cases} \tag{4.1}$$

This excitation method has been utilized to take advantage of the localized pulse-like behavior of the sinc function while proving a "soft start" to the system. The additional frequency content in the sinc function is an adequate tradeoff for the "soft start" property.

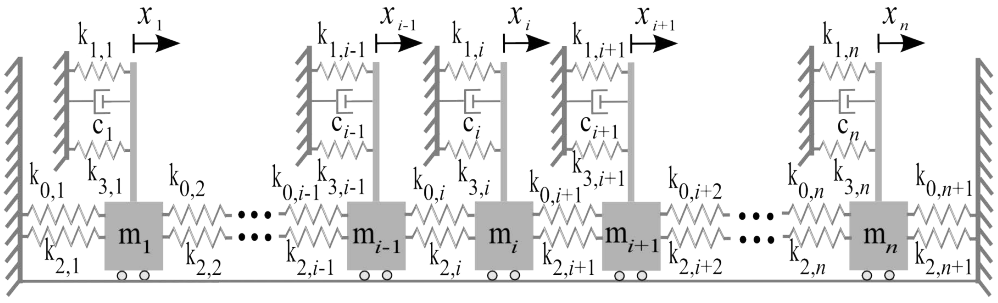

Figure 4.1: An array of nonlinear coupled oscillators. Each mass is coupled to adjacent masses by linear and nonlinear springs. In addition, each mass is attached to a local restraint through a combination of linear springs, nonlinear springs, and linear dampers. The parameters used in the subsequent simulations (except for Figure 4.12) are as follows: $m_{odd} = 1.00, m_{even} = 0.80, c_i = 0.01, k_{0,i} = 45.00, k_{1,i} = 1, k_{2,i} = 50.00, and k_{3,i} = 0.00$.

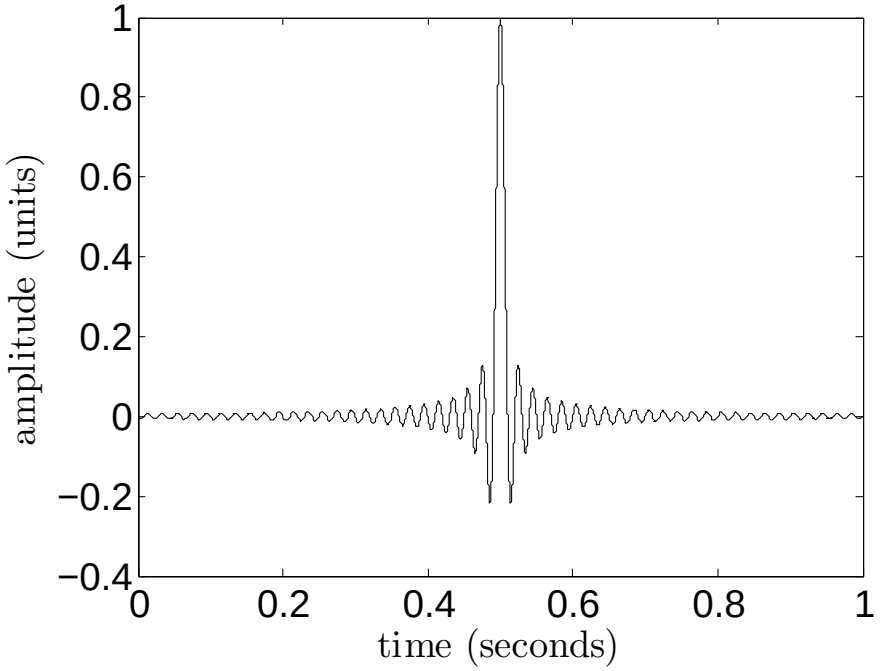

Figure 4.2: The sinc pulse which lasts for one second has energy content spread over a broad range of frequencies.

The Euler-Maruyama algorithm [Higham (2001)] is used to numerically simulate the considered systems, and along with it, the Fokker-Planck equation [Gardiner (1985)] is used to develop the moment evolution equations and study them. The moment evolution equations are derived by utilizing the method of moments [Socha

(2007)]. Morlet wavelet analysis [Chabalko *et al.* (2005)] is used to measure the effects of the noise and characterize the system response in the time-frequency domain.

4.2 Nonlinear Oscillator Array

The equations of motion for the considered oscillator array, which is shown in Figure 4.1, can be written in the form

$$\begin{cases} m_1\ddot{x}_1 + c_1\dot{x}_1 + (k_{0,1} + k_{0,2} + k_{1,1})\, x_1 - k_{0,2}x_2 + k_{2,1}x_1^3 + k_{3,1}x_1^3 + \\ k_{3,2}\,(x_1 - x_2)^3 = Fsinc(t) + \sigma\dot{W}(t) \\ \vdots \\ m_i\ddot{x}_i + c_i\dot{x}_i - k_{0,i}x_{i-1} + (k_{0,i} + k_{0,i+1} + k_{1,i})\, x_i - k_{0,i+1}x_{i+1} + k_{2,i}x_i^3 + k_{3,i}\,(x_i - x_{i-1})^3 + \\ k_{3,i+1}\,(x_i - x_{i+1})^3 = \sigma\dot{W}(t) \\ \vdots \\ m_n\ddot{x}_n + c_n\dot{x}_n - k_{0,n}x_{n-1} + (k_{0,n} + k_{0,n+1} + k_{1,n})\, x_n - k_{2,n}x_n^3 + \\ k_{3,n}\,(x_n - x_{n-1})^3 = \sigma\dot{W}(t) \end{cases} \tag{4.2}$$

where the constants are defined in Table 4.1. The boundary oscillators are coupled to adjacent oscillators on one side and fixed restraints on the other side. The internal oscillators are coupled to adjacent oscillators and also attached to local restraints through spring-damper combinations.

By appropriately choosing the $k_{2,i}$ and $k_{3,i}$ terms, the system becomes an array of monostable oscillators or an array of bistable Duffing oscillators. The Fokker-Planck equation for the i^{th} oscillator of this system can be written as follows:

$$\begin{aligned} \partial_t p = -\Bigg(\partial_{x_{i,1}} x_{i,2} p + \tfrac{1}{m_i}\partial_{x_{i,2}} p \Big(& - c_i x_{i,2} + k_{0,1}x_{i-1,1} - (k_{0,i} + k_{0,i+1} + k_{1,i})\, x_{i,1} + k_{0,i+1}x_{i+1,1} \\ & - (k_{2,i} + k_{2,i+1} + k_{3,i})\, x_{i,1}^3 + (3k_{2,i}x_{i-1,1} + 3k_{2,i+1}x_{i+1,1})\, x_{i,1}^2 - \left(3k_{2,i}x_{i-1,1}^2 + 3k_{2,i+1}x_{i+1,1}^2\right) x_{i,1} \\ & + \left(k_{2,i}x_{i-1,1}^3 + k_{2,i+1}x_{i+1,1}^3\right) \; + \delta_{1,i}Fsinc(t) \Big) \Bigg) + \tfrac{\sigma^2}{2m_i^2}\tfrac{\partial^2}{\partial(x_{i,2})^2} p \end{aligned} \tag{4.3}$$

Table 4.1: Nomenclature describing the quantities governing the array of oscillators.

x_i	position of i^{th} oscillator
$x_{i,1}$	position of i^{th} oscillator in state space
$x_{i,2}$	velocity of i^{th} oscillator in state space
m_i	mass of i^{th} oscillator
$k_{0,i}$	linear coupling spring on left side of i^{th} oscillator
$k_{1,i}$	linear spring constant of i^{th} oscillator
$k_{2,i}$	nonlinear coupling spring on left side of i^{th} oscillator
$k_{3,i}$	nonlinear spring constant of i^{th} oscillator
c_i	damping coefficient of i^{th} oscillator
F	forcing amplitude
$\dot{W}(t)$	white noise (derivative of Wiener process)
σ	noise amplitude
$sinc$	sinc pulse which lasts for one second

Further details of this construction and analysis of the Fokker-Plank equation is included in Section 4.4.

4.3 Euler-Maruyama Simulations

In order to numerically simulate the system of monostable oscillators, the governing equations need to be put in an appropriate form. First, to realize the system of monostable oscillators, the $k_{2,i}$ terms are set equal to a positive number, and the $k_{3,i}$ terms are set equal to zero. The oscillators are initialized at their equilibrium position and the first oscillator is excited by a delayed sinc function. In state-space form, the equations of motion are given by

$$
\begin{cases}
\dot{x}_{1,1} = x_{1,2} \\
\dot{x}_{1,2} = \Big(- c_1 x_{1,2} - \left(k_{0,1} + k_{0,2} + k_{1,1}\right) x_{1,1} + k_{0,2} x_{2,1} - \\
k_{3,1} x_{1,1}^3 - k_{3,2} \left(x_{1,1} - x_{2,1}\right)^3 + F sinc(t) + \sigma \dot{W}(t) \Big) / m_1 \\
\vdots \\
\dot{x}_{i,1} = x_{i,2} \\
\dot{x}_{i,2} = \Big(- c_i x_{i,2} + k_{0,i} x_{i-1,1} - \left(k_{0,i} + k_{0,i+1} + k_{1,i}\right) x_{i,1} + k_{0,i+1} x_{i+1,1} - \\
k_{3,i} \left(x_{i,1}^3 - x_{i-1,1}\right)^3 - k_{3,i+1} \left(x_{i,1} - x_{i+1,1}\right)^3 + \sigma \dot{W}(t) \Big) / m_i \\
\vdots \\
\dot{x}_{n,1} = x_{n,2} \\
\dot{x}_{n,2} = \Big(- c_n x_{n,2} + k_{0,n} x_{n-1,1} - \left(k_{0,n} + k_{0,n+1} + k_{1,n}\right) x_{n,1} - \\
k_{3,n} \left(x_{n,1} - x_{n-1,1}\right)^3 - k_{3,n+1} x_{n,1}^3 + \sigma \dot{W}(t) \Big) / m_n
\end{cases}
\tag{4.4}
$$

This system of Langevin equations can then be converted to differential form suitable for numerical simulations as

$$
\begin{cases}
dx_{1,1} = x_{1,2}dt \\
dx_{1,2} = \Big[\Big(- c_1 x_{1,2} - \left(k_{0,1} + k_{0,2} + k_{1,1}\right) x_{1,1} + k_{0,2} x_{2,1} - \\
k_{3,1} x_{1,1}^3 - k_{3,2} \left(x_{1,1} - x_{2,1}\right)^3 + Fsinc(t)\Big) dt + \sigma dW\Big] / m_1 \\
\vdots \\
dx_{i,1} = x_{i,2}dt \\
dx_{i,2} = \Big[\Big(- c_i x_{i,2} + k_{0,i} x_{i-1,1} - \left(k_{0,i} + k_{0,i+1} + k_{1,i}\right) x_{i,1} + k_{0,i+1} x_{i+1,1} - \\
k_{3,i} \left(x_{i,1}^3 - x_{i-1,1}\right)^3 - k_{3,i+1} \left(x_{i,1} - x_{i+1,1}\right]^3 \Big) dt + \sigma dW\Big] / m_i \\
\vdots \\
dx_{n,1} = x_{n,2}dt \\
dx_{n,2} = \Big[\Big(- c_n x_{n,2} + k_{0,n} x_{n-1,1} - \left(k_{0,n} + k_{0,n+1} + k_{1,n}\right) x_{n,1} - \\
k_{3,n} \left(x_{n,1} - x_{n-1,1}\right)^3 - k_{3,n+1} x_{n,1}^3 \Big) dt + \sigma dW\Big] / m_n
\end{cases}
\tag{4.5}
$$

With this system of equations in differential form, the Euler-Maruyama method is used to simulate the system. As mentioned previously in this dissertation, this is an extension of Euler's method for ordinary differential equations (ODEs) to an implementation for stochastic differential equations (SDEs). Representative results obtained from a simulation are shown in Figure 4.3. The time evolutions of the displacement responses of all 16 oscillators are shown in the upper portion of the figure by using a color scale for the displacement range. The oscillators begin at their equilibrium positions, denoted by green color. An excitation wave is applied to the first oscillator, and the wave can be seen traveling through the array of oscillators. Since the array is nonlinear, the wave motion cannot be described just by a wave speed. The wave defines a boundary of influence where an oscillator does not experience the excitation until the wave has reached it. A second wave, slightly

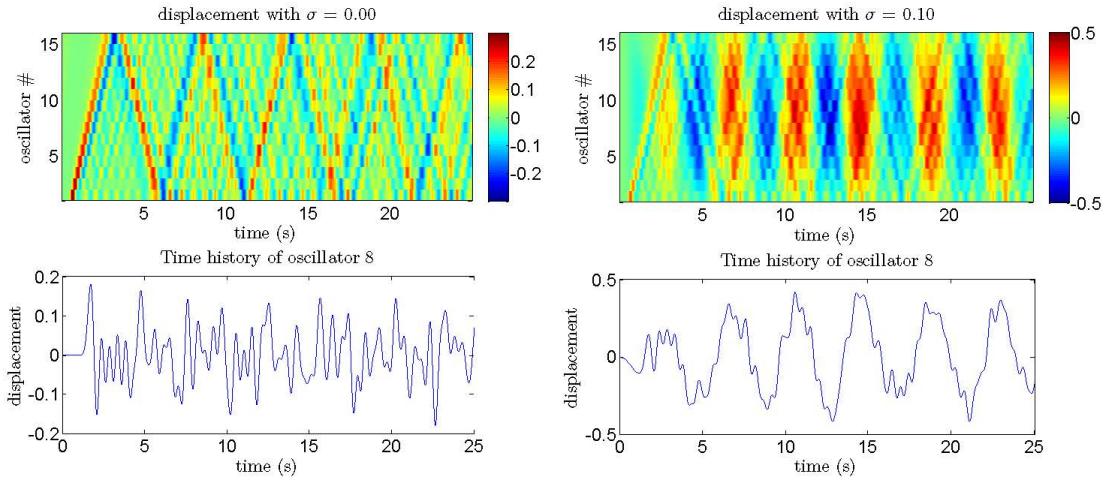

Figure 4.3: Time evolutions of the displacement responses for a system of 16 nonlinearly coupled monostable oscillators is shown in the upper portion of the figure. Displacement amplitude is expressed by using a color scale. In the lower portion of the figure, the time history of the displacement response of oscillator 8 is shown. For the results of the left column $\sigma = 0.00$, and for those in the right column $\sigma = 0.10$. In each panel, a traveling wave can be identified traversing the system.

delayed, of negative displacement follows the first wave. The waves reflect off the boundary at oscillator 16, and continue through the system. The individual nodes continue to oscillate after the wave has passed through them. The wave disperses as it reflects and travels through the system. An individual time history of oscillator 8 is shown in the lower portion of Figure 4.3. The oscillator can be identified to be in a zero energy state, until the oscillator encounters the wave. The crest of the wave can be identified at a time close to 2 seconds. The oscillator continues to ring; the reflected wave passes and revisits it, just after 5 seconds.

4.3.1 Continuous Wavelet Transform

The continuous wavelet transform allows simultaneous signal characterization in time and frequency domains. The wavelet coefficients are computed by convolving the input signal with a so-called mother wavelet as described in reference [Teolis (1998)] and shown below, wherein the asterisk denotes the complex conjugate of the

corresponding quantity.

$$W(a,\tau) = \int_{-\infty}^{\infty} f(t)\Psi^*(a, t-\tau)dt \tag{4.6}$$

The mother wavelet $\Psi(a,t)$ is chosen to have properties which match features of the signal being analyzed. The Morlet wavelet has been chosen since it matches well to signals with sinusoidal oscillations. The wavelet is defined as a complex sinusoid shaped by a Gaussian window as shown below.

$$\Psi(a,t) = \frac{1}{\sqrt{a}} e^{i\omega_\Psi t/a} e^{-(t/a)^2/2} \tag{4.7}$$

The center frequency of the wavelet is adjustable through ω_Ψ, which was taken to be 5.5 as described in reference [Chabalko *et al.* (2005)]. The real part, imaginary part, and magnitude of the mother wavelet are shown in Figure 4.4. The author notes the complex sinusoidal behavior of the real and imaginary parts. The magnitude of the wavelet can be identified by the Gaussian window. Here, the magnitude of the wavelet coefficient $|W(a,\tau)|$ is used to characterize oscillations in time and frequency. These coefficients provide a measure of transient matching of the wavelet to the signal. The magnitude of the coefficients is large when the scaled (a), and shifted (τ) wavelet matches the signal, and the coefficients are small otherwise. The scaling parameter a can be related to a harmonic frequency f by utilizing the Δt of the signal being analyzed through the relation $f = \frac{\omega_\Psi}{2\pi\Delta t a}$. As the scale a decreases, the frequency equivalent of the wavelet increases and vice-versa.

A validation example of a wavelet matching a transient harmonic signal is shown in Figure 4.5. In this case, the first two pulses are transient 30 Hz sinusoids, and the second two pulses are transient 55 Hz sinusoids. The magnitudes of the wavelet coefficients, plotted in the lower portion of Figure 4.5, reveal the time and frequency localization of each pulse.

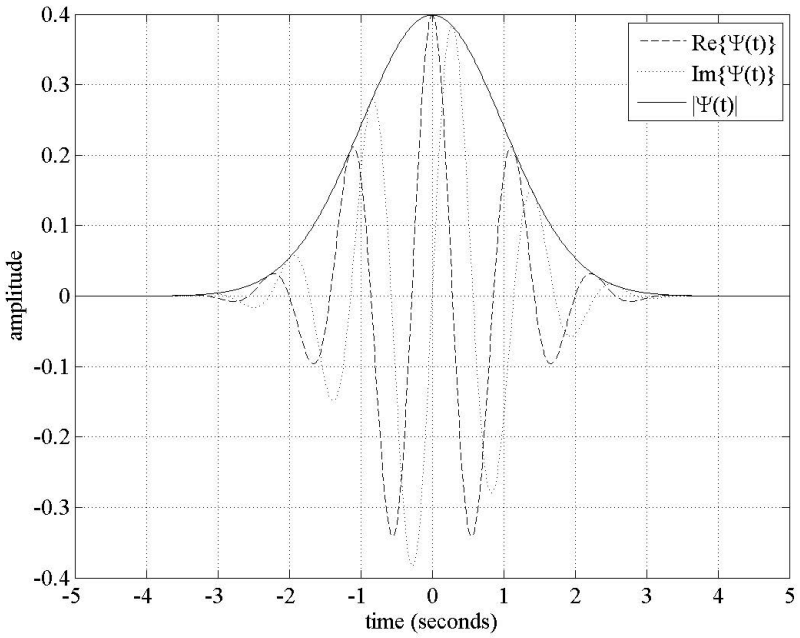

Figure 4.4: Real part, imaginary part, and magnitude of the mother Morlet wavelet. The wavelet can be used to describe signals with sinusoidal components, and it allows for identification of transient frequency content.

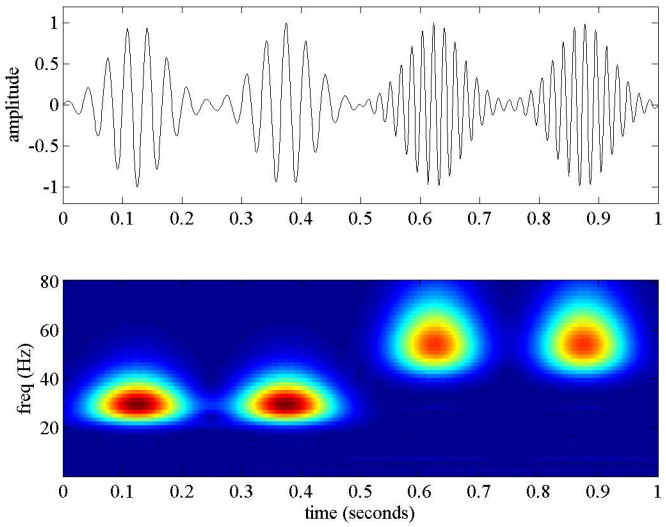

Figure 4.5: A time series with transient frequency content, along with the magnitudes of the wavelet coefficients shown below. The blue color is used to denote the lowest value and the red color is used to denote the highest value. The Morlet wavelet is able to characterize the transient signal in time and frequency space.

4.3.2 Analyses of Euler-Maruyama Simulation Results

The system of monostable oscillators, excited by a sinc pulse, was subjected to two different levels of noise. In the first case, no noise was included in the input signal; this case can be considered as a control case. The wave traversed the system of oscillators several times. The magnitudes of the wavelet coefficients for oscillators $1, 8$ and 16 of this case ($\sigma = 0.00$) are shown in the top row of Figure 4.6. The wave can be identified as a transient fluctuation just above 1 Hz in each of the oscillator responses. Oscillator 8 is less responsive to the wave, although this may be due to the phase of the wave as it traverses oscillator 8. The results obtained for the next case, for which $\sigma = 0.10$, are shown in the second row of Figure 4.6. In this case, the magnitudes of the wavelet coefficients show increased energy at lower frequencies. The response in the 1 Hz range of oscillator 8 is significantly reduced, as compared to that observed in the previous case. The response at oscillator 16 in the 1 Hz range is reduced as well. For all three oscillators, low frequency $(0.00 - 0.20)$ Hz energy can be identified in the responses, as shown in the lower portion of each plot. These frequency ranges can be compared to the lowest and highest linear natural frequencies for this array, which have been computed to be 0.27 Hz and 2.26 Hz, respectively.

This effect can be examined in more detail by analyzing the difference in the magnitudes of the wavelet coefficients between the control case and the case with $\sigma = 0.10$, as shown in Figure 4.7. To this end, the time integral of the amplitude of the wavelet coefficients was computed over all oscillators. Subtracting out the control case from the $\sigma = 0.10$ case, the difference in the amplitudes of each case is seen only as a function of frequency:

$$G = \Sigma_{oscillator} \int_{time} (|W_{\sigma=.1}| - |W_{\sigma=0}|)dt \tag{4.8}$$

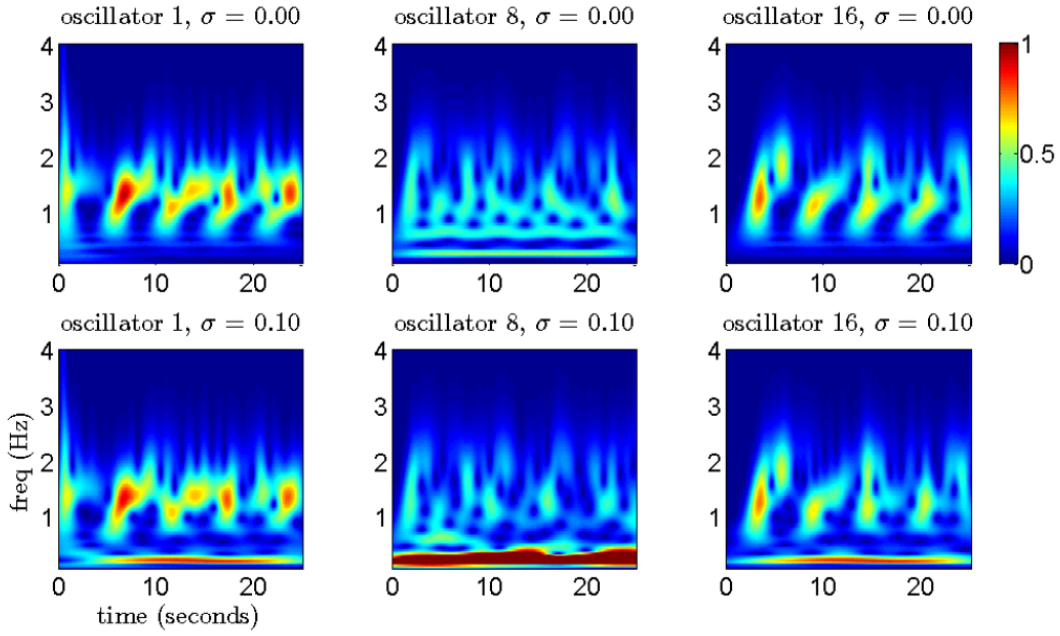

Figure 4.6: Amplitudes of the coefficients of the Morlet wavelets of the first, 8^{th}, and last oscillators show that noise attenuates the traveling wave, while increasing the amplitudes of low frequency components.

This allows the attenuation across the $1.00 - 2.00$ Hz band to be characterized, without any ambiguities from phase shifting. It is noted that a large amount of energy appears in the low-frequency range. The attenuations in the $1.00 - 2.00$ Hz range due to the noise can be clearly identified through the negative values. It appears that noise attenuates energy from the higher natural frequencies, while increasing energy near the first natural frequency.

4.4 Fokker-Planck Formalism

As previously mentioned, the Fokker-Planck equation is a partial differential equation whose solution is the time evolution of the probability density function. This probability density function is a function of all of the variables in state space and time. The general form can be written as follows [Gardiner (1985)]

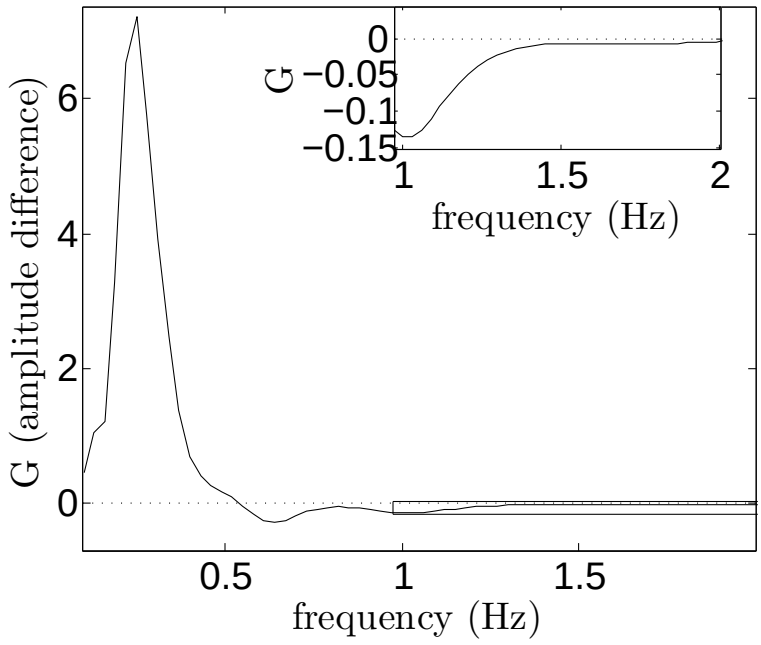

Figure 4.7: Time integral of the amplitude of the wavelet coefficients over all oscillators. An expanded view of the marked region is shown in the insert.

$$\partial_t p = -\Sigma_j \partial_j [A_j(\mathbf{x}, t)p] + \tfrac{1}{2}\Sigma_{j,k}\partial_j\partial_k [B(\mathbf{x}, t)B^T(\mathbf{x}, t)]_{j,k}p \tag{4.9}$$

The complete Fokker-Planck equation for this coupled oscillator system would require $2n + 1$ variables (i.e. one for each position, one for each velocity, and one for time). For brevity, the Fokker-Planck equation is written only for the i^{th} oscillator. By inserting the equations for the i^{th} oscillator in equation 4.5 into equation 4.9, equation 4.3 is found. The method of moments is used to find the moment evolution equation for this system, which is an infinite set of ODEs. As before, first consider the general moment equation, where $p = p(x_1, x_2, t)$ is the probability density function at time t:

$$\langle z \rangle = \iint z p dx_1 dx_2 \tag{4.10}$$

Then, obtaining the moment as it evolves through time, it is found that

$$\frac{d\langle z\rangle}{dt} = \iint z\frac{dp}{dt}dx_1dx_2 \tag{4.11}$$

Now, considering the r^{th} moment of position and s^{th} moment of velocity of the i^{th} oscillator, the result is

$$\frac{d\langle x^r v^s\rangle}{dt} = \iint x^r v^s\frac{dp}{dt}dx_1dx_2 \tag{4.12}$$

After substitution and rearrangement, the moment evolution equation for the i^{th} oscillator is obtained as

$$\begin{aligned}\tfrac{d}{dt}\langle x_i^r v_i^s\rangle = r\left\langle x_i^{r-1}v_i^{s+1}\right\rangle + \tfrac{s}{m_i}\Bigg[\Bigg(c_i\left(\langle v_{i-1}\rangle + \langle v_{i+1}\rangle\right) + k_{0,i}\langle x_{i-1}\rangle + k_{0,i+1}\langle x_{i+1}\rangle + \\ \left[k_{3,i}\langle x_{i-1}\rangle^3 + k_{3,i+1}\langle x_{i+1}\rangle^3\right] + \delta_{1,i}Fsinc(t)\Bigg)\left\langle x_i^r v_i^{s-1}\right\rangle \\ -2c_i\langle x_i^r v_i^s\rangle - \left[k_{0,1}+k_{0,i+1}+k_{1,i}\right]\left\langle x_i^{r+1}v_i^{s-1}\right\rangle - \\ \left[k_{3,i}+k_{3,i+1}\right]\left\langle x_i^{r+3}v_i^{s-1}\right\rangle + 3\left[k_{3,i}\langle x_{i-1}\rangle + k_{3,i+1}\langle x_{i+1}\rangle\right]\left\langle x_i^{r+2}v_i^{s-1}\right\rangle \\ +3\left[k_{3,i}\langle x_{i-1}\rangle^2 + k_{3,i+1}\langle x_{i+1}\rangle^2\right]\left\langle x_i^{r+1}v_i^{s-1}\right\rangle\Bigg] + \tfrac{\sigma^2}{2m_i^2}s\left(s-1\right)\left\langle x_i^r v_i^{s-2}\right\rangle\end{aligned} \tag{4.13}$$

From this moment evolution equation, one obtains an infinite set of ODEs parameterized by r and s. In order to solve this infinite set of ODEs, the following three approximations are made: i) the Fokker-Planck equation for the i^{th} oscillator can be written considering only the neighboring two oscillators, ii) the states of the i^{th} oscillator can be considered independent from the states of the neighboring oscillators (for instance, $< x_i^r v_i^s x_{i+1}^u >=< x_i^r v_i^s >< x_{i+1}^u >$), and iii) moments of order 7 and higher are set equal to zero (which truncates the infinite set of ODEs). These approximations yield a set of $27n$ ODEs, from the previous SDEs. This reduced-order system has been numerically solved and the obtained time histories

of the displacement responses of all the oscillators are presented in Figure 4.8.The oscillator motions are started at their equilibrium positions and the initial wave can be identified propagating through the array. After reaching oscillator 16, the wave reflects and continues propagating through the array. The results are similar to those obtained through the Euler-Maruyama simulations for $\sigma = 0.00$ and shown in Figure 4.3.

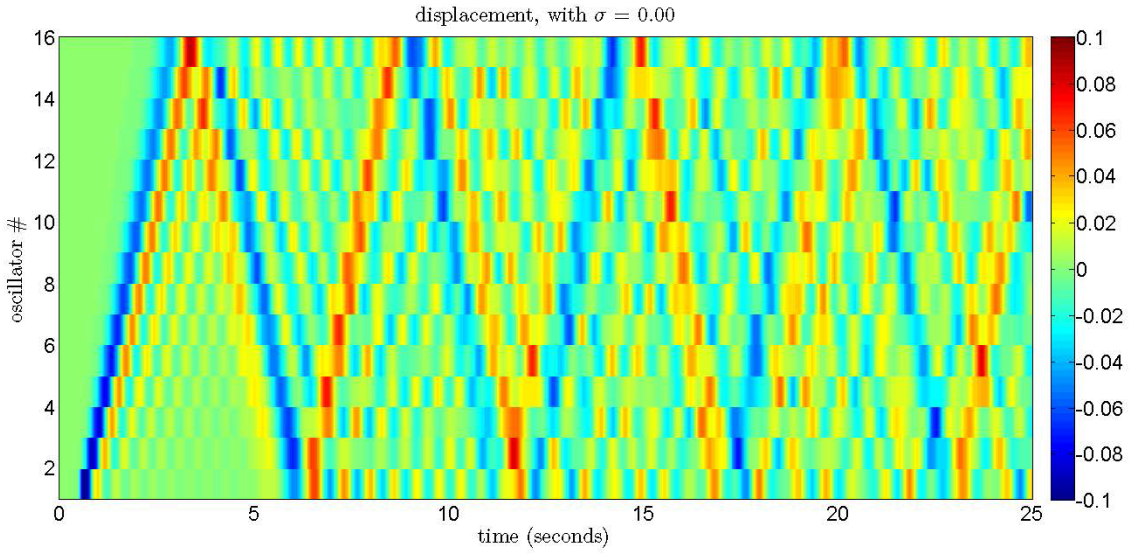

Figure 4.8: Time histories of the responses for the array of oscillators with no noise, obtained by using moment evolution equations.

The first six moments were computed from the method of moments. It is found that the 5^{th} and 6^{th} moments had near zero values, while the other moments had non-zero values. The probability distribution function of oscillator displacement can be modeled after the Pearson distribution (e.g., [Andreev *et al.* (2005)]). This distribution can be determined from the first four central moments μ_1, μ_2, μ_3, and μ_4, as obtained by solving the differential equation

$$p'(x) = p(x)\frac{(x-\mu_1)-a}{b_0 + b_1(x-\mu_1) + b_2(x-\mu_1)^2} \tag{4.14}$$

where

$$
\begin{aligned}
a = b_1 &= \frac{-\mu_3\left(\mu_4 + 3\mu_2^2\right)}{A} \\
b_0 &= \frac{-\mu_2\left(4\mu_2\mu_4 - \mu_3^2\right)}{A} \\
b_2 &= \frac{-\left(2\mu_2\mu_4 - 3\mu_3^2 - 6\mu_2^3\right)}{A} \\
A &= 10\mu_2\mu_4 - 18\mu_2^3 - 12\mu_3^2
\end{aligned}
\tag{4.15}
$$

Based on the above formulation, the Pearson distributions associated with the response of oscillator 8 has been determined for two different noise levels. The probability density function for the displacement response of oscillator 8 as a function of time in the absence of noise is shown in the left portion of Figure 4.9. Initially, the probability distribution for the displacement response of the oscillator is very narrow, because of the small variance of the distribution. As time progresses, the position of the oscillator may admit some uncertainty; however, the large central peak of the probability distribution is indicative of the high likelihood of the displacement position of the oscillator. The position of the oscillator is less certain when noise is added to the system, as indicated by the results shown in the right portion of Figure 4.9. In this case, the initial position of the oscillator has small variance as before. However, as time progresses, the probability distribution of the position of the oscillator becomes more diffuse. This characteristic diffusion effect can be seen for many Fokker-Planck systems. The presence of noise causes the second, third, and fourth moments to increase in time.

Similar to the wavelet analyses conducted in Section 4.3, wavelets calculated from the Fokker-Planck formalism are presented in Figure 4.10, with the associated analysis presented in Figure 4.11. Qualitatively similar attenuation of the traveling wave can be seen from the wavelet analyses performed on the Euler-Maruyama simulation results and that performed on the results from the Fokker-Planck formalism.

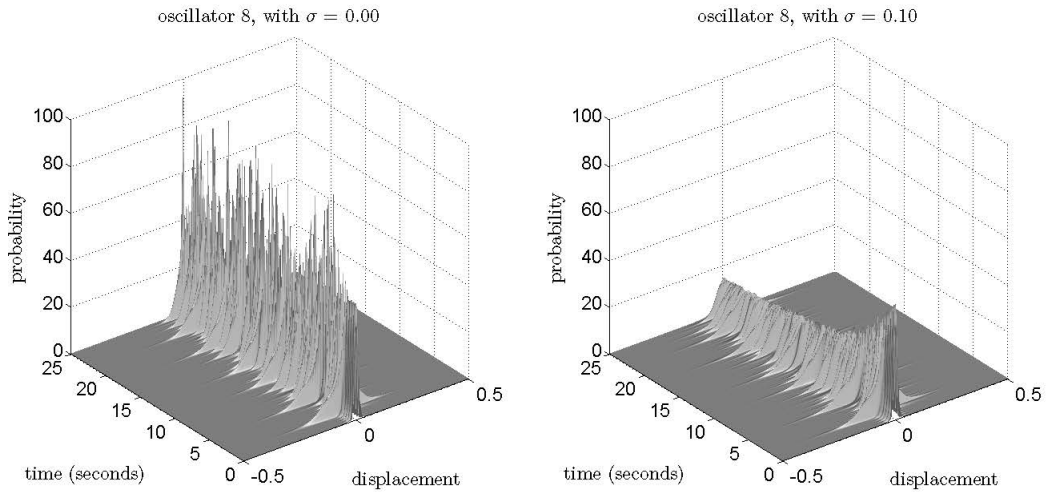

Figure 4.9: Probability density variation for displacement response of oscillator 8 with respect to time. The displacement can be characterized by a Pearson distribution. In the case of no noise, the displacement is highly localized (left). In the case of noise ($\sigma = 0.10$), the displacement is less certain as shown by the large amount of diffusion in the distribution as time evolves (right). The first moment (the mean value) for the control case in Figure 4.9 may be directly compared to the response history of oscillator 8 in Figure 4.3.

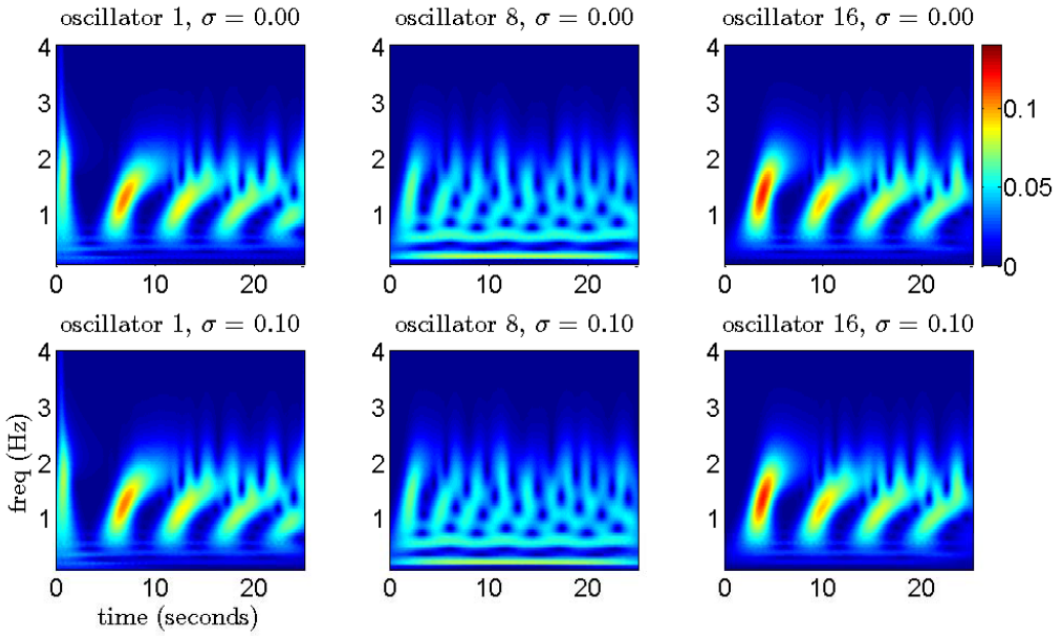

Figure 4.10: Wavelets calculated from the first moment obtained from the method of moments analysis. The traveling wave is slightly attenuated, which is similar to the results obtained from the Euler-Maruyama simulations.

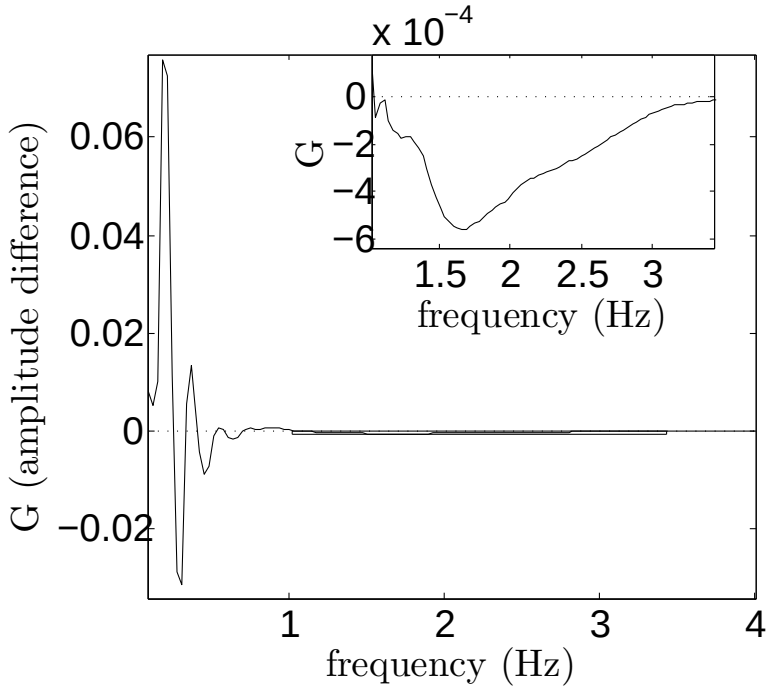

Figure 4.11: The difference in the integrals of the amplitudes of the wavelet coefficients is shown, in the same manner as presented in Figure 4.7. The scaling is smaller than that seen with the Euler-Maruyama simulations, although the qualitative attenuation in the $1.00 - 2.00$ Hz range and the low frequency amplification is still discernible. The author plans to further study the response behavior in the $0.25 - 1.00$ Hz range, as this is notably different from that seen in Figure 4.7.

4.5 Concluding Remarks

A system of nonlinearly coupled monostable Duffing oscillators has been studied in this effort. The variation of response with respect to noise level was considered, including the control case of no noise. The system was numerically simulated with the Euler-Maruyama method and analytically cast to a reduced-order model of ODEs by using the method of moments. Solutions from both methods yielded qualitatively similar behavior. In each case, an initial wave was shown to be attenuated with the addition of Gaussian white noise. In the cases studied, energy at low frequencies was identified. Time-frequency analyses was carried out by employing the Morlet wavelet and used to characterize the system response and identify transient energy

attenuation.

The probability distribution for the position of an oscillator was characterized by using the Pearson distribution. This distribution showed the mean position response of the oscillator as a function of time. When noise was present, the spread of the distribution was observed to increase significantly as time progressed. These results could be useful to develop shielding for systems which are robust to small noise levels, but for which wave impulses could be detrimental. The apparent energy transfer from noise into low frequency bands could also be exploited for energy harvesting. This work is part of an ongoing effort, as a part of which, macroscopic experimental systems of oscillators are being studied.

In a related study, an additional phenomenon was also found by the author. For a system of linearly coupled bistable Duffing oscillators (i.e., $k_1 < 0$, $k_2 = 0$, $k_3 > 0$), a wave-like, switching phenomenon could be produced with the addition of noise. The oscillators are initialized in their left stable equilibrium position, and the first oscillator is excited with a sinc pulse during the first second, as before. The pulse is seen to have little effect on the other oscillators, as it travels through the array, as shown in Figure 4.12. By adding Gaussian white noise, a switching, wave-like propagation is observed, where oscillators settle into their right stable equilibrium positions. This noise-induced switching phenomenon, which is akin to the stochastic resonance phenomenon, is to be further studied by the author and this phenomenon may be relevant to the dynamics of neuron chains.

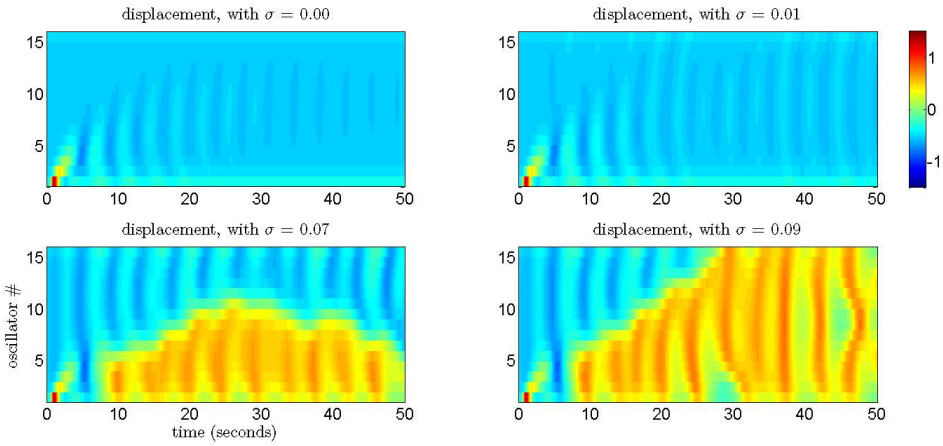

Figure 4.12: The sinc pulse alone does not cause all of the oscillators to switch from their left well to their right well. By using noise (applied to all oscillators), the switching, wave-like phenomenon is seen to progress through the entire array. For a moderate amount of noise, the switching behavior can only go through a portion of the array. A higher noise level induces all oscillators to switch wells. The parameters used in this simulation are as follows: $m_i = 1.00, c_i = 0.60, k_{0,i} = 1.50, k_{1,i} = -1.50, k_{2,i} = 0.00, and k_{3,i} = 5.00$.

Chapter 5

NOISE-ENHANCED RESPONSE OF NONLINEAR OSCILLATOR ARRAY

In this chapter, a set of coupled monostable Duffing oscillators will be studied. Noise-enhancement possibilities in the context of an array of monostable Duffing oscillators are explored. For the coupled oscillators, it is shown that an appropriately chosen noise addition can be used to localize energy as well as shift energy localization locations.

The rest of this chapter is organized as follows. In the next section, a brief literature review of intrinsic localized modes is presented. In Section 5.2, the equations governing the array of coupled monostable Duffing oscillators are derived. The Euler-Maruyama simulations and the Method of Moments analysis are both presented in this section and discussed along with the results obtained. Concluding remarks are collected together in Section 5.3.

5.1 Introduction and Background

In the literature, intrinsic localized modes (ILMs) are known as discrete breathers or Anderson localizations; they are energy localizations that can occur in spatially extended, perfectly periodic, discrete systems [Anderson (1958); Campbell, Flach, and Kivshar (2004)]. ILMs occurring in pure anharmonic lattices are similar to energy localizations occurring in harmonic lattices with a defect [Sievers and Takeno (1988)]. They can be considered to be a forced nonlinear vibration mode of an oscillatory system [Dick, Balachandran, and Mote (2008)]. Here, an array of monostable Duffing oscillators is studied, as it has relevance to microelectrome-

Table 5.1: Nomenclature describing the quantities governing the array of oscillators.

x_i	Displacement of i^{th} oscillator
$x_{i,1}$	Displacement of i^{th} oscillator in state space
$x_{i,2}$	Velocity of i^{th} oscillator in state space
m_i	Mass of i^{th} oscillator
$k_{0,i}$	Linear coupling spring on left side of i^{th} oscillator
$k_{1,i}$	Linear spring constant of i^{th} oscillator
$k_{3,i}$	Nonlinear spring constant of i^{th} oscillator
K_i	$k_{0,i} + k_{0,i+1} + k_{1,i}$
c_i	Viscous damping term of i^{th}
F	Forcing amplitude
Ω	Forcing frequency
$\dot{W}(t)$	White Gaussian noise (derivative of Wiener process)
σ	Noise amplitude

chanical systems (MEMS), which are relevant for a host of engineering applications including communications and signal processing. However, the oscillator array structure considered here is different from previous studies carried out in the author's group [Dick *et al.* (2008)]. At the micro-scale, stochastic effects can play a significant role in determining the system dynamics and ILMs have been studied in the context of micro-scale systems [Dick *et al.* (2008); Sato *et al.* (2003a)]. ILMs can have adverse effects on the performance of a micromechanical device; for example, they could inhibit information flow or, in some cases, damage the microelectromechanical array and the associated electronic circuitry. However, if these energy localizations are better understood, they have the potential to lead to new technologies. The energy localization phenomenon in the coupled oscillator array of this study does not have the large amplitude characteristic of an ILM; however, this work is relevant to realize energy localization in coupled oscillator arrays.

With each of the systems considered, the deterministic system will first be studied, and then a stochastic noise component will be included in the input. In both cases, the system is numerically studied by using the Euler-Maruyama method [Higham (2001)]. By using this method, one obtains an approximate solution of the system. This method is an extension of the Euler method for ordinary differential

equations, which has been adapted to perform integrations of stochastic differential equations (SDEs). In addition, a Method of Moments analysis is also used to study the averaged dynamics of the system. Through this analysis, the author obtains an approximation to the Fokker-Planck equation (a partial differential equation) for the system, which governs the evolution of the probability density function of the states of each oscillator in the array. The moment evolution equations (an infinite set of ordinary differential equations) are derived and truncated from the Fokker-Planck equation. Numerically solving this truncated, finite set of ordinary differential equations gives an averaged (approximate) solution to the variables in the state space.

5.2 Monostable Duffing oscillator array

Consider the array of monostable Duffing oscillators, which is depicted in Figure 5.1 and described by the following equations, with the variable and parameter descriptions, following that provided in Section 5.1:

$$\begin{cases} \begin{gathered} m_1\ddot{x}_1 + c_1\dot{x}_1 + (k_{0,1} + k_{0,2} + k_{1,1})\, x_1 - k_{0,2}x_2 + k_{3,1}x_1^3 \\ = Fsin(\Omega t) + \sigma\dot{W}(t) \end{gathered} \\ \vdots \\ \begin{gathered} m_i\ddot{x}_i + c_i\dot{x}_i - k_{0,i}x_{i-1} + (k_{0,i} + k_{0,i+1} + k_{1,i})\, x_i - k_{0,i+1}x_{i+1} + k_{3,i}x_i^3 \\ = Fsin(\Omega t) + \sigma\dot{W}(t) \end{gathered} \\ \vdots \\ \begin{gathered} m_n\ddot{x}_n + c_n\dot{x}_n - k_{0,n}x_{n-1} + (k_{0,n} + k_{0,n+1} + k_{1,n})\, x_n + k_{3,n}x_n^3 \\ = Fsin(\Omega t) + \sigma\dot{W}(t) \end{gathered} \end{cases} \tag{5.1}$$

5.2.1 Euler-Maruyama simulations

In system (5.1), these n oscillators all have the same deterministic and stochastic forcing ($Fsin(\Omega t)$ and $\sigma\dot{W}(t)$, respectively). The term, $\dot{W}(t)$, denotes white noise,

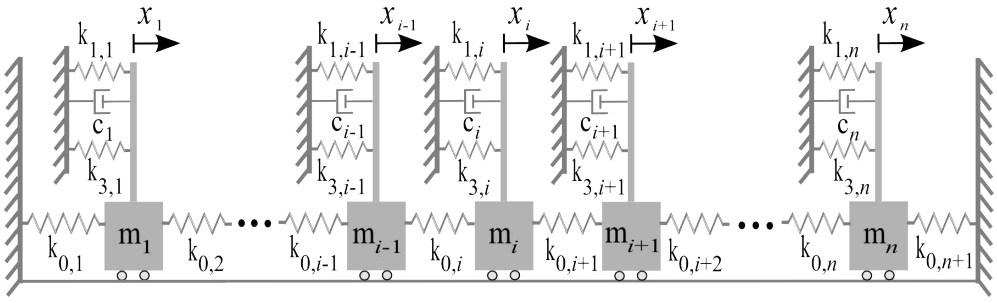

Figure 5.1: Array of n coupled monostable Duffing oscillators.

which is defined as the derivative of Brownian motion. Since Brownian motion (or in the physics literature, the Wiener process) has independent increments as previously, its derivative does not exist with probability one [Chorin and Hald (2009)]. Thus, $\dot{W}(t)$ is a "mnemonic" derivative. To write the equations with more formality, this system of stochastic differential equations are converted into Langevin form. For facilitating the analysis, the equations of motion are first cast into a state-space form. In the subsequent notation, the xs first subscript refers to the oscillator and the second subscript is used to denote the corresponding state:

$$
\begin{cases}
\dot{x}_{1,1} = x_{1,2} \\
\dot{x}_{1,2} = \Big(- c_1 x_{1,2} - (k_{0,1} + k_{0,2} + k_{1,1})\, x_{1,1} + k_{0,2} x_{2,1} \\
\qquad -k_{3,1} x_{1,1}^3 + F sin(\Omega t) + \sigma \dot{W}(t) \Big) / m_1 \\
\vdots \\
\dot{x}_{i,1} = x_{i,2} \\
\dot{x}_{i,2} = \Big(- c_i x_{i,2} + k_{0,i} x_{i-1,1} - (k_{0,i} + k_{0,i+1} + k_{1,i})\, x_{i,1} + k_{0,i+1} x_{i+1,1} \\
\qquad -k_{3,i} x_{i,1}^3 + F sin(\Omega t) + \sigma \dot{W}(t) \Big) / m_i \\
\vdots \\
\dot{x}_{n,1} = x_{n,2} \\
\dot{x}_{n,2} = \Big(- c_n x_{n,2} + k_{0,n} x_{n-1,1} - (k_{0,n} + k_{0,n+1} + k_{1,n})\, x_{n,1} \\
\qquad -k_{3,n+1} x_{n,1}^3 + F sin(\Omega t) + \sigma \dot{W}(t) \Big) / m_n
\end{cases}
\tag{5.2}
$$

Next, in differential form, this system of Langevin equations is written as

$$
\begin{cases}
dx_{1,1} = x_{1,2}dt \\
dx_{1,2} = \Big[\Big(- c_1 x_{1,2} - \left(k_{0,1} + k_{0,2} + k_{1,1}\right) x_{1,1} + k_{0,2} x_{2,1} \\
\qquad -k_{3,1} x_{1,1}^3 + F sin(\Omega t)\Big) dt + \sigma dW\Big] / m_1 \\
\vdots \\
dx_{i,1} = x_{i,2}dt \\
dx_{i,2} = \Big[\Big(- c_i x_{i,2} + k_{0,i} x_{i-1,1} - \left(k_{0,i} + k_{0,i+1} + k_{1,i}\right) x_{i,1} + k_{0,i+1} x_{i+1,1} \\
\qquad -k_{3,i} x_{i,1}^3 + F sin(\Omega t)\Big) dt + \sigma dW\Big] / m_i \\
\vdots \\
dx_{n,1} = x_{n,2}dt \\
dx_{n,2} = \Big[\Big(- c_n x_{n,2} + k_{0,n} x_{n-1,1} - \left(k_{0,n} + k_{0,n+1} + k_{1,n}\right) x_{n,1} \\
\qquad -k_{3,n} x_{n,1}^3 + F sin(\Omega t)\Big) dt + \sigma dW\Big] / m_n
\end{cases}
\tag{5.3}
$$

Notice that in this differential form, one no longer has the derivative of Brownian motion (which does not exist) but a differential white noise which does exist. Now, the Euler-Maruyama method can be used to obtain numerical solutions of the following system:

$$
\begin{cases}
x_{1,1}(j+1) = x_{1,1}(j) + x_{1,2}(j)dt \\
x_{1,2}(j+1) = x_{1,1}(j) + \Big[\Big(- c_1 x_{1,2}(j) - (k_{0,1} + k_{0,2} + k_{1,1})\, x_{1,1}(j) + k_{0,2} x_{2,1}(j) \\
\qquad -k_{3,1} x_{1,1}^3(j) + F sin(\Omega t)\Big) dt + \sigma \delta W_j \Big] / m_i \\
\vdots \\
x_{i,1}(j+1) = x_{i,1}(j) + x_{i,2}(j)dt \\
x_{i,2}(j+1) = x_{i,1}(j) + \Big[\Big(- c_i x_{i,2}(j) + k_{0,i} x_{i-1,1}(j) - (k_{0,i} + k_{0,i+1} + k_{1,i})\, x_{i,1}(j) \\
\qquad +k_{0,i+1} x_{i+1,1}(j) - k_{3,i} x_{i,1}^3(j) + F sin(\Omega t)\Big) dt + \sigma \delta W_j \Big] / m_i \\
\vdots \\
x_{n,1}(j+1) = x_{n,1}(j) + x_{n,2}(j)dt \\
x_{n,2}(j+1) = x_{n,1}(j) + \Big[\Big(- c_n x_{n,2}(j) + k_{0,n} x_{n-1,1}(j) - (k_{0,n} + k_{0,n+1} + k_{1,n})\, x_{n,1}(j) \\
\qquad -k_{3,n} x_{n,1}^3(j) + F sin(\Omega t)\Big) dt + \sigma \delta W_j \Big] / m_i
\end{cases}
\tag{5.4}
$$

In this form, j is associated with the time step in the solver. The quantity, δW_j, is the incremental noise; it has mean equal to zero and standard deviation equal to $\sqrt{dt}$. In these simulations, the forcing frequency was ramped up, starting at the highest linear natural frequency and progressing to a value 0.5% higher than the highest linear natural frequency for the system of oscillators, in a manner similar to that carried out in the group's previous studies [Dick *et al.* (2008); Ramakrishnan and Balachandran (2010)]. Thirty-two oscillators were simulated, while varying the noise intensity as a system parameter.

In Figure 5.2a), the forcing frequency profile is provided. The frequency is ramped from the highest natural frequency to 0.5% above the highest natural frequency over two seconds. After this time, the frequency is held constant until 40 seconds is reached, where the forcing is turned off completely. In Figure 5.2b),

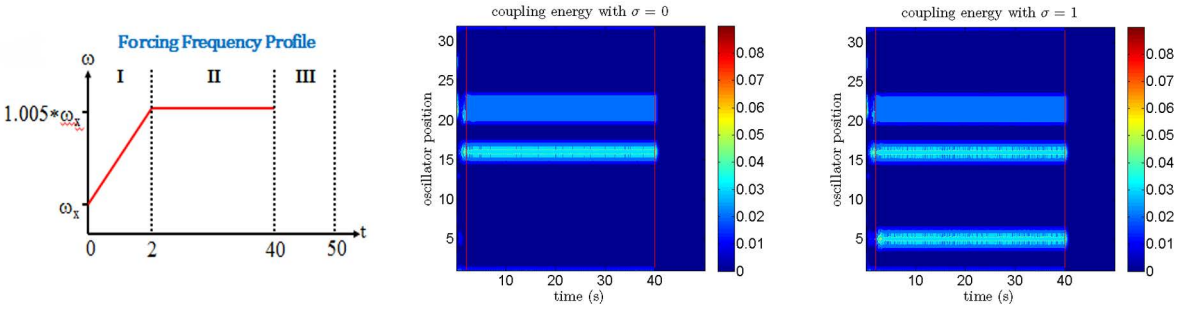

Figure 5.2: a) The forcing frequency profile. b) Without noise, two energy localizations form. c) With noise, three energy localizations form.

two energy localizations are shown. In Figure 5.2(c), with the addition of noise, an additional energy localization forms. In Figure 5.2, one of the localizations is more spatially distributed than the other: the localization at oscillators 15-16 has denser energy than the localization at oscillators 20-23. Further research is necessary in order to determine whether the noise has a deterministic effect on where an ILM forms. This is an important question if noise can be used to control the formation of ILMs at different locations in a micro-oscillator array. The present results can be compared to those previously obtained by Ramakrishnan and Balachandran [Ramakrishnan and Balachandran (2010)], for micro-cantilever arrays, in which each oscillator pair had two different types of oscillators. Although the oscillator systems of references [Dick *et al.* (2008); Ramakrishnan and Balachandran (2010)] are different from the current one, the author believes that noise can produce the following two differing effects in array systems; that is, attenuation of energy localizations and creation of energy localizations. If fully understood, noise might be harnessed to create and/or destroy energy localizations in an array. These phenomena will be further discussed in Chapter 7.

5.2.2 Fokker-Planck equation and Method of Moments analysis

In the preceding subsection, the use of noise to realize energy localization through a direct numerical simulation was demonstrated. In this subsection, the aim

is to obtain an approximate solution on the basis of a formalism based on the Fokker-Planck equation [Gardiner (1985)]. The solution of this partial differential equation is the time evolution of the probability density function, which is a function of the variables in state space and of time. As previously mentioned, the Fokker-Planck equation can be written as

$$\partial_t p = -\Sigma_j \partial_j [A_j(\mathbf{x},t)p] + \tfrac{1}{2}\Sigma_{j,k}\partial_j\partial_k [B(\mathbf{x},t)B^T(\mathbf{x},t)]_{j,k}p \tag{5.5}$$

where p is the probability density function and $\mathbf{x}$ is the vector of variables in state space. The Fokker-Planck equation for the i^{th} oscillator can be constructed as

$$\begin{array}{c}\partial_t p = -[\partial_{x_{i,1}} x_{i,2}p + \frac{1}{m_i}\partial x_{i,2}p(-c_i x_{i,2} + k_{0,i}x_{i-1,1} - [k_{0,i}+k_{0,i+1}+k_{1,i}]x_{i,1} \\ +k_{0,i+1}x_{i+1,1} - k_{3,i}x_{i,1}^3 + Fsin(\Omega t))] + D\frac{\partial^2}{\partial^2_{xi,2}}p\end{array} \tag{5.6}$$

To find an approximate solution for this equation, the Method of Moments is employed [Sobczyk (2001)], in a manner similar to previous chapters.

After substitution and rearrangement, the moment evolution equation for the i^{th} oscillator is obtained as

$$\begin{array}{c}\frac{d}{dt} < x^r v^s >= r < x^{r-1} >< v^{s+1} > -\frac{sc}{m} < x^r >< v^s > \\ +\frac{sk_{0,i}}{m} < x^r >< v^{s-1} >< x_{i-1} > -\frac{sK_i}{m} < x^{r+1} >< v^{s-1} > \\ +\frac{sk_{0,i}}{m} < x^r >< v^{s-1} >< x_{i+1} > -\frac{sk_{3,i}}{m} < x^{r+3} >< v^{s-1} > \\ +\frac{sFsin(\Omega t)}{m} < x^r >< v^{s-1} > +s(s-1)D < x^r >< v^s >\end{array} \tag{5.7}$$

The x's and v's without subscripts refer to the position and velocity of the i^{th} oscillator, and $K(i) = k_0(i) + k_0(i+1) + k_1(i)$. This moment evolution equation gives an infinite set of ODEs, as different values of r and s are substituted. The following three approximations are made, in order to solve this infinite set of ODEs: 1) the Fokker-Planck equation is written for the i^{th} oscillator, considering only the neighboring two oscillators, 2) the states are assumed to be independent (i.e.,

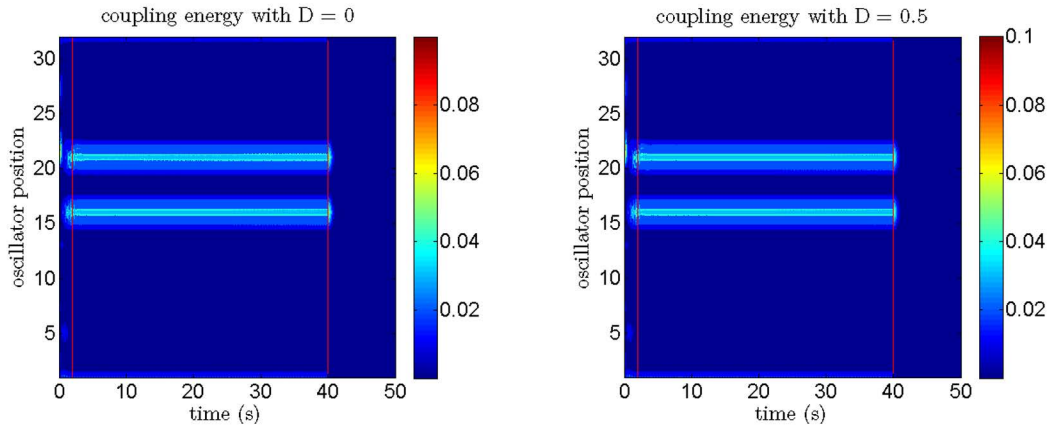

Figure 5.3: The numerical solution to the Fokker-Planck equation, using the same parameters as in Figure 5.1. a) For no noise, two energy localizations form. b) Using the same noise level as in Figure 5.1(b), there are still only two localizations.

$< x^r v^s >=< x^r >< v^s >$), and 3) moments of order 4 and higher are neglected. These approximations yield a set of $6n$ ODEs, from the previous SDE. The numerical results obtained with this reduced-order system are presented in Figure 5.3.

Note that in using the Fokker-Planck equation, it is customary to use $\sigma = \sqrt{2D}$; thus, this is indeed the same noise level as that used to generate the results shown in Figure 5.1. Also, the same initial conditions were used to generate the results shown in Figure 5.2 as well as that shown in Figure 5.3. It seems that on average, the third energy localization does not occur. However, through the previous Euler-Maruyama simulations, the localization is shown to occur sometimes. By taking higher order moments, the third energy localization observed in Figure 5.2c) might be better predicted by the Method of Moments analysis.

5.3 Concluding remarks

The present work is intended to be an exploration into coupled oscillator systems, to illustrate the influence of noise on the response of nonlinear oscillators. In one of the considered cases, preliminary efforts were undertaken to understand the effects of noise on the response of a homogeneous array of monostable Duffing

oscillators. The Euler-Maruyama method was employed to simulate this stochastic system. For the coupled oscillator array, the Fokker-Planck equation was derived for a representative oscillator. Assumptions regarding independence of moments and a truncation approximation were made in order to find a numerical approximation for the solution of the Fokker-Planck equation. The results suggest that a white noise addition can create an energy localization in the array, but in an average sense, this usually does not happen. In other studies in the author's group, with a different set of coupled oscillators, it was shown that noise can be used to attenuate an energy localization [Ramakrishnan and Balachandran (2010)]. Between the present and previous studies, it is shown that noise can be used to facilitate as well as to suppress energy localizations in coupled oscillator array systems. However, a fuller presentation of this effect with respect to the hysteresis curve will be explored in Chapter 7.

Chapter 6

INFLUENCE OF CUBIC COUPLING NONLINEARITIES ON RESPONSE LOCALIZATION

In this chapter, the response localization in coupled arrays of nonlinear oscillators with cubic coupling nonlinearities is studied. For illustration, an array of micro-scale oscillators with intersite or coupling nonlinearities is considered and attention is focused on intrinsic localized modes. Free oscillations and forced oscillations of this system are considered, and the interplay between noise and cubic coupling nonlinearities is studied through numerical studies. These studies help elucidate the role of coupling nonlinearities on energy localization in micro-scale oscillators.

The rest of this chapter has been structured as follows. In Section 6.1, a brief literature review of pertinent intrinsic localized mode research is presented. In Section 6.2, a micro-cantilever array model is presented along with a special case of a homogeneous oscillator array, which forms the basis for the work presented in the sections that follow. Next, in Section 6.3, numerical studies are conducted with the undamped and unforced system to understand the formation of intrinsic localized modes by examining the restricted normal modes of the system. Following that, in Section 6.4, numerical studies are conducted to examine the influence of noise on the system behavior. Different strengths of noise intensities are considered and the influence of the coupling nonlinearities on the system response is examined. Finally, based on the findings, conclusions are drawn and presented in the last section.

6.1 Introduction and Background

Localization of responses in oscillator arrays has been of interest for a number of years (e.g. [Sievers and Takeno (1988); Sato, Hubbard, and Sievers (2006)]), with particular attention devoted to the roles of nonlinearity and discreteness. Discrete breathers (DBs) or intrinsic localized modes (ILMs), which are spatially localized and time-periodic solutions of the considered system, constitute one example of localization phenomenon. This phenomenon has been often been described as a natural paradigm for response localization in several systems. Experimental evidence for these energy localizations has also been produced in different physical systems, including photonic lattices [Fleischer, Segev, Efremidis, and Christodoulides (2003)], Josephson junction arrays [Ustinov (2003)], micro-scale cantilever arrays [Sato *et al.* (2003b); Dick *et al.* (2008)], and macro-scale cantilever arrays [Kimura and Hikihara (2009)]. Extensive analytical and numerical studies have also been conducted to understand the occurrence of intrinsic localized modes [Sato, Hubbard, and Sievers (2006); Dick, Balachandran, and Mote (2008, 2009a); Kimura and Hikihara (2009); Kimura, Matsushita, and Hikihara (2013)]. There have also been some recent studies where the focus has been on the influence of noise on such localization. These studies include cases with onsite cubic nonlinearities [Cubero, Cuevas, and Kevrekidis (2009)] and both onsite and intersite cubic nonlinearities [Ramakrishnan and Balachandran (2010, 2011)]. Symmetric response distributions about a primary center oscillator location were considered in these studies. Apart from energy localization, a variety of other nonlinear phenomena are also exhibited by micro-scale and nano-scale oscillators [Rhoads, Shaw, and Turner (2010)].

In the group's prior efforts, in an array of micro-scale oscillators with linear (intersite) coupling and onsite cubic nonlinearity in each oscillator, it has been shown that ILMs can be interpreted as nonlinear vibration modes [Dick *et al.* (2008)] and that the fundamental frequency relationships between the adjacent oscillators

in an oscillator array can have an influence on the energy localization. Following these early efforts, in [Ramakrishnan and Balachandran (2010)], it was shown that white noise addition to a deterministic input can be used to strengthen as well as attenuate localizations. In a related study, Ramakrishnan and Balachandran [Ramakrishnan and Balachandran (2011)] examined the case where cubic coupling or intersite nonlinearities were present. The present work can be considered as an extension of these prior efforts. Here, a cantilever array of homogeneous oscillators is considered with cubic onsite nonlinearities in each oscillator and linear intersite coupling and cubic intersite coupling are considered. Dissipation is also considered. Numerical studies are considered to understand the influence of the cubic coupling nonlinearities and frequency relationships that could lead to internal resonances in the system. The influence of noise on the localization behavior is also investigated. In the free-oscillation case, it is shown that the intersite nonlinearities can help in tailoring the response localization. In the cases with noise, where some of the first results of its kind are reported, it is shown that the presence of cubic coupling nonlinearities can help in attenuating intrinsic localized modes.

6.2 Micro-cantilever array to homogeneous oscillator array

Following the work of Sato *et al.* [Sato *et al.* (2006)], for an oscillator cell i, the cell dynamics is governed by the equations

$$m_a\ddot{x}_{a,i} + \frac{m_a}{\tau}\dot{x}_{a,i} + k_{2a}x_{a,i} + k_{4a}x_{a,i}^3 + k_I\left(2x_{a,i} - x_{b,i} - x_{b,i-1}\right) + k_{4I}\left[\left(x_{a,i} - x_{b,i}\right)^3 + \left(x_{a,i} - x_{b,i-1}\right)^3\right] = m_a\alpha \quad (6.1)$$

$$m_b\ddot{x}_{b,i} + \frac{m_b}{\tau}\dot{x}_{b,i} + k_{2b}x_{b,i} + k_{4b}x_{b,i}^3 + k_I\left(2x_{b,i} - x_{a,i+1} - x_{a,i}\right) + k_{4I}\left[\left(x_{b,i} - x_{a,i}\right)^3 + \left(x_{b,i} - x_{a,i+1}\right)^3\right] = m_b\alpha \quad (6.2)$$

In Equations (6.1) and (6.2), the subscripts a and b correspond to the different cantilever lengths, m_a and m_b are their respective masses, τ is a time constant, k_{2a} and k_{2b} are the associated linear spring stiffness constants, k_{4a} and k_{4b} are the associated cubic spring stiffness constants, and k_I is the linear stiffness coupling constant. The entire array is subjected to a uniform forcing through acceleration α that can be achieved by distributed base actuation. It is important to note that this actuation, which can be realized through piezoelectric actuators, does not directly apply a force to the cantilevers but rather causes an acceleration of the cantilever array's base [Sato *et al.* (2006); Dick *et al.* (2008)].

Considering a special case of a homogeneous oscillator array; that is, an array with similar cantilevers for example, and setting $m_a = m_b = m$, $k_{2a} = k_{2b} = k$, and $k_{4a} = k_{4b} = k_3$ and dividing throughout by m, the system given by Equations (6.1) and (6.2) is rewritten as

$$\ddot{x}_i + \frac{1}{\tau}\dot{x}_i + \alpha_1 x_i + \beta_1 x_i^3 + \alpha_2\left(2x_i - x_{i+1} - x_{i-1}\right) + \beta_2\left[\left(x_i - x_{i+1}\right)^3 + \left(x_i - x_{i-1}\right)^3\right] = F\cos(\Omega t) + \sigma\dot{W}(t) \quad (6.3)$$

where

$$\alpha_1 = \frac{k}{m}; \qquad \alpha_2 = \frac{k_I}{m}$$
$$\beta_1 = \frac{k_3}{m}; \qquad \beta_2 = \frac{k_{4I}}{m}$$
$$\alpha = F\cos(\omega t) + \sigma\dot{W}(t) \tag{6.4}$$

Here, α_1 and β_1 are the onsite linear and cubic coefficients, respectively, and α_2 and β_2 are the intersite linear and cubic coefficients, respectively. The base acceleration α has been replaced with an excitation that includes a deterministic component and a noise component, which are further discussed in Section 6.4. The system given by Equation (6.3) is the uniform or homogeneous oscillator case.

6.3 Undamped homogeneous oscillator array: Restricted normal modes and influence of cubic intersite nonlinearities

The construction of the restricted modes follows the same approach as used in the group's prior work [Dick *et al.* (2009a)]. First, a symmetric group of uniform oscillators with cubic intersite coupling is isolated. Dropping the damping and external forcing terms, the resulting system is recognized to be a Hamiltonian system with a quartic potential function. Both the onsite and intersite potential function components are anharmonic in this case. For the considered localization, it is assumed that $x_{+1} = x_{-1}$, and that the influence of the ± 2 oscillators are negligible. Then, the resulting system takes the form

$$\ddot{x}_0 + \alpha_1 x_0 + \beta_1 x_0^3 + 2\alpha_2(x_0 - x_1) + 2\beta_2(x_0 - x_1)^3 = 0 \tag{6.5a}$$

$$\ddot{x}_1 \; + \; \alpha_1 x_1 \; + \; (\beta_1 \; + \; \beta_2) x_1^3 \; + \; \alpha_2 (2x_1 \; - \; x_0) \; + \; \beta_2 (x_1 \; - \; x_0)^3 \quad = \quad 0 \quad (6.5b)$$

Assuming a harmonic solution where both oscillators (the center oscillator and an adjancent oscillator) are responding with the same frequency, one can propose the solution

$$x_0 = A\cos(\omega t) \tag{6.6a}$$

$$x_1 = B\cos(\omega t) \tag{6.6b}$$

where A and B are the amplitudes of the oscillator responses, and ω is the response frequency. After substituting (6.6) into (6.5), ω^2 is eliminated. The higher harmonics are ignored. Then to parametrize $(A\,, B)$ as being a half period out of phase, $(R\,, \theta)$ is introduced and the oscillator amplitudes are expressed as

$$A = R\sin\theta \tag{6.7a}$$

$$B = R\cos\theta \tag{6.7b}$$

where R^2 is a measure of the system's total energy and θ is a phase term. The ratio of the amplitudes is

$$p = \frac{A}{B} = \tan\theta. \tag{6.7c}$$

Making use of (6.7) and the equations prior to it, a polynomial in p is obtained as.

$$p^4 + \gamma_3 p^3 + \gamma_2 p^2 + \gamma_1 p + \gamma_0 = 0 \tag{6.8}$$

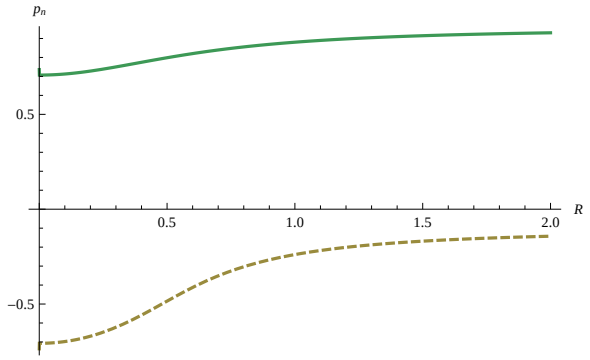

Figure 6.1: Roots of Equation (6.8) from the restricted mode approach for a uniform array of oscillators with parameters $\alpha_1 = 1.0$, $\beta_1 = 1.0$, $\alpha_2 = 0.1$, and $\beta_2 = 0.1$. Note that there are only two completely real roots for any particular R value.

where the coefficients γ_i's are defined by

$$\gamma_3 = \frac{3\left(\beta_1 - 4\beta_2\right)R^2}{2\left(4\alpha_2 + 3\beta_2 R^2\right)} \tag{6.9a}$$

$$\gamma_2 = \frac{3}{2} - \frac{4\alpha_2}{4\alpha_2 + 3\beta_2 R^2} \tag{6.9b}$$

$$\gamma_1 = \frac{3\left(\beta_2 - \beta_1\right)R^2}{2\left(4\alpha_2 + 3\beta_2 R^2\right)} \tag{6.9c}$$

$$\gamma_0 = -\frac{1}{2}. \tag{6.9d}$$

For the numerical studies, the following parameters provided in reference [Sato *et al.* (2006)] for a micro-oscillator are used: $\alpha_1 = 1.0$, $\beta_1 = 1.0$, $\alpha_2 = 0.1$, and $\beta_2 = 0.1$. In Figure 6.1, the real roots of Equation (6.8) are plotted with respect to R. It is noted that there are only 2 roots that are completely real for a given value of R, and that the other two form a complex conjugate pair. For the chosen parameter values, there is a one-to-one frequency relationship between an oscillator and an adjacent oscillator. In addition, given the cubic coupling nonlinearities and structure of the equations, one-to-one internal resonances are possible in this system (e.g. [Nayfeh and Balachandran (1989)]). Of course, other oscillator designs may be conducive for other internal resonances (e.g., [Vyas *et al.* (2009)]).

To construct the profile of the ILM for an amplitude of 1, the equation is solved

for (R, θ) such that $B = 1$. Numerically, this is performed by solving

$$1 = R\cos(\tan^{-1} p)$$

where p is a root of equation (6.8) that is a function of R. The root is chosen so that the resulting profile has the lowest energy. Only two of the roots are feasible solutions since there are always two roots with imaginary parts. The numerical solution to the above expression is $R = 1.027$, and substituting this value back into equation (6.7) leads to $A = -0.233$ and $B = 1.00$. The amplitude of the adjacent oscillator is found by taking the $|A|$ value, and solving using the other root of p

$$0.233 = R\sin(\tan^{-1} p)$$

This yields $R = 0.291$ and a corresponding pair $A = 0.262$ and $B = 0.174$. This second B value is the amplitude of the next oscillator over. The obtained localization profile is shown in Figure 6.2 along with the profile for the case when $\beta_2 = 0$ and there are no intersite or coupling cubic nonlinearities. For the considered case, the cubic coupling does have a significant affect on the responses of the oscillators adjacent to the center oscillator. The amplitudes of the adjacent oscillators are found to increase compared to the case without the coupling nonlinearities. The cubic coupling nonlinearities may be used as a means to tailor the response localization; for example, if one needs to emphasize the localization in the center oscillator, the coupling would need to be weak.

6.4 Influence of noise on localization

Next, the effects of noise on an ILM are considered. A forced and damped system is considered, with the forcing including a harmonic forcing and a noise term.

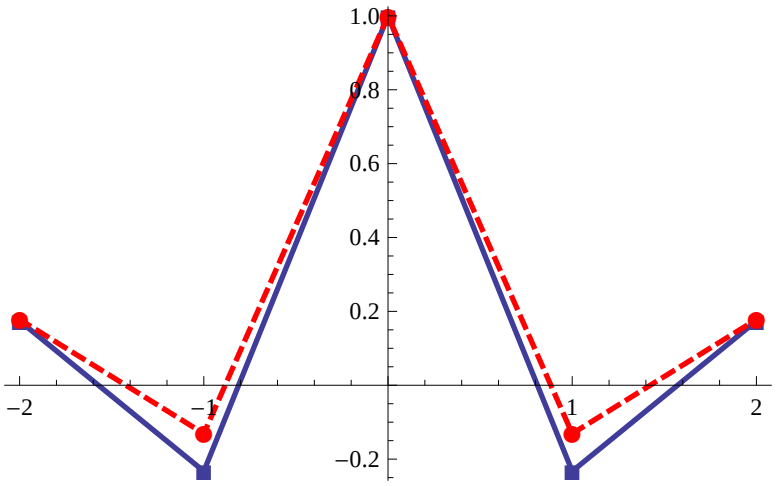

Figure 6.2: Profile of the ILM predicted from the restricted mode approach for a uniform array of oscillators with parameters $\alpha_1 = 1$, $\beta_1 = 1$, and $\alpha_2 = 0.1$. The cubic intersite coupling is $\beta_2 = 0.1$ for the solid line, and $\beta_2 = 0$ for the dashed line.

It is mentioned that in an earlier study (e.g. [Cubero *et al.* (2009)]), a harmonic forcing with a staggering factor is considered wherein the forcing amplitude F sign assumes a negative value for the odd number oscillators and a positive value for the even numbered oscillators. Here, the same forcing amplitude is used for all oscillators as in the prior work of the author's group [Ramakrishnan and Balachandran (2010, 2011)]. A staggering factor was not found to be necessary to produce a sustained response localization here. In the equation of motion (6.3), the noise amplitude will be such that $\sigma \neq 0$, in order to include the presence of noise. Since the derivative of white noise does not exist, an Euler-Maruyama scheme is used to integrate the system for varying noise amplitudes. By averaging multiple simulations with only different noise vectors, an averaged response for the system is obtained. Here, 50 separate simulations have been carried out to generate the results presented for the parameters provided in Table 6.1. The linear and nonlinear onsite and intersite parameter values match those used in the previous section, and the forcing frequency Ω is chosen such that the frequency location is above that corresponding to the jump point from the lower branch of the frequency response curve. This choice is critical so that the initial response state without the noise addition has a sufficiently large

Table 6.1: Values used in the Euler-Maruyama simulations.

Parameter	Value
α_1	1.0
α_2	0.1
β_1	1.0
β_2	0.0 or 0.1
F	0.2
$1/\tau$	0.01
Ω	1.75

amplitude. With the addition of noise, the ILM displacement profile is found to have a decreased amplitude.

Figures 6.3, 6.4, and 6.5 have been generated for the case in which the intersite coupling nonlinearities are absent (i.e. $\beta_2 = 0$). While Figure 6.3 corresponds to the no noise case, the other two cases correspond to noise of different strengths. The oscillatory responses corresponding to the localization can be seen for a pure harmonic forcing case. In the cases with noise, as the noise strength is increased, the ILM profile is attenuated. While the ILM is still present for $\sigma = 0.3$, it is well attenuated at the higher leverl of $\sigma = 0.6$. Figures 6.6, 6.7, and 6.8 are counterparts of Figures 6.3, 6.4, and 6.5 when the intersite coupling nonlinearities are present (i.e. $\beta_2 \neq 0$). Comparing Figure 6.3 and Figure 6.6, the effect of cubic coupling on the ILM profile can be observed. The considered nonlinear coupling acts to increase the participation of the adjacent oscillators in the ILM profile, consistent with what was observed in the free-oscillation case discussed in Section 6.3. The intersite nonlinearity also has the effect of decreasing the maximum amplitude of the ILM displacement. This effect is highlighted in Figures 6.9 and 6.10, for the case of $\sigma = 0$.

It should be noted that the ILM is destroyed for the case of $\sigma = 0.6$, for either $\beta_2 = 0$ (Figure 6.5) or $\beta_2 = 0.1$ (Figure 6.8). In this case, only synchronous motion is observed. For the displacement profiles (Figures 6.9 and 6.10), this synchronous motion appears as a manifestation of displacements in all oscillators. Comparing the

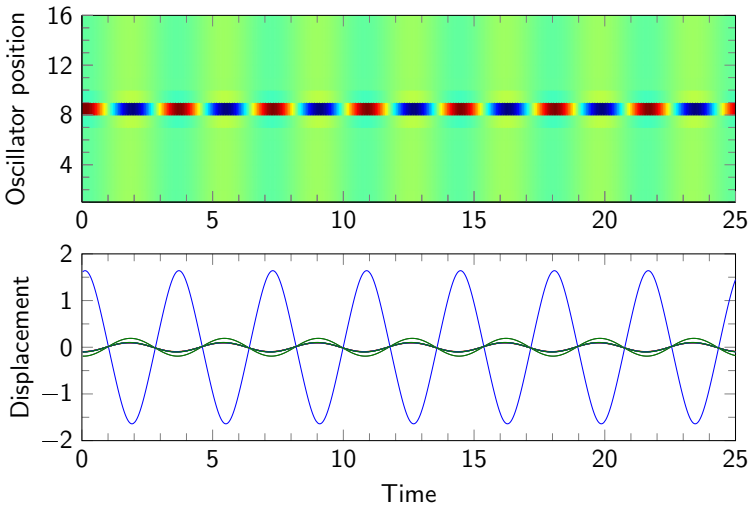

Figure 6.3: With $\beta_2 = 0$ and $\sigma = 0$, responses of oscillators in array for only the deterministic input. The oscillation with the highest relative amplitude corresponds to the oscillator in the middle of the localization.

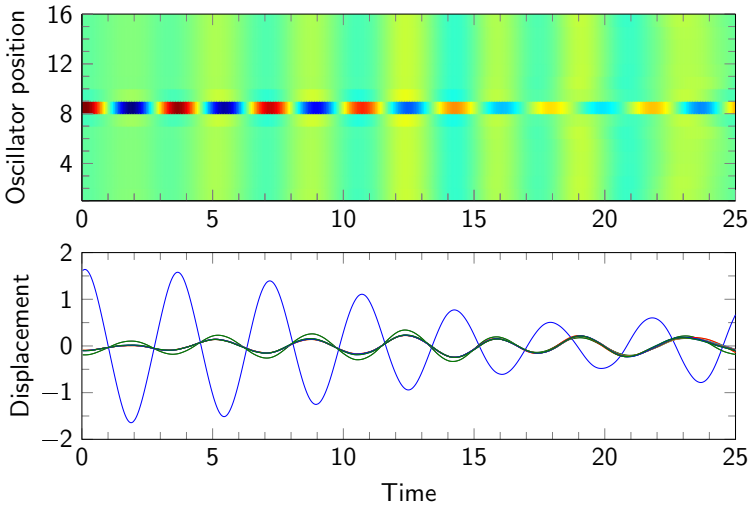

Figure 6.4: With $\beta_2 = 0$ and $\sigma = 0.3$, averaged time histories of oscillator responses. 50 Euler-Maruyama simulations have been averaged.The oscillation with the highest relative amplitude corresponds to the oscillator in the middle of the localization.

cases with and without cubic coupling, it is seen that noise destroys the ILM with cubic coupling more easily than the case without cubic coupling.

Comparing the case of $\sigma = 0.3$ in Figures 6.9 and 6.10, it is seen that the ILM for the case with cubic coupling is almost destroyed, while the case without cubic coupling still has a discernible energy localization. In designing an oscillator array,

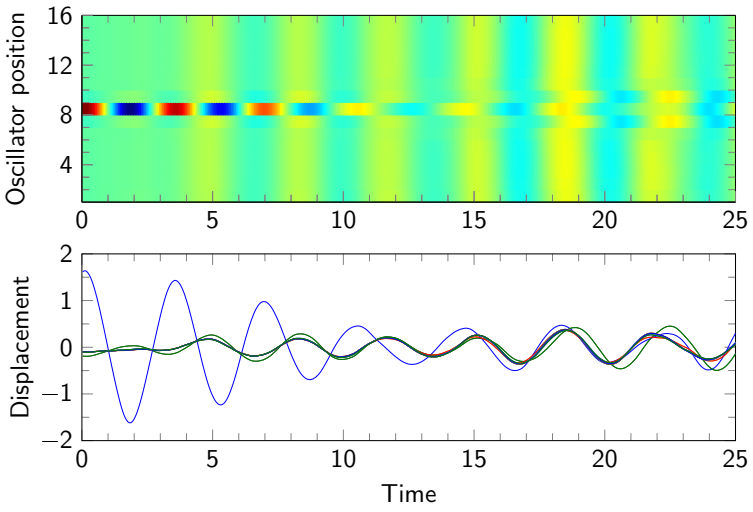

Figure 6.5: With $\beta_2 = 0$ and $\sigma = 0.6$, averaged time histories of oscillator responses. 50 Euler-Maruyama simulations have been averaged. The ILM has been destroyed.

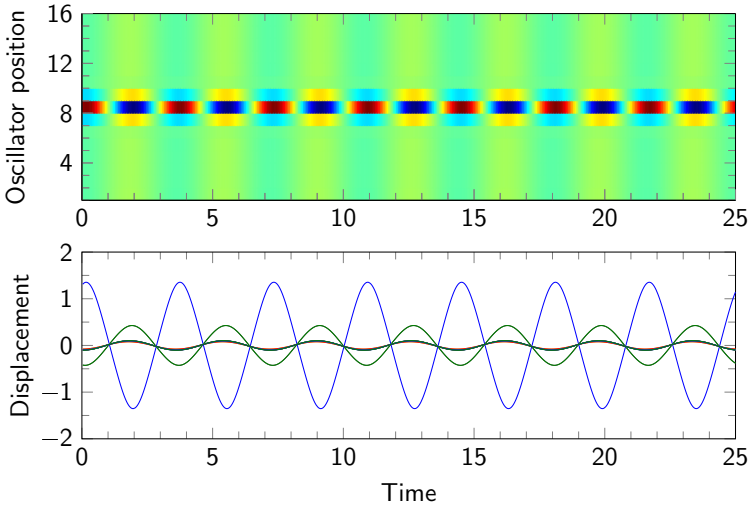

Figure 6.6: With $\beta_2 = 0.1$ and $\sigma = 0$, responses of oscillators in array for only the deterministic input.The oscillation with the highest relative amplitude corresponds to the oscillator in the middle of the localization.

this effect of noise on an ILM could be exploited. For instance, with cubic coupling, noise could be used to reset the array to an ILM-free state. Also, nonlinear coupling may be used to create ILMs with lower response localization at the center oscillator and adjacent ones. The results presented in this section are consistent with the group's prior efforts (e.g., [Ramakrishnan and Balachandran (2011)]) and others in the literature (e.g., [Cubero *et al.* (2009)]), wherein it has been noted that ILMs

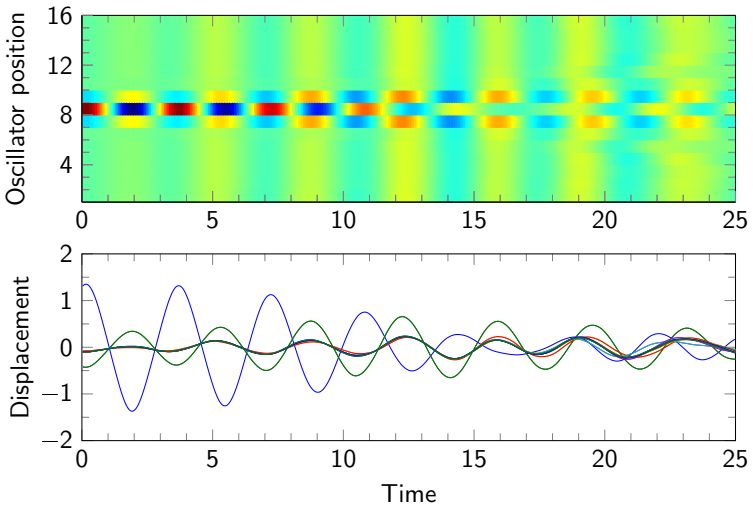

Figure 6.7: With $\beta_2 = 0.1$ and $\sigma = 0.3$, averaged time histories of oscillator responses. 50 Euler-Maruyama simulations have been averaged.The oscillation with the highest relative amplitude corresponds to the oscillator in the middle of the localization.

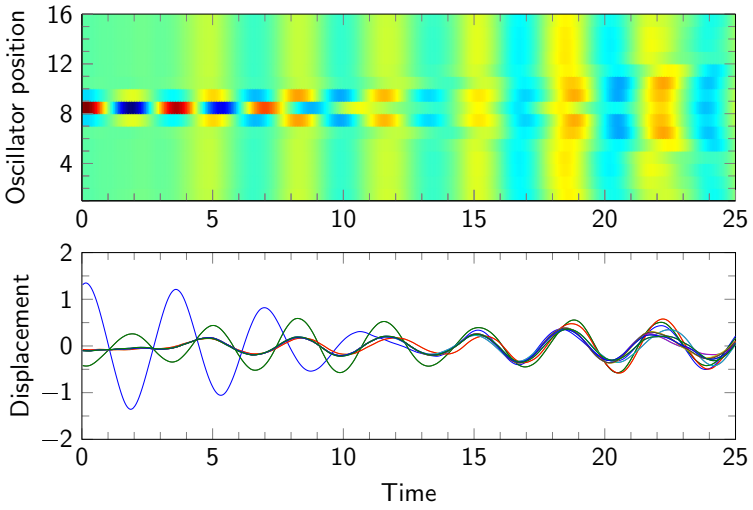

Figure 6.8: With $\beta_2 = 0.1$ and $\sigma = 0.6$, averaged time histories of oscillator responses. 50 Euler-Maruyama simulations have been averaged. The ILM has been destroyed.

exist in the presence of noise and they can be destroyed for sufficiently high noise levels. Moment evolution equations derived through a Fokker-Planck formalism was used in the earlier work of Ramakrishnan and Balachandran [Ramakrishnan and Balachandran (2011)], and certainly, that approach could be pursued here as well with the current system.

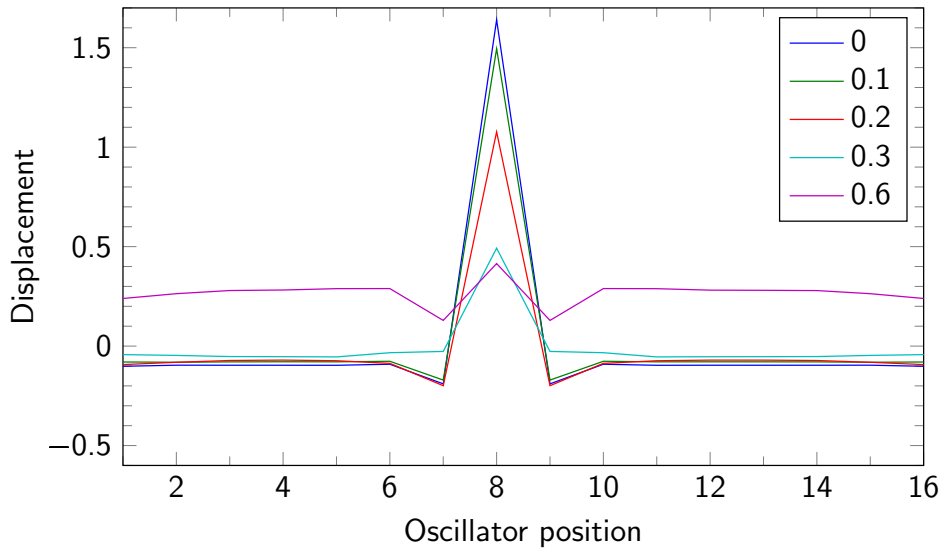

Figure 6.9: With $\beta_2 = 0$, profiles of ILM with varying levels of noise amplitude, σ. Note that for $\sigma = 0.3$, an ILM can still be seen, and the displacement is considerably different than that for the same case in Figure 6.10. For $\sigma = 0.6$, there is no ILM, but only synchronous motion.

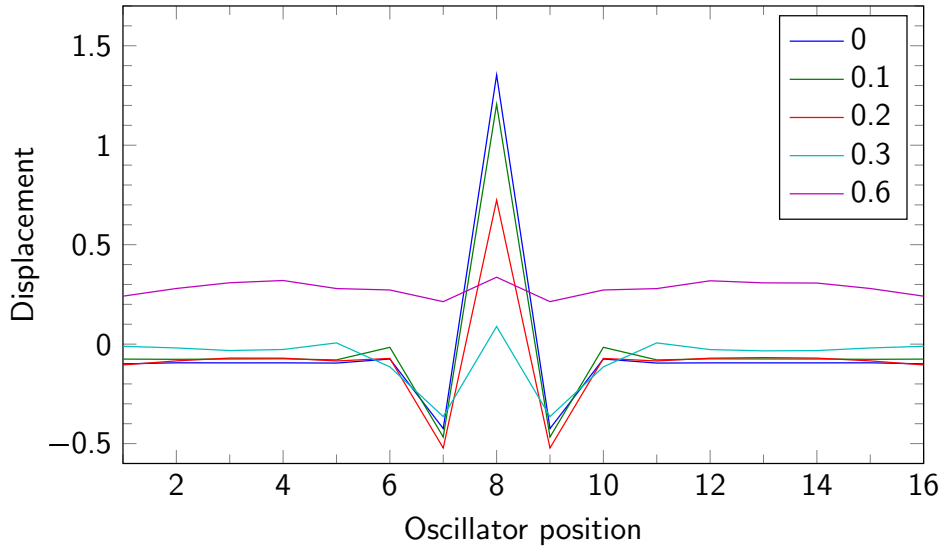

Figure 6.10: With $\beta_2 = 0.1$, profiles of ILM for varying levels of noise amplitude, σ. Note that for $\sigma = 0.3$, the ILM profile is very different from that seen for the case corresponding to Figure 6.9. For $\sigma = 0.6$, there is no ILM, but only synchronous motion.

6.5 Concluding remarks

A numerical study of energy localization in nonlinear oscillator arrays with cubic onsite nonlinearities and intersite coupling nonlinearities has been presented here. The responses of both unforced conservative systems and forced dissipative systems have been considered, and it is shown that the cubic coupling nonlinearities can be used to tailor the response levels at the center and adjacent oscillators in spatially symmetric intrinsic localized modes. The influence of noise is also considered, and it is shown that a high level of noise could be used to attenuate an intrinsic localized mode regardless of the presence of the cubic coupling nonlinearities. In addition, the studies suggest that the interplay between the cubic coupling nonlinearities and noise could be beneficial for controlling this response attenuation associated with a localization. In the context of micro-oscillator arrays, this could be important to note, since excessive amplitude levels could be determinental to the micro-oscillator system. The results presented in this work do not by any means present a full picture of the possibilities, and additional parametric studies are recommended to explore the responses for different system parameters as well as the forcing parameters. Furthermore, a better understanding of localization phenomenon could be helpful for energy distribution and harnessing systems.

Chapter 7

EFFECTS OF NOISE ON INTRINSIC LOCALIZED MODES: EXPERIMENTAL AND NUMERICAL STUDIES

As mentioned in previous chapters, intrinsic localized modes are energy localizations which can occur in arrays of coupled oscillators. They are caused by nonlinearity and discreteness. The effects of noise on intrinsic localized modes are not completely understood. Building on the efforts of the previous chapter, the author further studies the effects of noise on intrinsic localized modes, by varying the sinusoidal excitation frequency, noise amplitude, and sinusoidal amplitude. It is found that depending on the parameter values, intrinsic localized modes can be destroyed or created by utilizing noise.

The rest of this chapter is organized as follows. In the next section, some pertinent literature is given for intrinsic localized modes. In Section 7.2, the equations governing the array of nonlinear oscillators are given, and the experimental setup is explained. Euler-Maruyama simulations are presented in Section 7.3, showing the effects of noise for different sinusoidal excitation frequencies and amplitudes. The experimental results are then discussed in Section 7.4. Concluding remarks are collected together in Section 7.5.

7.1 Introduction and Background

Intrinsic localized modes (ILMs) are energy localized vibrations that are due to nonlinearity and discreteness [Sievers and Takeno (1988)]. Such energy localizations, which are also called discrete breathers (DBs), have been identified in many physical systems, ranging from nano- to macro-scale [Flach and Gorbach (2008)]. For example,

x_n	Oscillator position in state space
$\dot{x}_n$	Oscillator velocity in state space
γ	Viscous damping coefficient
K	Linear stiffness coefficient
χ_0	Coefficient in magnetic force expression due to permanent magnet
χ_1	Coefficient in magnetic force expression due to electromagnet
d_0	Equilibrium distance between magnets
Ω	Forcing frequency
ω_n	Natural frequency
A	Forcing amplitude
$\dot{W}(t)$	White Gaussian noise (derivative of Wiener process)
σ	Nondimensionalized noise amplitude in simulation
σ_{volt}	Noise amplitude in experiment

Sato *et al.* have reported that ILMs can be excited and manipulated in a micro-mechanical cantilever array [Sato *et al.* (2003a, 2006)]. Similar experiments have been performed in a macro-mechanical cantilever array [Kimura and Hikihara (2009, 2012)] in which a restoring force of each cantilever can individually be tuned. The experimental results imply that ILMs can survive under the presence of a noise, which might come from electronic circuits, ambient air flow, thermal fluctuation, and so on

On the other hand, noise will play a crucial role when the system size diminishes to nano-scale because the signal-to-noise ratio becomes small. Recently, numerical simulations on the stochastic resonance in the Fermi-Pasta-Ulam-β (FPU-β) lattice have been reported [Miloshevich, Khomeriki, and Ruffo (2009)]. In addition, it has been shown that noise helps the spontaneous formation of ILMs in a hard ϕ^4 lattice [Cubero, Cuevas, and Kevrekidis (2009)]. The effects of noise on ILMs are not completely understood. In [Cubero *et al.* (2009)], staggered forcing was utilized to produce a phenomenon similar to stochastic resonance. The Fokker-Planck equation has been used to study the effects of noise on arrays of coupled oscillators in [Ramakrishnan and Balachandran (2011); Perkins *et al.* (2013)]. In [Ramakrishnan and Balachandran (2010)], white noise was shown to destroy an ILM in an array of linearly coupled oscillators. On the other hand, in [Perkins and Balachandran

(2012)], white noise was shown to create an ILM in an array of linearly coupled oscillators.

7.2 System Equations and Experimental Setup

7.2.1 Experimental arrangement of coupled oscillators

Here, the coupled oscillator array is an array of cantilevers, which has been used in prior work of the authors Kimura and Hikihara (2009, 2012). The array schematic is illustrated in Figure 7.1.

In this cantilever array, eight cantilevers are arranged with equal separation between them. Strain gauges placed close to the fixed end of each cantilever are used to get a measure of the responses of the different cantilever oscillators. The cantilevers are coupled at the top through a coupling rod. Each cantilever has a permanent magnet at the free end at the bottom and an electromagnet placed below the permanent magnet. These magnets create a nonlinear restoring force for each cantilever, and this restoring force can be estimated by using Coulomb's law for magnetic charges.

If the displacement of the n^{th} cantilever, x_n, is sufficiently small relative to the length of the cantilever, Coulomb's law for magnetic charges can be used to obtain the force Kimura and Hikihara (2012)

$$\begin{aligned} F(x_n) =& \frac{m_{\mathrm{p}} m_{\mathrm{e}}}{4\pi\mu_0} \frac{x_n}{(x_n^2 + d_0^2)^{\frac{3}{2}}} \\ =& \chi(I_{\mathrm{EM}}) \frac{x_n}{(x_n^2 + d_0^2)^{\frac{3}{2}}}, \\ \approx& (\chi_0 + \chi_1 I_{\mathrm{EM}}) \frac{x_n}{(x_n^2 + d_0^2)^{\frac{3}{2}}}, \end{aligned} \tag{7.1}$$

where m_{p} and m_{e} correspond to the magnetic charge of PM and EM, respectively.

Table 7.1: Parameter values Kimura and Hikihara (2012)

Symbol	Value	Symbol	Value
ω_0	$2\pi\times35.1$ rad/s	γ	$1.5\ \mathrm{s}^{-1}$
K	$284\ \mathrm{s}^{-2}$	χ_0	$-4.71\times10^{-5}\ \mathrm{m}^3/\mathrm{s}^2$
d_0	3.0 mm	χ_1	$-9.14\times10^{-3}\ \mathrm{m}^3/\mathrm{s}^2\mathrm{A}$

Noting that m_e is the magnetic charge of the electromagnet, the coefficient of the force can be adjusted by varying the current flowing in the electromagnet. In the current work, the coefficient $\chi(I_\mathrm{EM})$ is approximated as the linear function, $\chi_0 + \chi_1 I_\mathrm{EM}$, where I_EM is the associate current, as shown in the restoring force equation (7.1). The experimentally estimated parameter values are listed in Table 7.1. In the experiments, the forcing amplitude is determined by making use of the measurements of the accelerometer, which is attached to the base of the array.

The coupling rod, which is located at the top of the array, deforms with relatively small amplitudes since the position of the rod is close to the fixed end of each cantilever. Hence, the coupling force can be assumed to be linear with respect to the relative displacements of adjacent cantilevers. The external forcing (both sinusoidal excitation and noise) is applied to the support where all of cantilevers' bases are fixed. This arrangement allows for a spatially uniform force to be applied to the cantilever array. Further details on the experimental arrangement are shown in Figure 7.2. The cantilever array is excited by the magnetic actuator, and the generated actuator force is proportional to the current instead of the voltage. A V/I converter is inserted between the actuator and the input signal source so that the a current input is provided to the actuator. The input signal is generated by using two function generators, one (AFG3051C, Tektronix) for the sinusoidal or harmonic input and the other (AFG3022B, Tektronix) for the noise input. Low-pass filters are used to filter out high frequency components above a chosen bandwidth. For the low-pass filter used with the noise source, the cut-off frequency is set at 234 Hz. The individual displacements of cantilever ends are determined from corresponding strain

gauge measurements, after conditioning by using a strain gauge amplifier. For the actuator induced acceleration, a tri-axis accelerometer system with module circuit (MM-2860, Sunhayato) and a micro-electromechanical accelerometer (MMA-7260QT, Freescale Semiconductor) is used. The accelerometer and strain gauge data are sampled with a sampling frequency of 10 kHz and recorded by using an eight-channel data logger (GL820, Graphtec).

The noise used in this effort is white noise, which is generated by the previously mentioned function generator (AFG3022B, Tektronix). As already noted previously, this input is band limited by sending the white noise signal through a low-pass filter. In addition, the frequency characteristics of the V/I converter and the magnetic actuator do alter the power spectral density of the noise input. The power spectral densities recorded at the output of each circuit component are shown in Figure 7.3. As shown by the curve with the label "OSC OUT," the output of the function generator exhibits an almost flat power spectral density characteristic, which is indicative of white noise. The curve labeled "LPF OUT" is the filtered output, and as expected there is a roll off past the chosen cut-off frequency of 234 Hz. The curve labeled "V/I OUT" represents the current converted by the V/I converter, where in the conversion the input voltage is multiplied by a frequency independent factor; the curves labeled "LPF OUT" and "V/I OUT" have almost the same profiles. The curve labeled "ACC. OUT" represents the acceleration applied to the support of the cantilever array. The shape of this curve strongly reflects the frequency characteristics of the magnetic actuator. However, in the frequency range from 20 Hz to 70 Hz, the power spectral density is kept almost constant. Since the first natural frequency of the cantilever system is about 35 Hz (see the curve labeled "DISP. OUT(ch1)"), the acceleration input can be considered as being "white noise" like, in the range of the first system natural frequency.

7.2.2 System equations for coupled oscillators

After reducing the governing system equations of motion, for the n^{th} cantilevered oscillator, the equation of motion is given by Kimura and Hikihara (2012):

$$\begin{aligned} \ddot{x}_n = &- \omega_0^2 x_n - \gamma \dot{x}_n + F(x_n) + A\cos(\omega t) \\ &- K(x_n - x_{n+1}) - K(x_n - x_{n-1}), \end{aligned} \tag{7.2}$$

where n is the index number for the cantilevers ranging from 1 to 8, γ is the damping coefficient for a cantilevered oscillator, K is the linear stiffness coupling coefficient, the restoring force is given by equation (7.1), and the harmonic excitation with amplitude A and frequency ω is shown. As shown in Figure 7.1, the cantilever array is fixed at its ends. With respect to Eq. (7.2), these boundary conditions mean $x_0 = x_9 = 0$. For the case with noise input as well, the governing equation for the n^{th} cantilever oscillator takes the form

$$\begin{aligned} \ddot{x}_n = &- \omega_0^2 x_n - \gamma \dot{x}_n + F(x_n) + A\cos(\omega t) \\ &- K(x_n - x_{n+1}) - K(x_n - x_{n-1}) + \sigma \dot{W}, \end{aligned} \tag{7.3}$$

where compared to Eq. (7.2), $\sigma\dot{W}$ is the additional term.

7.3 NUMERICAL RESULTS

The numerical results reported in this section have been obtained by integrating the equations of motion Eq. (7.3). This system of stochastic differential equations (SDEs) are integrated with the Euler-Maruyama scheme, as discussed in reference Higham (2001). The integration procedure starts with the differential form of the equations as discussed in the previous chapters. First, a shooting method was

applied to the deterministic equations of motion, in order to find satisfactory initial conditions to be used in the SDE studies. The amplitude profile produced by using the shooting method is shown in Figure 7.4, which is plotted as the solid curve with "+" marks correspoding to specific simulation runs.

It should be noted that the curves plotted in Figures 7.4 and 7.7 are only for reference purposes, and the symbols pertain to the actual obtained data from either simulations or experiments. The arrow, in each of these two figures, denotes that the oscillator response dropped from the ILM energy level to the low energy level seen in the deterministic case (i.e., $\sigma = 0$). Figure 7.4 was generated by averaging 100 Euler-Maruyama simulations, with distinct noise vectors.

The following points should be kept in mind when comparing the simulation results of Figure 7.4 and the experimental results of Figure 7.7. First, the noise intensity in the experiment is a complicated function of several frequency-response relationships (see Figure 7.3), while for the simulations, an assumption of white Gaussian noise is used. For this reason, noise input amplitudes used for experiments and simulations cannot be directly compared. Second, since the simulations deal with averaged dynamics, data points that lie between the ILM state and the low energy state represent cases where noise "eventually" pulled the ILM state to the low energy state. On the basis of the frequency-response curve with hysteresis for an uncoupled cantilever system (i.e., one low amplitude stable branch and high amplitude stable branch), it can be said that in an "ILM state" for a coupled system, the system response of a cantilever oscillator is on the top branch of the curve. Similary, the "low energy state" is a system response of an oscillator on the bottom branch of the hysteresis curve. In the experimental data, data points lie near the ILM curve or the low energy curve, since the response is allowed to approach a steady state. Third, response amplitudes in the simulation results shown in Figure 7.4 are found from the average response peaks; while the response amplitudes in the experimental results

shown in Figure 7.7 are found from the FFT amplitude of the response. FFTs were used in order to capture the amplitude of only the desired frequency component (i.e., the response at the amplitude of the forcing frequency component). In Figure 7.5, the averaged dynamics of the array is illustrated, where the darkness of the color plotted corresponds to the amplitude level. The ILM is destroyed in this case, as shown by the time response.

The creation of ILMs appears to be more complicated. The "breathing" effect, which lended ILMs their other name (i.e., "discrete breathers"), is observed in the frequency range above 36.5 Hz (not shown in Figure 7.7). In this range, if noise is added to an ILM-free state (i.e., when there are no ILMs present in the system response), an ILM might form. In Figure 7.6, the simulation results reveal an ILM at oscillator 4 in the beginning, with the addition of noise causing this ILM to move to oscillator 5. In addition, another ILM is seen at oscillator 2. In Figure 7.12, the experimental results are shown for a case, in which one starts from an ILM-free state. With the addition of noise, an ILM is formed at oscillator 5, and then can be seen moving to a location between oscillators 4 and 5. This complicated phenomenon needs to be explored further.

7.4 EXPERIMENTAL RESULTS

The experimental results are presented in this section. The procedure employed to obtain the set of experimental results shown in Figures 7.7 and 7.8 is as follows. First, an ILM was induced at oscillator 3, with $\sigma_{\text{volt}} = 0.0$ units and $\omega = 2\pi \times 33.5$ rad/s. Then, the frequency was gradually adjusted to the frequency values presented in Figure 7.7. These values chosen were in the range extending from 32.9 Hz (below the hysteresis range) to 36.5 Hz (below the jump in the hysteresis curve to the upper branch), and they were chosen in increments of 0.3 Hz. The frequency change was carried out quasi-statically and the responses were recorded at the frequency

locations mentioned. After the frequency was adjusted as explained, noise of different amplitudes were added to the deterministic forcing, as explained in Section 2.2.1. Throughout, the amplitude of the sinusoidal forcing was set at $A = 2.6$ units. The results obtained from this procedure are plotted in Figure 7.7. As mentioned in Figure 7.2, the data logger is used to record the acceleration signal instead of the strain response signal from the 8^{th} cantilever. Thus, while 8 oscillators are in the experimental array, only 7 are presented in the subsequent figures. The 8^{th} oscillator is not near the ILM, and so its motion is not pertinent to the dynamics of the ILM.

In the experiments, it was found that when the forcing frequency, ω, was near the "jump down" point of the hysteresis curve, even a relatively low amplitude level of noise destroyed the ILM. A typical example of noise destroying an ILM is presented in Figure 7.8. In the center of the hysteresis region, the ILM seems to be robust to noise. This can be noted from the response at points in the right portion of Figure 7.7, where the response remains near the upper branch of the hysteresis curve for the deterministic case. When the coupled oscillator array is forced with a frequency at the "upward jump" location in the hysteresis curve, it was experimentally observed that ILM movements may occur. This phenomenon was observed in a narrow band for a frequency below the frequency location for the "upward jump" point in the hysteresis curve, which was discussed at the end of Section 7.2.1.

To obtain the results shown in Figures 7.9 and 7.10, the forcing amplitude and forcing frequency are set at $A = 1.5$ units and $\omega = 2\pi \times 36.6$ rad/s. In Figure 7.9, it can be seen that only one ILM is present for $\sigma_{\text{volt}} = 0.0$ units. In Figure 7.10, with the addition of noise with $\sigma_{\text{volt}} = 10.0$ units, the ILM is observed to be destroyed. For the results shown in Figures 7.11 and 7.12, the forcing amplitude and forcing frequency are set at $A = 1.9$ units and $\omega = 2\pi \times 36.6$ rad/s. In Figure 7.11, it can be seen that no ILM is present for $\sigma_{\text{volt}} = 0.0$ units. In Figure 7.12, with the addition of noise with $\sigma_{\text{volt}} = 10.0$ units, a moving ILM is created. It was observed that if the

noise is switched off, the ILM could disappear or become pinned. Near the "jump down" point of the hysteresis curve, the dynamics of the array under the influence of noise is very complicated. More work will need to be performed to better understand the noise-influenced dynamics in this region.

7.5 CONCLUDING REMARKS

The effects of noise on the response of an array of coupled nonlinear oscillators has been studied through experiments and numerical studies. In particular, the chosen system was an array of cantilever oscillators and the focus was on how noise influenced periodic oscillations in the form of intrinsic localized modes. If one were to use a classical nonlinear oscillator frequency response curve with stable low amplitude and stable high amplitude branches, as a reference, then, near the "downward jump" point in the hysteresis curve, noise seems to destroy the pinned intrinsic localized modes. For high noise levels, the ILM behavior over a wider band of frequencies are effected. However, over the middle portion of the upper branch in the hysteresis curve (away from the jump locations), the ILM behavior appears to be robust to noise additions.

The complex dynamics noted towards the end of Sections 7.3 and 7.4 could possibly be used to develop a control scheme. It was noted that noise could be used to both create as well as destroy ILMs. There seem to be particular choices of sinusoidal forcing amplitude and the noise level, which promote this noise-influenced phenomena. However, with the current experimental arrangement, it is difficult to explore these dynamics precisely. This is in part due to the difficulty in realizing the right combination of deterministic and noise components in the system input.

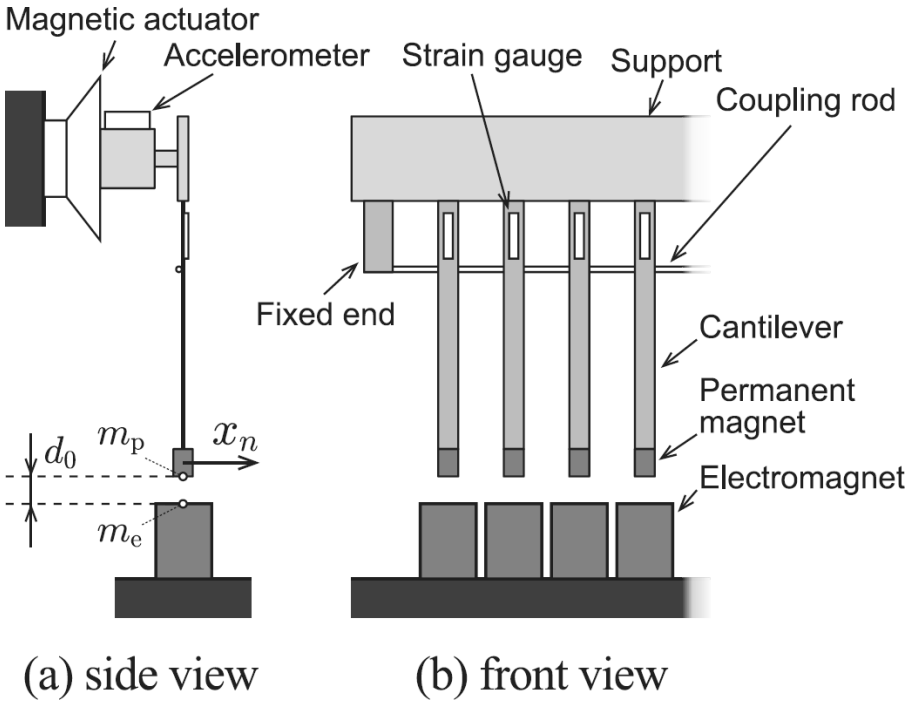

Figure 7.1: Schematic configuration of cantilever array, actuator, and sensors, studied by the author at Kyoto University. (a) Side view of a cantilever. m_p and m_e are magnetic charges of the permanent magnet and electromagnet, respectively. (b) Front view of the cantilever array.

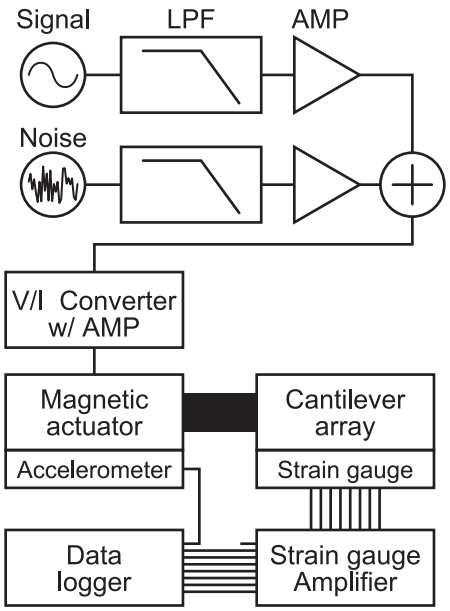

Figure 7.2: Block diagram of experimental setup. The data logger is used to record the acceleration signal instead of the strain response signal from the eighth cantilever. The capability to impose a combination of deterministic and noise excitations is also shown. The introduction of noise in the input was a new feature introduced by the author in the experimental arrangement at Kyoto University.

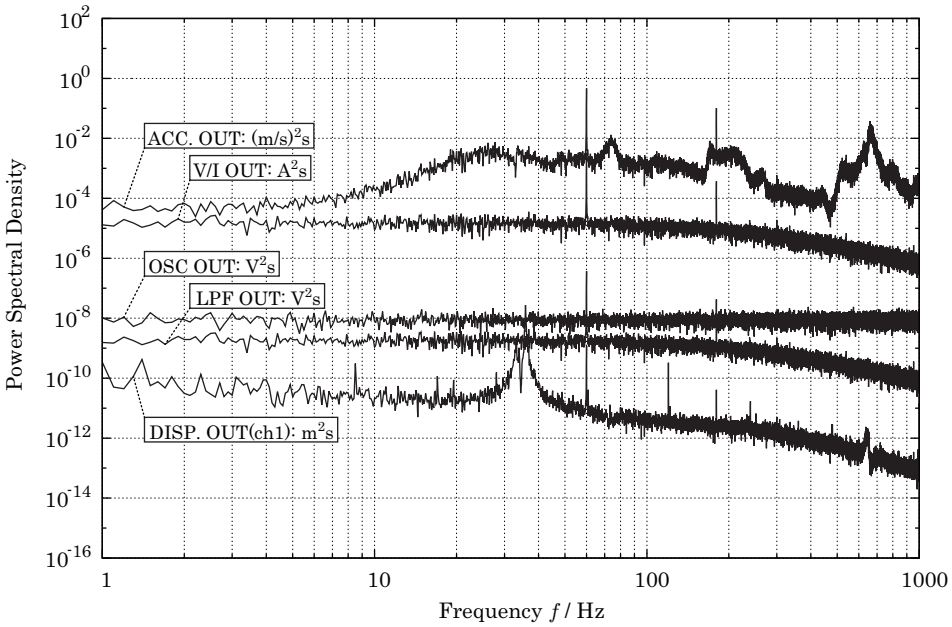

Figure 7.3: Power spectral density of noise input at different stages. All the data were recorded for 10 s at a sampling frequency of 10 kHz. The curves are obtained by averaging 10 data sets.

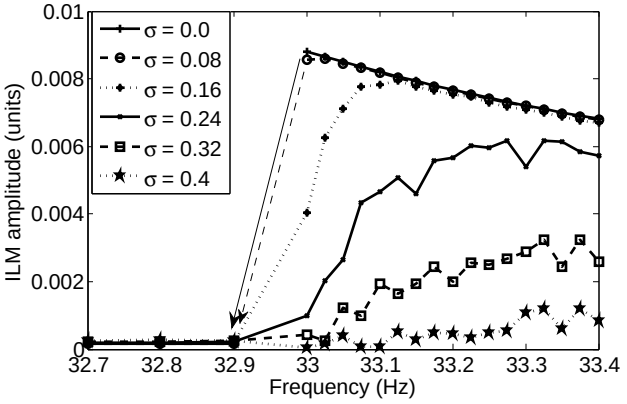

Figure 7.4: For every point on the plot, an ILM state was used as an initial condition, as found by the shooting method. After this, the noise intensity was set to the values shown in the legend. The forcing amplitude for all cases was $A = 2.6$ units, which is comparable to that used to generate the results in Figure 7.7. The arrow in this figure highlights the "falling" point of the hysteresis curve, for the deterministic case.

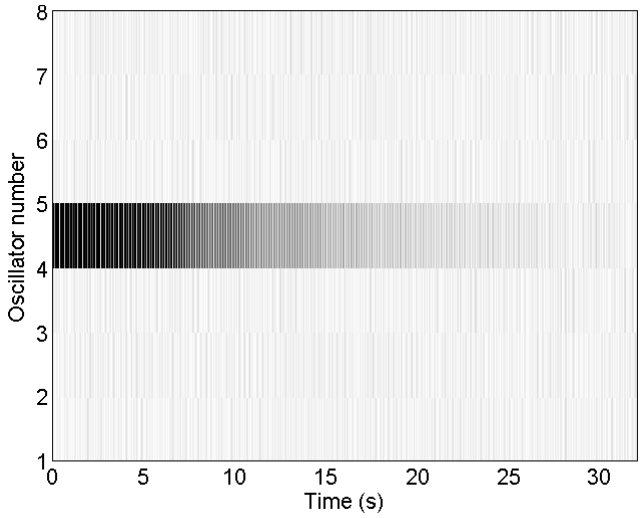

Figure 7.5: Averaged dynamics of the array for $A = 2.6$ units, $\omega = 2\pi \times 33$ rad/s, and $\sigma = 0.4$ units. Noise destroys the ILM in this case. This result may be compared to the experimental finding shown in Figure 7.8.

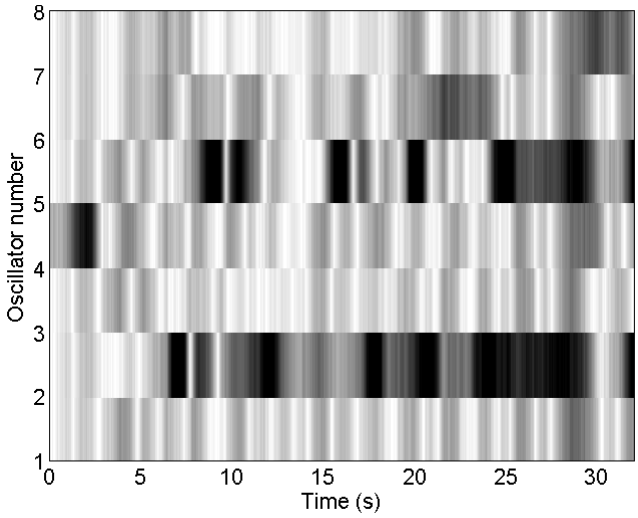

Figure 7.6: Averaged dynamics of the array for $A = 1.9$ units, $\omega = 2\pi \times 36.6$ rad/s, and $\sigma = 0.23$ units. Noise causes movement of ILM at oscillator 4 to oscillator 5, and creation of a new ILM at oscillator 2. This simulation result may be compared to the experimental finding presented in Figure 7.10.

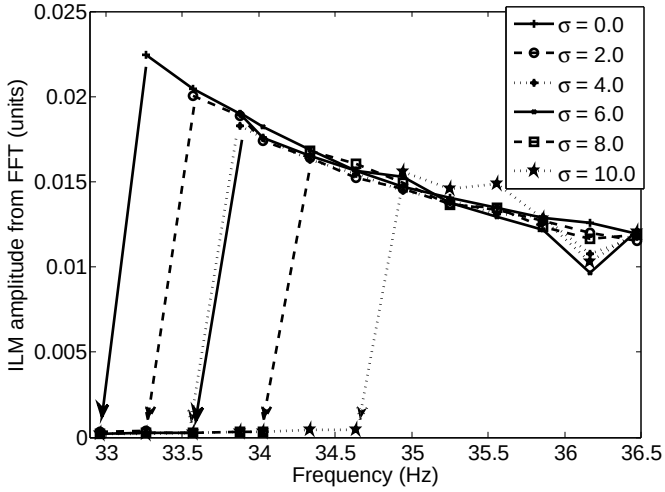

Figure 7.7: For every point marked in this plot, an ILM state was first induced with no noise. Then, the frequency of the sinusoidal excitation was adjusted to the considered frequency. After this, the noise level was set to the values in the legend. For all cases, the sinusoidal excitation amplitude was set at $A = 2.6$ units. Arrows are used to highlight the "falling" or "jump down" location in the hysteresis curve for the deterministic case.

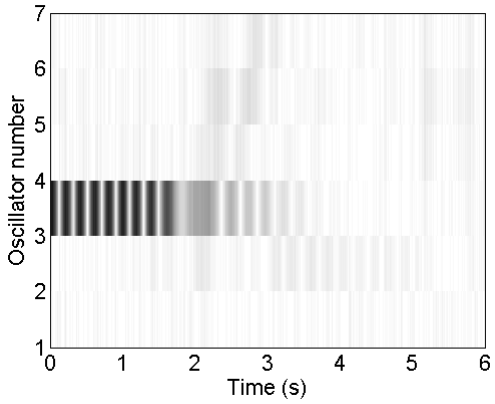

Figure 7.8: Typical example of noise destroying an ILM in the experiments. For this case, $A = 2.6$ units, $\omega = 2\pi \times 33.5$ rad/s, and $\sigma_{\text{volt}} = 8.0$ units.

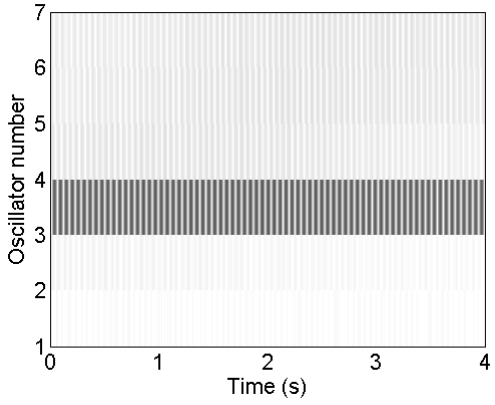

Figure 7.9: Experimental results for $A = 1.5$ units, $\omega = 2\pi \times 36.6$ rad/s, and $\sigma_{\text{volt}} = 0.0$ units, an ILM is present.

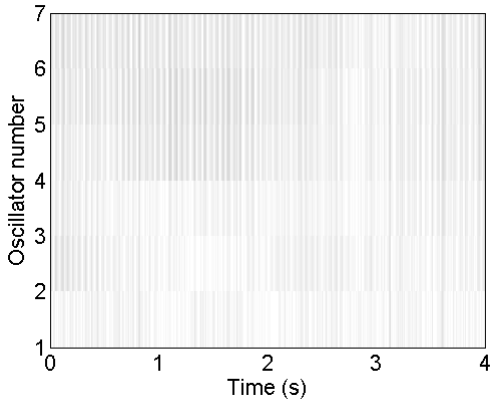

Figure 7.10: Experimental results for $A = 1.5$ units, $\omega = 2\pi \times 36.6$ rad/s, and $\sigma_{\text{volt}} = 10.0$ units. Starting from a state with an ILM (as in Figure 7.9), the ILM has been destroyed.

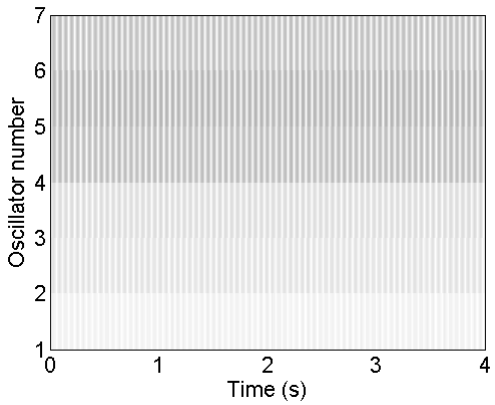

Figure 7.11: Experimental results for $A = 1.9$ units, $\omega = 2\pi \times 36.6$ rad/s, and $\sigma_{\text{volt}} = 0.0$ units. No ILM is present.

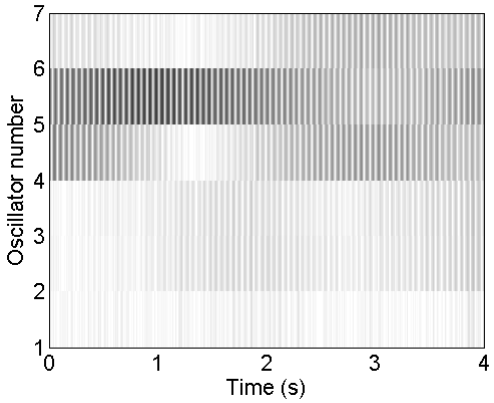

Figure 7.12: Experimental results for $A = 1.9$ units, $\omega = 2\pi \times 36.6$ rad/s, and $\sigma_{\text{volt}} = 10.0$ units. Starting from a state with no ILMs (as in Figure 7.11), ILM movements can be observed as time evolves.

Chapter 8

Summary and Recommendations for Future Work

8.1 Summary

In this dissertation work, several noise-influenced phenomena were brought to light. Also, new methods have been constructed to control and visualize the effects of noise. The phenomena discovered in this work could be used to design systems, wherein noise could be utilized in an advantageous manner. The methods, although used for oscillating systems in the context of this dissertation, could be implemented to study other systems as well. The key aspects and findings of this dissertation are the following:

1) Noise can influence bifurcations in a significant manner, including causing them to occur. In the pendulum system, the system was deterministically forced, with parameters which were near the bifurcation location of the upright position. An addition of white Gaussian noise caused the system to remain at the upright position [Perkins and Balachandran (2013)].

Similarly, for the Rayleigh-Duffing mixed type oscillator, the system was deterministically forced, with parameters which were near the chaotic bifurcation point for the broken egg attractor. An addition of white Gaussian noise, in this case, caused the system to become quasiperiodic or chaotic [Perkins and Balachandran (2012)]. A novel histogram plotting technique was used to elucidate the effects of noise on this system. This noise-induced transition could be used in a manner which is complementary to finding (2).

2) Noise can be utilized in a novel control scheme, wherein one employs noise to move the system to a desired location, after which a classical control scheme is used

to trap the system at this location [Perkins and Balachandran (2013)]. The advantage of this control scheme is that the control energy cost is only that of maintaining the system at the location; the noise energy is utilized during the possible large excursions. In systems that are noisy and in which energy consumption is expensive, this could be a useful means of control.

3) Although the effects of noise are often measured with the signal-to-noise ratio, the information metric is also a useful and necessary metric as well, when considering the oscillator to be receiving information. The phase lag has a significant effect on the information rate. Although often modeled as having a linear relationship, the phase lag is shown to be a nonlinear function of the noise level. The effects of phase lag are shown to be important in calculating the information rate [Perkins and Balachandran (2015)]. Since the information rate is important in the field of neuronal stochastic resonance, this could be a useful result in sending signals between neurons.

4) Several noise-influenced phenomena were observed for a nonlinear oscillator array.

a) When an array of coupled, nonlinear oscillators is subjected to an impulse, it was shown that noise can attenuate higher frequency components of the traveling wave [Perkins *et al.* (2013)]. A novel metric was defined in this work to elucidate the effects of this phenomenon. This attenuating phenomenon could be further studied to design arrays that use noise to attenuate energy in certain bands.

b) By studying intrinsic localized mode response as a function of input frequency, a hysteresis curve can be observed. From this starting point, the effects of noise on the ILM has been studied. Near the "jump down point" of the hysteresis curve, the ILM is easily destroyed with noise. Near the "jump up point" of the hysteresis curve for a single Duffing oscillator, complicated dynamics is possible for the array. Here, an ILM might be moved, created, or destroyed. The area between these points is

more robust to noise [Perkins *et al.* (2015)].

This work, which was both experimental and numerical, has several implications to ILM research. Noise may be used to actively destroy ILMs, if the system is operated near the "jump down point". However, if robustness to noise is desired, the system may be operated in the middle area of the hysteresis curve. If better understood, noise could be used to move ILMs, if the system was operated near the "jump up point" of the hysteresis curve.

c) The effects of noise and cubic coupling was also studied. In this work, it was found that cubic coupling allows noise to more easily destroy an ILM [Balachandran *et al.* (2014)]. By using this work and the hysteresis work discussed in (4b), systems may be designed, in which one adjusts coupling, forcing amplitude, forcing frequency, and noise amplitude to control ILMs.

Taking stochastic resonance as a starting point, the author has shown several noise-influenced phenomena which may be utilized to enhance the system dynamics. Optimization schemes could be devised, to find parameter values which best exploit the noise. An experimental setup, which can exhibit chaotic motion, might also be constructed to test both the noise-utilizing control scheme, as well as the noise-induced transition into chaos.

8.2 Recommendations for Future Work

An experimental coupled oscillator array is presented in Figure 8.1; this experimental system was designed and constructed by the author. Permanent magnets attached to the oscillators and on a plate above the oscillators provide a nonlinear spring characteristic effect.

The frequency-response curve for this experimental system is shown in Figure 8.2. The points plotted in this curve are the maximal experimental strains measured at each frequency for each oscillator, when performing a quasi-static frequency sweep.

It should be noted that the experimental frequency-response curve has a hardening character and that the upper curve is concave down, which is different from that observed with the experimental setup presented in Chapter 7.

Although the experimental setup is different than that presented in Chapter 7, similar phenomena can be observed, when the system is forced near the frequency location of the "jump down" point of the frequency-response curve. In Figure 8.3, the ILM can be observed at the fourth oscillator. This energy localization is persistent, when there is no noise. However, in Figure 8.4, the energy localization is destroyed after noise is added to the system.

The effects of noise on this experimental arrangement are suggested for further studies in the future. The differences in frequency-response curves between the experimental systems of Chapter 7 and 8 in terms of softening and hardening character, and their influence on noise-induced phenomena, require further attention.

Additionally, the modified basin of attraction for the pendulum system in Chapter 2 should be studied further. The dynamic stabilization of the upper equilibrium position requires high frequency and large amplitude oscillations. For this reason, the basin of attraction for the upper equilibrium position is a function of the frequency and amplitude of the forcing. In the system presented in Chapter 2, the basin of attraction is also a function of the noise amplitude. If this was better understood, noise-utilizing devices could be designed.

The author is currently studying the effects of noise on the single monostable Duffing oscillator's frequency-response curve. A continuation method of the cumulant equations for this system is now being undertaken as well. The effects of noise on nonlinear phenomena, such as the hysteresis behavior, could allow novel control schemes that utilize noise. For energy harvesting systems, an understanding of how noise effects the dynamics in the hysteresis region could allow an optimization of system parameters, to enable more energy to be harvested. A full understanding of

noise on this system could elucidate the role of noise for more complex systems.

Studies on the effect of noise on the different types of intrinsic localized modes (namely, the symmetric modes and and the anti-symmetric modes) could also produce fruitful results. It is possible that noise could be used to cause stability changes between these mode types. Also, studies with an array with nonlinear coupling springs could provide interesting findings.

Since deterministic nonlinear systems may exhibit complicated dynamics, the effects of noise on these systems is not trivial to predict. Understanding how noise effects the dynamics of these systems could allow better control of the system, as well as providing insight into how noise may be utilized in useful ways.

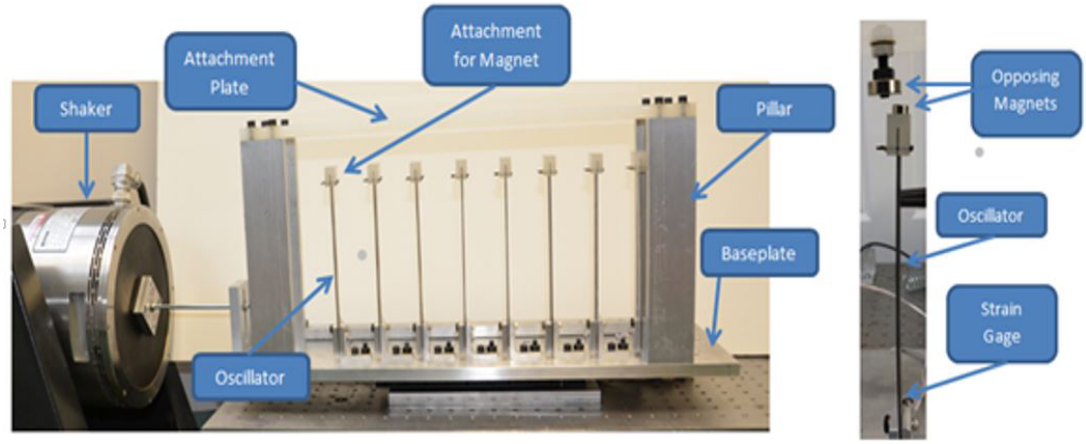

Figure 8.1: An experimental coupled oscillator array is shown. Permanent magnets attached to the oscillators and on a plate above the oscillators lead to a nonlinear hardening characteristic in the model.

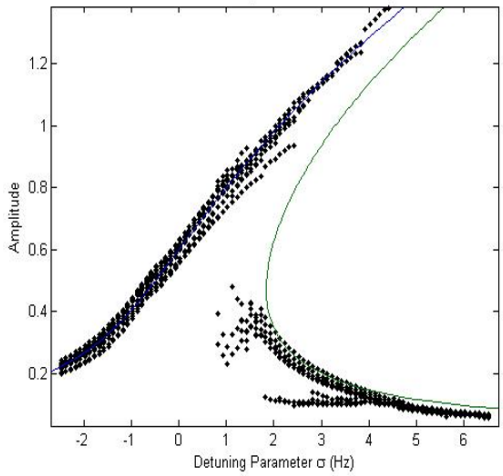

Figure 8.2: The nonlinear hardening effect may be observed from a quasi-static frequency sweep. On the x-axis, the difference between the harmonic forcing frequency and the first natural frequency of the system is shown. The points plotted are maximal experimental strains at each frequency for each oscillator. Since the oscillators are coupled, not all oscillators "jump down" from the frequency-response curve at the same time. The blue and green curves are the upper and lower branches of the predicted frequency-response curve.

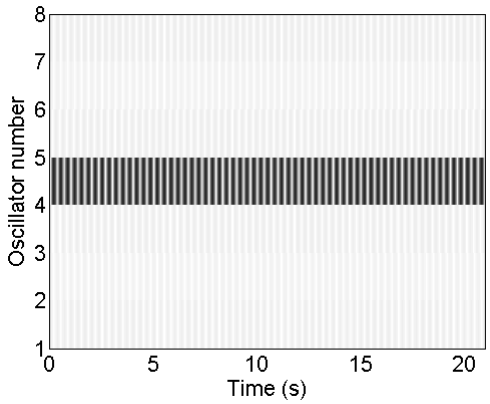

Figure 8.3: When operating near the "jump down" point of the hysteresis curve ($\omega = 2\pi \times 29.5$ rad/s), the oscillator remains at the high energy level when no noise is present.

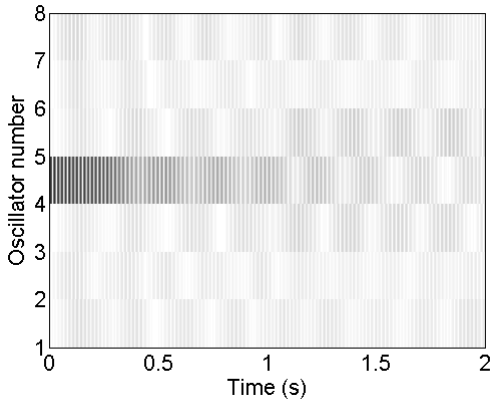

Figure 8.4: When operating near the "jump down" point of the hysteresis curve ($\omega = 2\pi \times 29.5$ rad/s), the oscillator "falls" to the lower energy level when noise is added.

A.1 Method of Multiple Scales to Derive an Approximation for Equation of Motion of Vertically Excited Pendulum

In this appendix, the derivation for an approximation for the equation of motion for a system subjected to a high-frequency, low-amplitude excitation and weak damping is provided, and this approximation is used to construct the associated dynamic potential for the pendulum system. This approximation is obtained by using the method of multiple scales Nayfeh and Balachandran (1995). The authors start with equation (2.2) and carry out the substitutions

$$\omega^2 = \epsilon\hat{\omega}^2, a = \epsilon\hat{a}, \mu = \epsilon\hat{\mu} \tag{1}$$

where ϵ is an ordering parameter. The approximation sought is of the form

$$\theta(t,\epsilon) = \theta_0(T_0, T_1, T_2, ...) + \epsilon\theta_1(T_0, T_1, T_2, ...) + \epsilon^2\theta_2(T_0, T_1, T_2, ...) + ...$$

where the different time scales are

$$T_0 = t, T_1 = \epsilon t, T_2 = \epsilon^2 t \tag{2}$$

The derivatives are then

$$\frac{d}{dt} = D_0 + \epsilon D_1 + \epsilon^2 D_2 ... \ \frac{d^2}{dt^2} = D_0^2 + 2\epsilon D_0 D_1 + \epsilon^2(D_1^2 + 2D_0 D_2) + ...$$

Re-writing equation (2.2) with these expansions, results in the following:

$$\begin{gathered}(D_0^2 + 2\epsilon D_0 D_1 + \epsilon^2 D_1^2 + 2\epsilon^2 D_0 D_2 + ...)(\theta_0 + \epsilon\theta_1 + ...) \\ +\epsilon\hat{\mu}(D_0 + \epsilon D_1 + ...)(\theta_0 + \epsilon\theta_1 + ...) - \epsilon^2\hat{\omega}^2 \sin(\theta_0 + \epsilon\theta_1 + ...) \\ -\epsilon\hat{a}\sin(\theta_0 + \epsilon\theta_1 + ...)\cos T_0 = 0\end{gathered} \tag{3}$$

Collecting terms according to ϵ, leads to the following hierarchy of equations:

$$O(1) : D_0^2\theta_0 = 0 \tag{4}$$

$$O(\epsilon) : 2D_0D_1\theta_0 + D_0^2\theta_1 + \hat{\mu}D_0\theta_0 - \hat{a}\sin\theta_0\cos T_0 = 0 \tag{5}$$

$$\begin{gathered} O(\epsilon^2) : D_0^2\theta_2 + (D_1^2 + 2D_0D_2)\theta_0 + 2D_0D_1\theta_1 + \hat{\mu}D_0\theta_1 + \hat{\mu}D_1\theta_0 \\ -\hat{\omega}^2\sin\theta_0 - \hat{a}\cos\theta_0\theta_1\cos T_0 = 0 \end{gathered} \tag{6}$$

The solution of equation (4) is $\theta_0 = c_1(T_1, T_2)t_0 + c_0(T_1, T_2)$. Since the first term is secular, the coefficient c_1 is chosen to be zero. Hence, $\theta_0 = c_0(T_1, T_2)$, which is only a function of the slow time scales. After substituting this solution into equation (5), the solution of equation (5) is determined to be $\theta_1 = -\hat{a}\sin\theta_0\cos T_0$. Next, substituting for θ_0 and θ_1 into equation (6), it is found that

$$\begin{gathered} D_0^2\theta_2 = [-(D_1^2 + 2D_0D_2)\theta_0 - \hat{\mu}D_1\theta_0 + \hat{\omega}^2\sin\theta_0 - \tfrac{\hat{a}^2}{4}\sin 2\theta_0] \\ -[2\hat{a}\cos\theta_0 D_1\theta_0 + \hat{\mu}\hat{a}\sin\theta_0]\sin T_0 - [\tfrac{\hat{a}^2}{4}\sin 2\theta_0]\cos 2T_0 \end{gathered} \tag{7}$$

Setting the sources of secular terms equal to zero, it is found that

$$(D_1^2)\theta_0 + \hat{\mu}D_1\theta_0 - \hat{\omega}^2\sin\theta_0 + \frac{\hat{a}^2}{4}\sin 2\theta_0 = 0 \tag{8}$$

This leads to

$$\ddot{\theta}_0 + \mu\dot{\theta}_0 - \omega^2\sin\theta_0 + \frac{a^2}{4}\sin 2\theta_0 = 0 \tag{9}$$

Since $\theta = \theta_0 + O(\epsilon)$, equation (2.2) can be approximated as

$$\ddot{\theta} + \mu\dot{\theta} - \omega^2\sin\theta + \frac{a^2}{4}\sin 2\theta = 0 \tag{10}$$

Hence, for $f(\theta) = \omega^2\sin\theta - \frac{a^2}{4}\sin 2\theta$, the dynamic potential of the forced pendulum system can be approximated as

$U(\theta) = -\int f(\theta)d\theta = \omega^2\cos\theta - \frac{a^2}{8}\cos 2\theta$

B.1 Sample Code

In this section, a sample code which is used to calculate and average the output of an Euler-Maruyama scheme is presented. Additionally, a code that is used for the calculating of the cumulant solutions of a nonlinear oscillator array is also shown. This latter code also contains a Shooting Method on the cumulant equations. Section B.1.1 is a simplified example of the procedure used to solve equation (3.7). Section B.1.2 is a simplified example of the procedure used to solve equation (3.15).

B.1.1 Euler-Maruyama Code

```
close all
clear all
clc

%Specify parameters to be used in equations of motion
s.parameters.k1        = 1;
s.parameters.k3        = 1;
s.parameters.zeta       = .1;
s.parameters.K          = s.parameters.k3/s.parameters.k1;
force                   = 1;
omega                   = 1;
%Specify parameters for noise amplitude and averaging
numnoise                = 1;
numaverages             = 100;

%Specify time inputs
s.time.dt      = 2^-10;
s.time.nPoints = 2^18;
indexVec       = [1:s.time.nPoints];
s.time.timeVec = [0:indexVec(end-1)]*s.time.dt;
t = s.time.timeVec;

%Specify initial conditions
s.parameters.IC(1) = 4;
s.parameters.IC(2) = 0;

s.parameters.W      = omega;
s.parameters.F      = force;

%Set the noise amplitude and noise seed
%(for the noise vector calculation)
s.parameters.sigma     = .1;   %noise amplitude
s.parameters.noiseSeed = 100;
```

```
%Precalculate the noise vector
stdNoise = sqrt(s.time.dt);
s.noise.noiseVec = ...
generateWhiteNoise(s.time.nPoints,stdNoise,s.parameters.noiseSeed);
for i1 = 1:numaverages
    solEM = nan(s.time.nPoints,2);

    %Find Euler-Maruyama solution
    solEM          = defineEM(s);
    %Store the position vector for each solution, to be
    %averaged later
    sol(:,i1)      = solEM(:,1);
end

%Average the solutions and plot the resulting averaged dynamics
ave_sol = nan(s.time.nPoints,1);
for i2 = 1:s.time.nPoints
    ave_sol(i2) = mean(sol(i2,:));
end


figure
plot(s.time.timeVec,ave_sol)
xlabel('time')
ylabel('average displacement')
```

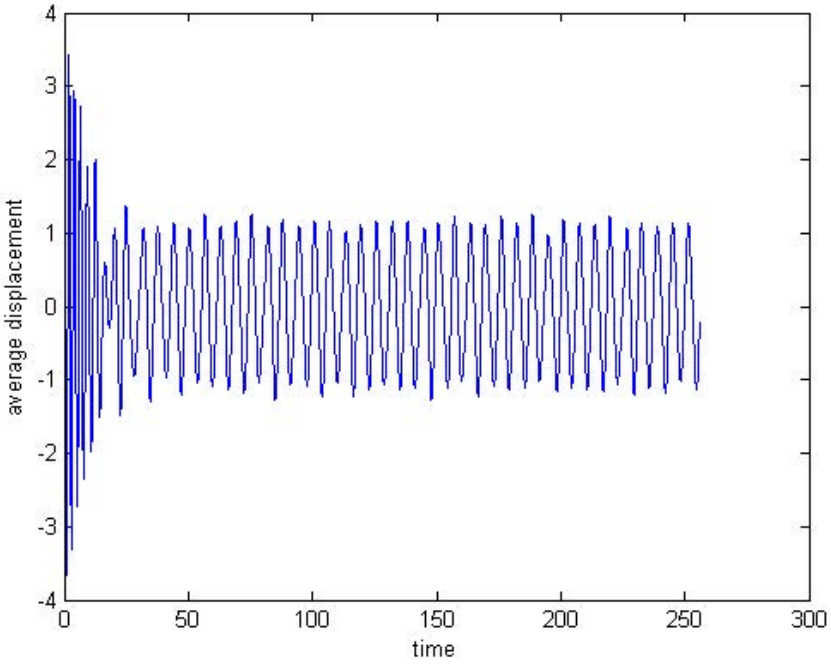

```
function solutionWithNoise = defineEM(s)


indexVec = [1:s.time.nPoints];
dt       = s.time.dt;
timeVec  = [0:indexVec(end-1)]*dt;

%Load parameters
zeta    = s.parameters.zeta;
K       = s.parameters.K;
F       = s.parameters.F;
W       = s.parameters.W;
sigma = s.parameters.sigma;
seed  = s.parameters.noiseSeed;

%Get noise values
stdNoise = sqrt(dt);
noiseVec = s.noise.noiseVec;


x1 = nan(indexVec(end),1);
x2 = nan(indexVec(end),1);


x1(1) = s.parameters.IC(1);
x2(1) = s.parameters.IC(2);


for i1 = 1:s.time.nPoints-1

   x1(i1+1) = x1(i1)+x2(i1)*dt;
   x2(i1+1) = x2(i1)+(-2*zeta*x2(i1)-x1(i1)-K*(x1(i1))^3+...
              F*cos(W*timeVec(i1)))*dt+sigma*noiseVec(i1);

end

solutionWithNoise = [x1 x2];

%Generate noise vector
%noiseVec = generateWhiteNoise(numberOfElements,StandardDeviation)

function noiseVec = generateWhiteNoise(nMax,stdNoise,seed)

s1  = RandStream.create('mt19937ar','seed',seed);
noiseVec = randn(s1,nMax,1);
```

```
noiseVec = noiseVec*stdNoise;
```

B.1.2 Cumulant Code

```
close all
clear all
clc


%Uncoupled case, because k1 and k3 are set to zero

%number of oscillators
s.parameters.nOscillators = 2;
%mass
s.parameters.m            = 1*ones(s.parameters.nOscillators,1);
%damping
s.parameters.c            = .2*ones(s.parameters.nOscillators,1);
%linear nominal
s.parameters.k0           = 1*ones(s.parameters.nOscillators,1);
%linear coupling
s.parameters.k1           = 0*ones(s.parameters.nOscillators+1,1);
%nonlinear nominal
s.parameters.k30          = 1*ones(s.parameters.nOscillators,1);
%nonlinear coupling
s.parameters.k3           = 0*ones(s.parameters.nOscillators+1,1);
%forcing amplitude
s.parameters.a            = 1;

%number of cumulant equations, from truncation procedure implemented
%on FPE
s.parameters.nEq          = 5;

nOscillators              = s.parameters.nOscillators;
nEq                       = s.parameters.nEq;

%Specify size of z
z                         = zeros(nOscillators*nEq,1);
%Specify time vector
timeVec                   = linspace(0,50*(2*pi)/1,5000);

%Set initial conditions
ic = nan(s.parameters.nOscillators,nEq,1);
for i3 = 1:s.parameters.nOscillators
    ic(i3,:,1) = [0   0    0   0   0];
```

```
end
ic_local(:,:)=ic(:,:,1);
for i5 = 1:s.parameters.nOscillators*s.parameters.nEq
    z(i5,1) = ic_local(i5);
end

s.parameters.sigma      = .1*ones(s.parameters.nOscillators,1);
s.parameters.w          = 1;

[t,sol]   =   ode15s(@defineCumulants,timeVec,z,[],s);

%Find peaks of forcing vector
[pks,locs] =
findpeaks(s.parameters.a*cos(s.parameters.w*timeVec));

%Perform Shooting Method to find fixed points of Poincare sections
iterates = 20;
p = nan(nEq*nOscillators,iterates);
n = nan(iterates-1,1);
p(:,1) = sol(locs(end-1),:);

zee = zeros(nEq*nOscillators,nEq*nOscillators+1);
shootingTime=linspace(0,(2*pi)/s.parameters.w,400);

for i0 = 1:(iterates-1)
    zee(:,1)=p(:,i0);
    zee(:,2:end) = eye(nOscillators*nEq,nOscillators*nEq);
    [tShooting,y] ...
     = ode15s(@defineCumulantShootingMethod,shootingTime,zee,[],s);

    %Shooting method iterate step
    p(:,i0+1) = p(:,i0) -...
        (reshape(y(end,(nEq*nOscillators+1):end),...
        nEq*nOscillators,nEq*nOscillators)...
        -eye(nEq*nOscillators))\(y(end,1:(nEq*nOscillators))'...
        -p(:,i0));




    %Find difference between iterates
    n(i0) = norm(p(:,i0+1)-p(:,i0));
    zee = zeros(nOscillators*nEq,nOscillators*nEq+1);
end

%Calculate floquet multipliers (eigs of
```

```
%reshape(y(end,(2*regOscillators+1):end),
%2*regOscillators,2*regOscillators))
theta = linspace(0,2*pi,300);
floq = eigs(reshape(y(end,(nEq*nOscillators+1):end),...
    nEq*nOscillators,nEq*nOscillators));

%Plot first cumulant of first oscillator (mean displacement)
figure
plot(t,sol(:,1))
xlabel('time')
ylabel('mean displacement')
```

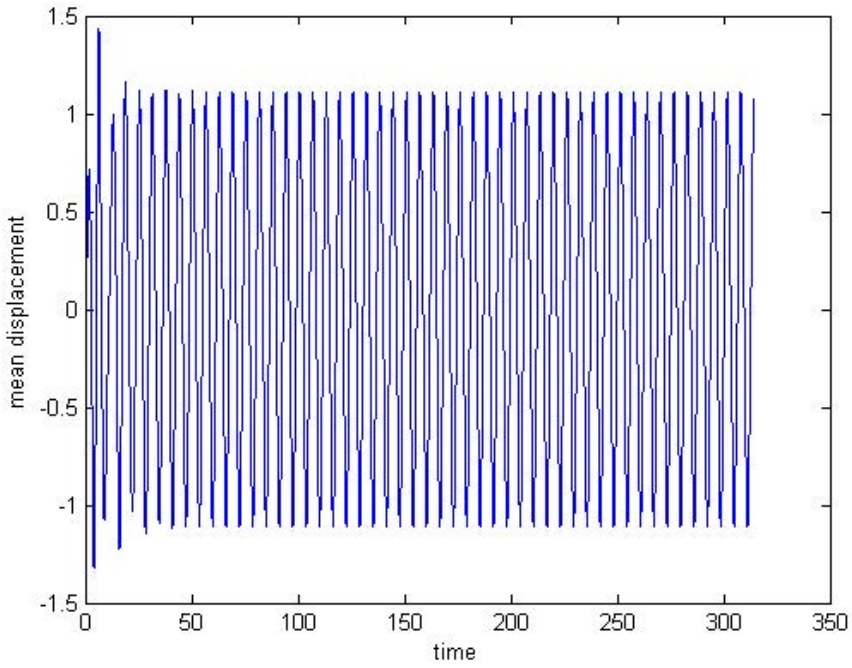


```
function dz = defineCumulants(t,z,s)

%Load parameters
nOscillators  = s.parameters.nOscillators;
m             = s.parameters.m;
c             = s.parameters.c;
k0            = s.parameters.k0;
k1            = s.parameters.k1;
k30           = s.parameters.k30;
k3            = s.parameters.k3;
a             = s.parameters.a;
sigma         = s.parameters.sigma;
nEq           = s.parameters.nEq;
```

```
w               = s.parameters.w;

% dz=zeros((nEq*nOscillators),1);
z  = reshape(z,nEq*nOscillators,1);
dz = zeros(nEq*nOscillators,1);

%Differential equations for position
%(z(1:8)) and velocity (z(9:16)).
i1 = 1;
dz(i1,1) = z(i1+nOscillators);
dz(i1+nOscillators,1) = a*cos(w*t)+ k1(i1+1)*z(i1+1) - ...
    k0(i1)*z(i1) + 2*k30(i1)*z(i1)^3 - ...
    c(i1)*z(i1+nOscillators) - ...
    3*k30(i1)*z(i1)*z(i1+2*nOscillators);

dz(i1+2*nOscillators,1) = 2*z(i1+3*nOscillators);
dz(i1+3*nOscillators,1) = z(i1)*(a*cos(w*t) + k1(i1+1)*...
    z(i1+1) + 2*k30(i1)*z(i1)^3) ...
    - k0(i1)*z(i1+2*nOscillators) - ...
    3*k30(i1)*z(i1+2*nOscillators)^2 ...
    - c(i1)*z(i1+3*nOscillators) +...
    z(i1+4*nOscillators);
dz(i1+4*nOscillators,1) = sigma(i1)^2 + 2*((a*cos(w*t) + ...
    k1(i1+1)*z(i1+1) + 2*k30(i1)*z(i1)^3)*z(i1+nOscillators)...
     - k0(i1)*...
    z(i1+3*nOscillators) - 3*k30(i1)*z(i1+2*nOscillators)*...
    z(i1+3*nOscillators) - c(i1)*z(i1+4*nOscillators));

for i1 = 2:nOscillators - 1

    dz(i1,1) = z(i1+nOscillators);
    dz(i1+nOscillators,1) = a*cos(w*t) + k1(i1)*z(i1-1) + ...
        k1(i1+1)*z(i1+1) - k0(i1)*z(i1) + 2*k30(i1)*z(i1)^3 -...
        c(i1)*z(i1+nOscillators) ...
        - 3*k30(i1)*z(i1)*z(i1+2*nOscillators);

    dz(i1+2*nOscillators,1) = 2*z(i1+3*nOscillators);
    dz(i1+3*nOscillators,1) = z(i1)*(a*cos(w*t) ...
     + k1(i1)*z(i1-1) + ...
        k1(i1+1)*z(i1+1) + 2*k30(i1)*z(i1)^3) ...
        - k0(i1)*...
        z(i1+2*nOscillators) ...
        - 3*k30(i1)*z(i1+2*nOscillators)^2 -...
        c(i1)*z(i1+3*nOscillators) ...
        + z(i1+4*nOscillators);
```

```
    dz(i1+4*nOscillators,1) = sigma(i1)^2 + 2*((a*cos(w*t) + ...
        k1(i1)*z(i1-1) + k1(i1+1)*z(i1+1) + 2*k30(i1)*z(i1)^3)*...
        z(i1+nOscillators) - k0(i1)*z(i1+3*nOscillators)...
         - 3*k30(i1)...
        *z(i1+2*nOscillators)*z(i1+3*nOscillators) - c(i1)*...
        z(i1+4*nOscillators));

end

i1 = nOscillators;
dz(i1,1) = z(i1+nOscillators);
dz(i1+nOscillators,1) = a*cos(w*t) + k1(i1)*z(i1-1) ...
- k0(i1)*z(i1) ...
    + 2*k30(i1)*z(i1)^3 - c(i1)*z(i1+nOscillators) ...
    - 3*k30(i1)*z(i1)*...
    z(i1+2*nOscillators);

dz(i1+2*nOscillators,1) = 2*z(i1+3*nOscillators);
dz(i1+3*nOscillators,1) = z(i1)*(a*cos(w*t) + k1(i1)*z(i1-1)+ ...
    2*k30(i1)*z(i1)^3) - k0(i1)*z(i1+2*nOscillators) - 3*k30(i1)*...
    z(i1+2*nOscillators)^2 - c(i1)*z(i1+3*nOscillators) + ...
    z(i1+4*nOscillators);
dz(i1+4*nOscillators,1) = sigma(i1)^2 + 2*((a*cos(w*t)...
 + k1(i1)*z(i1-1) ...
    + 0 + 2*k30(i1)*z(i1)^3)*z(i1+nOscillators) - k0(i1)*...
    z(i1+3*nOscillators) - 3*k30(i1)*z(i1+2*nOscillators)*...
    z(i1+3*nOscillators) - c(i1)*z(i1+4*nOscillators));

function dz = defineCumulantShootingMethod(t,z,s)
%Shooting method for coupled oscillator experiment

%Load parameters
nOscillators        = s.parameters.nOscillators;
c                   = s.parameters.c;
k0                  = s.parameters.k0;
k1                  = s.parameters.k1;
k30                 = s.parameters.k30;
k3                  = s.parameters.k3;
w                   = s.parameters.w;
a                   = s.parameters.a;
sigma               = s.parameters.sigma;
nEq                 = s.parameters.nEq;

% dz=zeros((nEq*nOscillators),1);
z  = reshape(z,nEq*nOscillators,(nEq*nOscillators)+1);
```

```
dz = zeros(nEq*nOscillators,(nEq*nOscillators)+1);
var = zeros(nEq*nOscillators,nEq*nOscillators);


alpha = zeros(nOscillators,nOscillators);
beta = zeros(nOscillators,nOscillators);
gamma = zeros(nOscillators,nOscillators);
delta = zeros(nOscillators,nOscillators);
epsilon = zeros(nOscillators,nOscillators);
zeta = zeros(nOscillators,nOscillators);
eta = zeros(nOscillators,nOscillators);
iota = zeros(nOscillators,nOscillators);



%differential equations for position (z(1:8))
%and velocity (z(9:16)).
i1 = 1;

dz(i1,1) = z(i1+nOscillators);
dz(i1+nOscillators,1) = a*cos(w*t) + k1(i1+1)*z(i1+1) -...
    k0(i1)*z(i1) + 2*k30(i1)*z(i1)^3 ...
    - c(i1)*z(i1+nOscillators) - ...
    3*k30(i1)*z(i1)*z(i1+2*nOscillators);

dz(i1+2*nOscillators,1) = 2*z(i1+3*nOscillators);
dz(i1+3*nOscillators,1) = z(i1)*(a*cos(w*t) + ...
    k1(i1+1)*z(i1+1) + 2*k30(i1)*z(i1)^3) ...
    - k0(i1)*z(i1+2*nOscillators) ...
    - 3*k30(i1)*z(i1+2*nOscillators)^2 ...
    - c(i1)*z(i1+3*nOscillators) ...
    + z(i1+4*nOscillators);
dz(i1+4*nOscillators,1) = sigma(i1)^2 + 2*((a*cos(w*t) + ...
    k1(i1+1)*z(i1+1) + 2*k30(i1)*z(i1)^3)*z(i1+nOscillators) - ...
    k0(i1)*z(i1+3*nOscillators) ...
    - 3*k30(i1)*z(i1+2*nOscillators)*...
    z(i1+3*nOscillators) - c(i1)*z(i1+4*nOscillators));



for i1 = 2:nOscillators - 1


    dz(i1,1) = z(i1+nOscillators);
    dz(i1+nOscillators,1) = a*cos(w*t) + k1(i1)*z(i1-1) + ...
```

```
        k1(i1+1)*z(i1+1) - k0(i1)*z(i1) + 2*k30(i1)*z(i1)^3 -...
        c(i1)*z(i1+nOscillators) ...
        - 3*k30(i1)*z(i1)*z(i1+2*nOscillators);

    dz(i1+2*nOscillators,1) = 2*z(i1+3*nOscillators);
    dz(i1+3*nOscillators,1) = z(i1)*(a*cos(w*t) ...
     + k1(i1)*z(i1-1) + ...
        k1(i1+1)*z(i1+1) + 2*k30(i1)*z(i1)^3) - k0(i1)*...
        z(i1+2*nOscillators) ...
        - 3*k30(i1)*z(i1+2*nOscillators)^2 - ...
        c(i1)*z(i1+3*nOscillators) + z(i1+4*nOscillators);
    dz(i1+4*nOscillators,1) = sigma(i1)^2 ...
     + 2*((a*cos(w*t) + ...
        k1(i1)*z(i1-1) + k1(i1+1)*z(i1+1) + 2*k30(i1)*z(i1)^3)*...
        z(i1+nOscillators) - k0(i1)*z(i1+3*nOscillators) ...
        - 3*k30(i1)*z(i1+2*nOscillators)*z(i1+3*nOscillators)...
        - c(i1)*...
        z(i1+4*nOscillators));


end



i1 = nOscillators;

dz(i1,1) = z(i1+nOscillators);
dz(i1+nOscillators,1) = a*cos(w*t) + k1(i1)*z(i1-1) ...
- k0(i1)*z(i1) ...
    + 2*k30(i1)*z(i1)^3 - c(i1)*z(i1+nOscillators) ...
    - 3*k30(i1)*z(i1)*z(i1+2*nOscillators);

dz(i1+2*nOscillators,1) = 2*z(i1+3*nOscillators);
dz(i1+3*nOscillators,1) = z(i1)*(a*cos(w*t) ...
+ k1(i1)*z(i1-1) + ...
    2*k30(i1)*z(i1)^3) - k0(i1)*z(i1+2*nOscillators) ...
    - 3*k30(i1)*...
    z(i1+2*nOscillators)^2 - c(i1)*z(i1+3*nOscillators) + ...
    z(i1+4*nOscillators);
dz(i1+4*nOscillators,1) = sigma(i1)^2 + 2*((a*cos(w*t) ...
+ k1(i1)*z(i1-1) ...
    + 0 + 2*k30(i1)*z(i1)^3)*z(i1+nOscillators) - k0(i1)*...
    z(i1+3*nOscillators) - 3*k30(i1)*z(i1+2*nOscillators)*...
    z(i1+3*nOscillators) - c(i1)*z(i1+4*nOscillators));
```

```
%Construct DxF*cos(w*t) (variational matrix)
for i7 = 2:(nOscillators)
    delta(i7,i7) = 2*k1(1)*z(i7-1);
end
for i7 = 1:nOscillators-1
    delta(i7,i7) = delta(i7,i7)+2*k1(1)*z(i7+1);
end

for i7 = 2:(nOscillators)
    beta(i7,i7) = k1(1)*z(i7-1);
end
for i7 = 1:nOscillators-1
    beta(i7,i7) = beta(i7,i7)+k1(1)*z(i7+1);
end
for i6 = 1:nOscillators

    alpha(i6,i6) = -k0(1)+6*k30(1)*z(i6)^2-3*k30(1)...
    *z(i6+2*nOscillators);
    for i7 = 1:(nOscillators-1)
        alpha(i7,i7+1)     = k1(1);
        alpha(i7+1,i7)     = k1(1);
    end

    beta(i6,i6) = beta(i6,i6) + a*cos(w*t)+8*k30(1)*z(i6)^3;
    for i7 = 1:(nOscillators-1)
        beta(i7,i7+1)     = k1(1)*z(i7);
        beta(i7+1,i7)     = k1(1)*z(i7+1);
    end

    gamma(i6,i6) = 12*k30(1)*z(i6)^2*z(i6+nOscillators);
    for i7 = 1:(nOscillators-1)
        gamma(i7,i7+1)     = 2*k1(1)*z(i7+nOscillators);
        gamma(i7+1,i7)     = 2*k1(1)*z(i7+1+nOscillators);
    end

    delta(i6,i6) = delta(i6,i6) ...
     + 2*a*cos(w*t)+4*k30(1)*z(i6)^3;

    epsilon(i6,i6) = -3*k30(1)*z(i6);

    zeta(i6,i6) = -k0(1)-6*k30(1)*z(i6+2*nOscillators);

    eta(i6,i6)  = -6*k30(1)*z(i6+3*nOscillators);
```

```
    iota(i6,i6) = 2*(-k0(1)-3*k30(1)*z(i6+2*nOscillators));

end

var = [zeros(nOscillators,nOscillators),
eye(nOscillators,nOscillators),...
    zeros(nOscillators,nOscillators),
    zeros(nOscillators,nOscillators),...
    zeros(nOscillators,nOscillators);...
    alpha,-c(1)*eye(nOscillators,nOscillators),epsilon,...
    zeros(nOscillators,nOscillators),
    zeros(nOscillators,nOscillators);...
    zeros(nOscillators,nOscillators),
    zeros(nOscillators,nOscillators),...
    zeros(nOscillators,nOscillators),
    2*eye(nOscillators,nOscillators),...
    zeros(nOscillators,nOscillators);...
    beta,zeros(nOscillators,nOscillators),zeta,
    -c(1)*eye(nOscillators,...
    nOscillators),eye(nOscillators,nOscillators);...
    gamma,delta,eta,iota,-2*c(1)*eye(nOscillators,nOscillators)];

dz(:,2:end) = var*z(:,2:end);

dz = reshape(dz,nEq*nOscillators+(nEq*nOscillators)^2,1);
```

Bibliography

Abraham, R. and Ueda, Y. (2001). *The chaos avant-garde: Memories of the early days of chaos theory*, volume 39. World scientific.

Almog, R., Zaitsev, S., Shtempluck, O., and Buks, E. (2007). Signal amplification in a nanomechanical duffing resonator via stochastic resonance. *Applied physics letters* **90**(1), 013508.

Anderson, P.W. (1958). Absence of diffusion in certain random lattices. *Physical review* **109**(5), 1492.

Andreev, A., Kanto, A., and Malo, P. (2005). Simple approach for distribution selection in the pearson system. *Helsinki School of Economics Working Papers* .

Badzey, R.L. and Mohanty, P. (2005). Coherent signal amplification in bistable nanomechanical oscillators by stochastic resonance. *Nature* **437**(7061), 995–998.

Balachandran, B., Perkins, E., and Fitzgerald, T. (2014). Response localization in micro-scale oscillator arrays: influence of cubic coupling nonlinearities. *International Journal of Dynamics and Control* **3**(2), 1–6.

Benzi, R., Parisi, G., Sutera, A., and Vulpiani, A. (1982). Stochastic resonance in climatic change. *Tellus* **34**(1), 10–16.

Benzi, R., Sutera, A., and Vulpiani, A. (1981). The mechanism of stochastic resonance. *Journal of Physics A: mathematical and general* **14**, L453.

Bulsara, A.R. and Zador, A. (1996). Threshold detection of wideband signals: A noise-induced maximum in the mutual information. *Physical Review E* **54**(3), R2185–R2188.

Campbell, D.K., Flach, S., and Kivshar, Y.S. (2004). Localizing energy through nonlinearity and discreteness. *Physics Today* **57**(1), 43–49.

Chabalko, C., Jordan, D., Hajj, M., and Tieleman, H. (2005). Characteristic time scales of velocity and pressure events. *Journal of fluids and structures* **20**(8), 1057–1071.

Chakraborty, I. and Balachandran, B. (2011). Noise influenced elastic cantilever dynamics with nonlinear tip interaction forces. *Nonlinear Dynamics* **66**(3), 427–439.

Chapeau-Blondeau, F. (1997). Noise-enhanced capacity via stochastic resonance in an asymmetric binary channel. *Physical Review E* **55**(2), 2016.

Chapeau-Blondeau, F., Blanchard, S., and Rousseau, D. (2006). Noise-enhanced fisher information in parallel arrays of sensors with saturation. *Physical Review E* **74**(3), 031102.

Chorin, A. and Hald, O. (2009). *Stochastic tools in mathematics and science*, volume 1. Springer Verlag.

Collins, J., Chow, C.C., Capela, A.C., and Imhoff, T.T. (1996). Aperiodic stochastic resonance. *Physical Review E* **54**(5), 5575.

Cubero, D., Cuevas, J., and Kevrekidis, P. (2009). Nucleation of breathers via stochastic resonance in nonlinear lattices. *Physical review letters* **102**(20), 205505.

Dick, A.J., Balachandran, B., and Mote, Jr, C.D. (2008). Intrinsic localized modes in microresonator arrays and their relationship to nonlinear vibration modes. *Nonlinear Dynamics* **54**(1-2), 13–29.

Dick, A.J., Balachandran, B., and Mote, Jr, C.D. (2009a). Localization in microresonator arrays: Influence of natural frequency tuning. *ASME Journal of Computational and Nonlinear Dynamics* **5**, 011002–1–011002–11.

Dick, A.J., Balachandran, B., Yabuno, H., Numatsu, M., Hayashi, K., Kuroda, M., and Ashida, K. (2009b). Utilizing nonlinear phenomena to locate grazing in the constrained motion of a cantilever beam. *Nonlinear Dynamics* **57**(3), 335–349.

Dorigo, M. and Blum, C. (2005). Ant colony optimization theory: A survey. *Theoretical computer science* **344**(2), 243–278.

Douglass, J.K., Wilkens, L., Pantazelou, E., and Moss, F. (1993). Noise enhancement of information transfer in crayfish mechanoreceptors by stochastic resonance. *Nature* **365**(6444), 337–340.

Dussutour, A., Beekman, M., Nicolis, S.C., and Meyer, B. (2009). Noise improves collective decision-making by ants in dynamic environments. *Proceedings of the Royal Society of London B: Biological Sciences* **276**(1677), 4353–4361.

Dykman, M., Mannella, R., McClintock, P.V., and Stocks, N. (1992). Phase shifts in stochastic resonance. *Physical review letters* **68**(20), 2985.

Flach, S. and Gorbach, A.V. (2008). Discrete breathersadvances in theory and applications. *Physics Reports* **467**(1), 1–116.

Fleischer, J.W., Segev, M., Efremidis, N.K., and Christodoulides, D.N. (2003). Observation of two-dimensional discrete solitons in optically induced nonlinear photonic lattices. *Nature* **422**, 147–150.

Gammaitoni, L., Hänggi, P., Jung, P., and Marchesoni, F. (1998). Stochastic resonance. *Reviews of Modern Physics* **70**(1), 223–287.

Gardiner, C. (1985). *Stochastic methods*. Springer.

Godivier, X. and Chapeau-Blondeau, F. (1998). Stochastic resonance in the information capacity of a nonlinear dynamic system. *International Journal of Bifurcation and Chaos* **8**(03), 581–589.

Guderian, A., Dechert, G., Zeyer, K.P., and Schneider, F. (1996). Stochastic resonance in chemistry. 1. the belousov-zhabotinsky reaction. *The Journal of Physical Chemistry* **100**(11), 4437–4441.

Hänggi, P. (2002). Stochastic resonance in biology how noise can enhance detection of weak signals and help improve biological information processing. *ChemPhysChem* **3**(3), 285–290.

Hidaka, I., Nozaki, D., and Yamamoto, Y. (2000). Functional stochastic resonance in the human brain: noise induced sensitization of baroreflex system. *Physical review letters* **85**(17), 3740–3743.

Higham, D. (2001). An algorithmic introduction to numerical simulation of stochastic differential equations. *SIAM review* 525–546.

Jaramillo, F. and Wiesenfeld, K. (1998). Mechanoelectrical transduction assisted by brownian motion: a role for noise in the auditory system. *Nature neuroscience* **1**(5), 384–388.

Jung, P., Behn, U., Pantazelou, E., and Moss, F. (1992). Collective response in globally coupled bistable systems. *Physical Review A* **46**(4), R1709.

Kao, J. and Wihstutz, V. (2000). Characterization of stochastic processes which stabilize linear companion form systems. *Stochastic processes and their applications* **89**(1), 49–68.

Kimura, M. and Hikihara, T. (2009). Coupled cantilever array with tunable on-site nonlinearity and observation of localized oscillations. *Physics Letters A* **373**(14), 1257–1260.

Kimura, M. and Hikihara, T. (2012). Experimental manipulation of intrinsic localized modes in macro-mechanical system. *Nonlinear Theory and Its Applications, IEICE* **3**(2), 233–245.

Kimura, M., Matsushita, Y., and Hikihara, T. (2013). A study on feedback control of intrinsic localized modes in a micro-mechanical cantilever array. In *2013 International Symposium on Nonlinear Theory and its Applications*, 282–285.

Kish, L.B., Harmer, G.P., and Abbott, D. (2001). Information transfer rate of neurons: stochastic resonance of shannon's information channel capacity. *Fluctuation and Noise Letters* **1**(01), L13–L19.

Leonard, D.S. and Reichl, L. (1994). Stochastic resonance in a chemical reaction. *Physical Review E* **49**(2), 1734.

Lepik, Ü. and Hein, H. (2005). On response of nonlinear oscillators with random frequency of excitation. *Journal of sound and vibration* **288**(1), 275–292.

Levin, J.E. and Miller, J.P. (1996). Broadband neural encoding in the cricket cereal sensory system enhanced by stochastic resonance. *Nature* **380**(6570), 165–168.

Lindner, J.F., Bennett, M., and Wiesenfeld, K. (2006). Potential energy landscape and finite-state models of array-enhanced stochastic resonance. *Physical Review E* **73**(3), 031107.

McNamara, B., Wiesenfeld, K., and Roy, R. (1988). Observation of stochastic resonance in a ring laser. *Physical Review Letters* **60**(25), 2626.

Meerkov, S. (1977). Vibrational control theory. *Journal of the Franklin Institute* **303**(2), 117–128.

Miloshevich, G., Khomeriki, R., and Ruffo, S. (2009). Stochastic resonance in the fermi-pasta-ulam chain. *Physical review letters* **102**(2), 020602.

Mitaim, S. and Kosko, B. (2004). Adaptive stochastic resonance in noisy neurons based on mutual information. *Neural Networks, IEEE Transactions on* **15**(6), 1526–1540.

Mori, T. and Kai, S. (2002). Noise-induced entrainment and stochastic resonance in human brain waves. *Physical Review Letters* **88**(21), 218101.

Morse, R.P., Allingham, D., and Stocks, N.G. (2003). An information-theoretic approach to cochlear implant coding. In *AIP Conference Proceedings*, 125–132. IOP Institute of Physics Publishing, LTD.

Nayfeh, A. and Balachandran, B. (1989). Modal interactions in dynamical and structural systems. *Applied Mechanics Reviews* **42**, 175–202.

Nayfeh, A. and Balachandran, B. (1995). *Applied nonlinear dynamics*. John Wiley & Sons.

Neiman, A., Shulgin, B., Anishchenko, V., Ebeling, W., Schimansky-Geier, L., and Freund, J. (1996). Dynamical entropies applied to stochastic resonance. *Physical Review Letters* **76**(23), 4299–4302.

Nicolis, G. and Nicolis, C. (2000). Nonequilibrium thermodynamics and dynamical complexity. In *Stochastic processes in physics, chemistry, and biology*, 212–231. Springer.

Ogata, K. (2001). *Modern control engineering*. Prentice Hall PTR.

Pérez-Madrid, A. and Rubi, J. (1995). Stochastic resonance in a system of ferromagnetic particles. *Physical Review E* **51**(5), 4159.

Perkins, E. and Balachandran, B. (2012). Noise-enhanced response of nonlinear oscillators. *Procedia IUTAM* **5**, 59–68.

Perkins, E. and Balachandran, B. (2013). Noise-influenced dynamics of a vertically excited pendulum. In *ASME 2013 International Design Engineering Technical Conferences and Computers and Information in Engineering Conference*, V07BT10A025–V07BT10A025. American Society of Mechanical Engineers.

Perkins, E. and Balachandran, B. (2015). Effects of phase lag on the information rate of a bistable duffing oscillator. *Physics Letters A* **379**(4), 308–313.

Perkins, E., Chabalko, C., and Balachandran, B. (2013). Noise-influenced transient energy localization in an oscillator array. *Nonlinear Theory and Its Applications, IEICE* **4**(3), 232–243.

Perkins, E., Kimura, M., Hikihara, T., and Balachandran, B. (2015). Effects of noise on intrinsic localized modes. *Submitted* .

Poznyak, A.S. and Taksar, M. (1996). Robust control of linear stochastic systems with fully observable state. *Applicationes Mathematicae* **24**(1), 35–46.

Priplata, A.A., Niemi, J.B., Harry, J.D., Lipsitz, L.A., and Collins, J.J. (2003). Vibrating insoles and balance control in elderly people. *The Lancet* **362**(9390), 1123–1124.

Ramakrishnan, S. and Balachandran, B. (2010). Energy localization and white noise-induced enhancement of response in a micro-scale oscillator array. *Nonlinear Dynamics* **62**(1-2), 1–16.

Ramakrishnan, S. and Balachandran, B. (2011). Influence of noise on discrete breathers in nonlinearly coupled micro-oscillator arrays. In *IUTAM Symposium on Dynamics Modeling and Interaction Control in Virtual and Real Environments*, 247–254. Springer.

Rhoads, J.F., Shaw, S.W., and Turner, K.L. (2010). Nonlinear dynamics and its applications in micro- and nanoresonators. *ASME Journal of Dynamic Systems, Measurement, and Control* **132**, 034001–1–034001–14.

Rosenstein, M.T., Collins, J.J., and De Luca, C.J. (1993). A practical method for calculating largest lyapunov exponents from small data sets. *Physica D: Nonlinear Phenomena* **65**(1), 117–134.

Sato, M., Hubbard, B., Sievers, A., Ilic, B., Czaplewski, D., and Craighead, H. (2003a). Observation of locked intrinsic localized vibrational modes in a micromechanical oscillator array. *Physical Review Letters* **90**(4), 044102.

Sato, M., Hubbard, B.E., English, L.Q., Sievers, A.J., Ilic, B., Czaplewski, D.A., and Craighead, H.G. (2003b). Study of intrinsic localized vibration modes in micromechanical oscillator arrays. *Chaos* **13**, 702–715.

Sato, M., Hubbard, B.E., and Sievers, A.J. (2006). Colloquium: Nonlinear energy localization and its manipulation in micromechanical oscillator arrays. *Reviews of Modern Physics* **78**(1), 137–157.

Shannon, C.E. and Weaver, W. (1948). A mathematical theory of communication.

Sievers, A. and Takeno, S. (1988). Intrinsic localized modes in anharmonic crystals. *Physical Review Letters* **61**(8), 970.

Sobczyk, K. (2001). *Stochastic differential equations: with applications to physics and engineering*, volume 40. Springer Science & Business Media.

Socha, L. (2007). *Linearization methods for stochastic dynamic systems*, volume 730. Springer.

Stephenson, A. (1908). *On a new type of dynamical stability*.

Stocks, N., Stein, N., and McClintock, P.V. (1993). Stochastic resonance in monostable systems. *Journal of Physics A: Mathematical and General* **26**(7), L385.

Teolis, A. (1998). *Computational signal processing with wavelets*. Springer Science & Business Media.

Thomsen, J. (2002). Some general effects of strong high-frequency excitation: stiffening, biasing and smoothening. *Journal of Sound and Vibration* **253**(4), 807–831.

Ustinov, A.V. (2003). Imaging of discrete breathers. *Chaos* **13**(2), 716–724.

Vyas, A., Peroulis, D., and Bajaj, A. (2009). A microresonator design based on nonlinear 1:2 internal resonance in flexural structural modes. *IEEE Journal of Microelectromechanical Systems* **18**, 744–762.

Wiebe, R. and Spottswood, S. (2014). Co-existing responses and stochastic resonance in post-buckled structures: A combined numerical and experimental study. *Journal of Sound and Vibration* **333**(19), 4682–4694.

Wiesenfeld, K. and Moss, F. (1995). Stochastic resonance and the benefits of noise: from ice ages to crayfish and squids. *Nature* **373**(6509), 33–36.

Wihstutz, V. (1999). Perturbation methods for lyapunov exponents. *Stochastic dynamics* 209–239.

Wihstutz, V. (2003). On stabilizing the double oscillator by mean zero noise. In *IUTAM Symposium on Nonlinear Stochastic Dynamics: proceedings of the IUTAM symposium held in Monticello, Illinois, USA, 26-30 August 2002*, volume 110, 179. Springer.

Xu, X., Wiercigroch, M., and Cartmell, M. (2005). Rotating orbits of a parametrically-excited pendulum. *Chaos, Solitons & Fractals* **23**(5), 1537–1548.

Yabuno, H., Miura, M., and Aoshima, N. (2004). Bifurcation in an inverted pendulum with tilted high-frequency excitation: analytical and experimental investigations on the symmetry-breaking of the bifurcation. *Journal of sound and vibration* **273**(3), 493–513.

Zhi-Long, H., Xiao-Ling, J., and Zi-Qi, Z. (2008). Stability analysis of an inverted pendulum subjected to combined high frequency harmonics and stochastic excitations. *Chinese Physics Letters* **25**, 3099.